Imperial College London, London

Department of Materials

Investigating photovoltaic performance parameters of organic solar cells under and during 3-point bending flexural testing.

Huda Ahmad Jassim Hassan Ahli

Submitted in part fulfilment of the requirements for the degree of

Doctor of Philosophy

March 2022

Declaration

The work in this thesis was conducted between October 2018 and September 2021 in the Department of Materials and Department of Chemistry at Imperial college London. Some experiments were also conducted in the Department of Engineering and Material Science at Queen Mary University of London as a visiting student. The works is my own and any contributions from others have been acknowledged.

Huda Ahli

March 2022

Abstract

The overall goal of this thesis was to be able to answer the simple question as to how the performance parameters of a flexible OPV changes as it experiences 3-point mechanical bending tests. An inverted OPV with the structure of (PET/ITO/ZnO/ITIC:PBDP-T/MoOx/Ag) was chosen for this study. Three different bending radiuses were tested, 2.7 cm, 5 cm and 10 cm, and the devices were tested under illumination after 10, 50 and 100 bending cycles. From there, it was noted that bending radiuses of 5 cm and 2.7 cm led to mechanical degradation that resulted in a dramatic drop in J_{sc}, PCE, along with a dramatic increase in R_s. A novel in-situ method of monitoring the electrical resistance of the device while bending was used, to investigate the effect of bending on the interfaces and the individual layers. Where users will be able to obtain information regarding the mechanical limitation of devices' interfaces and interlayers for a given bending radius and bending cycles. It was concluded that the resistance overload resulted from a weak interface between MoOx and the active layer, possibly leading to increase in R_s. This was further confirmed via a manual peeling test, indicating that the active layer was intact and the top layer of the peeler had silver and MoO which was reported as a layer underneath the silver, lighter in color. The second mechanical degradation was witnessed in the active layer, as after 100 bending cycles, striation started to appear at 5 cm bending radius, and were more obvious at 2.7 bending radius which could results to further reduction in J_{sc} due to possible charge recombination processes. An in house, novel system was utilised in this study to understand the behaviour of a flexible OPV under bending, while under illumination with the focus of bending radius of 5 cm. From there, it was noticed that delamination spot changes upon bending and flattening the device causing fluctuations to R_s values and reversible behaviour of the device. Finally, the flexible OPVs were encapsulated via lamination techniques, in an attempt to move the neutral axis towards the device layers and thus, protecting any weak interfaces from mechanical degradation. Although the performance parameters of the flexible OPV, more specifically, R_s and PCE were not degraded with the same severity as the case with un-encapsulated devices. It is believed that the degradation, which is governed by reduction in V_{oc}, FF and R_{sh}, is resulted from creating a shunting path within the device. Which is believed to be an effect of encapsulation and not mechanical degradation. The FE analysis of both encapsulated and un-encapsulated substrates was conducted clearly indicating movements of the neutral axis towards the mid-plane of encapsulated substrates.

Acknowledgement

Firstly, I would like to thank the United Arab Emirates Ministry of Education for providing the financial support for this PhD. My supervisor professor Martyn McLachlan for his continuous support thought this journey, I learnt so much from him even beyond academia. I would also like to thank Dr Han Zhang and Dr Joe Briscoe for allowing me to work at their lab as a visiting student at Queen Mary university of London. Their support, help and interest allowed for this project to become a possibility.

Special thanks to those who have contributed to the work in this thesis: Akmaral Seitkhan from Prof Thomas Anthopoulos group in (KAUST), Dr. Ryley Ratnasingham, Dr. Matyas Daboczi and George Morgan.

Through my PhD journey in London, I found incredible people who became as close as family to me. Sana my best friend, sister and, the mother to my wonderful goddaughters, Rowda for being a great friend and mentor outside academia and Maitha for showing me what a kind heart really looks like. To my sisters and backbone, Muna, Hanna and Nada for tolerating my anxiety throughout the PhD and encouraging me. To my group members and Cohort 8, for welcoming me from the very start and specially Becky, Lucky, Faisal and Ahmad for all the times we talked and vented to each other.

To my mother for supporting me throughout my academic journey and believing in me, thank you for all your prayers, kind words and sacrifices, I love you.

Lastly but most importantly, to my husband for being my rock, my partner, and the love of my life, thank you for putting up with me.

I have learnt so much throughout this experience, and I could not have done it without all of you. From laughter to tears, to running my very first 10K, to experiencing life in London. I am very grateful for this journey.

TABLE OF CONTENT

List of Figures

List of Tables

Chapter 1

Introduction

The photovoltaic (PV) research sector has committed significant effort towards developing green, sustainable, low cost sources of energy that can be integrated into diverse array of environments, enabling applications such as: remote power generation for off-grid and standalone systems; building integrated PV (BIPV), wearable electronics as well as architecturally challenging locations where the placement of conventional, rigid PV would be impossible [1]. The drive to achieve clean, green energy generation is driven by national and international targets aimed at reducing CO_2 emissions, in 2021, More than 130 countries have made the same pledge of net zero target by 2050 including the UK and UAE. Thus, reducing dependency on fossil fuel and ensuing resilience in front of future fluctuation of energy prices [2].

Around 342 W m^{-2} of solar energy is received by the earth's atmosphere annually, 30% of this irradiation is reflected back into space and the remaining 70% equivalent of 239 W m^{-2} reaches the surface of our planet [3]. Depending on the location, the average solar power received is within the rage of 60-270 W m^{-2} annually [3, 4]. For example, the annual solar power in in London is around 109 W m^{-2} whereas in the United Arab Emirates (UAE) it is around 261 W m^{-2} [5, 6].

It is worth mentioning that from February until mid-May of 2020, around 200 countries around the world implemented a mixture of full and partial lockdown measure to contain the pandemic of COVID-19. These containment regulations and mobility constraint also disrupted and delayed both the supply chain and constructions of renewable energy projections especially PV and onshore wind installations in key markets such as China and the United States. Nonetheless, in mid-June of 2020 renewable-based projects have returned to near normal levels in terms of constructions, supply chain and implementing policies. This is because, manufacturers have adapted new systems of operation that align with the new social-distancing rules [7].

However, according to the data published by the International Energy Agency (IEA), most countries accelerated their renewable energy projects once the restrictions were eased, thus, they state that annual addition of solar power could reach over 142 GW and 150 GW in 2021 and 2022, respectively. Global annual PV contribution is expected to surge during period of 2023 until 2025 as the global market economy enhances [7].

This near exponential growth in PV industry has been mainly dominated by crystalline silicon solar cells [8]. Between the period of 2010 to 2020, the silicon PV industry underwent dramatic changes starting with, the reduction of manufacturing cost that is estimated around -15% per year in average and the continuous increase in efficiency of around +2% per year on average. Which lead to standardising the technology in terms of the design all the way to the supply chain [9]. Most of which is produced for ground mounting utility scale applications such as commercial and residential rooftop markets. However, one of the key challenges to further improve the silicon PV's efficiency is producing interfaces withing the cell structure to allow for very low recombination process thus, improving surface passivation of the cell [10]. Which requires a careful defect analysis and control as well a drive in the research field for new interface materials.

On the other hand, multi junction solar cells has set the record for the highest PV efficiency reaching 29.1% for single-junction GaAs (at one sun illumination) and 47.1% for six-junction device (under concentrated light) [11]. These record efficiencies along with the device's stability, made multi-junction cells very desirable for space application. However, these tremendous values come at cost of around 100-200 $/Wp. This high cost is what is keeping the multi-junction devices from dominating the PV market for terrestrial applications. Nonetheless, the technological path that leads to lower cost, will require multi-junction cells to enter larger markets to push the demand to increase production scale and reduce manufacturing cost [12]. Examples for near term market could include military, High-Altitude Long Endurance (HALE) vehicles and thermophotovoltaic. in the meantime, it is unclear which of these applications will offer significant growth in the multi-junction market to reach economies of scale.

The future of these PV designs and structure will mainly depend on improving energy yield and cost value trade of efficiency. However, when considering applications such as ground

transportation market and Building Integrated PV (BIPV), then a multifunctional thin film-based PV's that combine attributes such as opaque or semi-transparent and have a high power to weight ration must be considered. Unlike with the production of Silicon based PV, the approach of 'one size fits all' which is values on a cost per watt system can't be implemented in architectural applications. This presents BIPV's with difficult technical challenges due to the costs associated with designing, manufacturing, and certifying a range of sizes [13].

Nonetheless, it can be noted that the markets need governs the technological advancement and production cost of PV technology. Thus, as the sales of Internet of Things (IoT) devices grow, the demand of smart electronics increases. Here comes the need of developing new innovative power sources that are cost effective, maintenance free to be used in health, retail, and personal applications which is not a niche market anymore. Thus, significant work has been dedicating towards advancing flexible plastic based PV for smart wearable electronics and portable applications, which led to its efficiency to jump from 3% to 13% in 20 years [14]. Flexible PVs are great candidates among energy harvesting technologies in terms of their practicality as they are flexible, easily processable, have high energy to weight ratio and allow integration into various surfaces. In addition, they can overcome the obstacles of transportation, storage, mass production and viability of infrastructures as they are adaptable to roll-to-roll production as well as low temperature processes [15-17]. When compared to their rigid counterparts, stability and efficiency come as challenges for flexible solar cells. Nonetheless, their unique market target makes great candidate for their respective applications. The flexibility of these devices has allowed them to be portable power supplies, this is critical to the evolution of transportation and instrumental devices and technology away from the main grid. In addition, flexible PVs can be combined with shelters, clothing, and bags due to their lightweight at a lower production price compared to other technologies. In general flexible PVs can be categorised into three main groups, including perovskite solar cells (PSCs) [18], dye-sensitized solar cells (DSSCs) [19] and organic solar cells (OSCs) [20]. However, it has been reported that stripe-patterned silicon based solar cells that are electrically interconnected to have certain flexibility, but their complex fabrication process has made them economically undesirable [21]. The second generation of thin film solar cells such as gallium arsenide (GaAs) and copper indium gallium selenide (CIGS) have been

reported to have better flexibility compared to silicon based solar cells but the toxicity of some of the elements limited their wide use in large scale applications. This thesis will focus on third category which is the third generation of solar cells; OSCs, which will be extensively analysed [22, 23]. The flexible fabrication of OSCs will further maximize their manufacturing advantages over other forms of photovoltaic as low temperature processing methods are feasible in addition to OPVs being free of toxic material which make them great candidates for laboratory cyclic fatigue testing without encapsulations. Nonetheless, currently, establishing a set of performance characterisation for flexible cells in general is far from standardised. Many researchers have reported data related to performance parameters such as fill factor, efficiency and current density but without relating it to the mechanical durability in terms of minimum bending radius and cyclic loading tests.

However, the term "flexible PV" must be well defined in order to develop a scientific method to measure and examine the degree of flexibility. In many cases including the work reported in this thesis, polymer based flexible substrates are wildly used in fabricating PV flexible devices. These substrates can be bent, stretched, and twisted. The substrates' bendability is primarily measured to obtain the degree of flexibility by refereeing to radius of curvature (r_c). Around 80% of the device features must be maintained after bending with a range of r_c from 10 cm to 1 mm. in such case, the device is said to be "flexible" however if r_c was 1 mm or less, the device is said to be "ultra-flexible" [24].

Consequently, the research in this thesis focuses on fabricating flexible OPVs and measuring their performance evolution under different conditions of mechanical stress and strain.

Chapter 2 will cover the background knowledge needed to conduct the work in this thesis while also providing a review on the recent literature in mechanical testing of flexible OPV. **Chapter 3** will cover the methods employed to fabricate OPVs, analyze their constituent layers and to characterise the mechanical and optoelectronic properties of flexible devices will be discussed. **Chapter 4** will cover flexible OPV's optimization techniques followed by the initial results of the effect of 3-point bending in terms of, bending radius and bending cycles on the flexible OPV's performance parameters. **Chapter 5** will cover an in-depth analysis of the effect of 3-point bending on each individual layer along with their interfaces with adjacent layers. By introducing a new technique that allow to track the change in

flexible OPV's behaviour while bending via trancing the changes in the device's resistance. In addition, the effect of encapsulation on positioning the device towards the neutral axis was studied and confirmed via Finite Element Analysis (FEA). Finally, **in chapter 6**, will conclude with a summary of experimental findings discussed in this work and future outlook.

Chapter 2

Background

2.1 Organic Semiconductors

Once polymers are synthesised, they can be easily stored for long periods of time, as in most cases they do not require any special environmental conditions. Commonly they can be dissolved in a number of organic solvents and can be proceed into films by number of techniques available within research laboratory capacity including dip coating, spin coating and doctor blading and are also feasible for roll-to-roll printing for large area production [25].

A variety of flexible polymeric substrates can be sourced commercially at relatively low-cost. Typically, polyimide (PI), polyethylene (PE), polypropylene (PP) and Polyethylene terephthalate (PET) based materials are used depending on the processing and end use requirements [26]. Conductivity is achieved by depositing conductive material as a thin film onto one surface of the substrate, this is typically a transparent conducting oxide *i.e.* indium/fluorine doped tin oxide (ITO/FTO), aluminium and/or gallium doped zinc oxide (AZO/GZO) or complex mixtures such as indium gallium zinc oxide (IGZO) however alternative materials have been proposed that include silver nanowires [27, 28].

The inherent lack of conductivity arises from the saturated nature of the carbon backbones of these polymers, whereby the structure prevents the movement or generation of charge. Conducting and semiconducting behaviour can however be achieved in polymers that are both unsaturated and conjugated, through the process of hybridisation. Considering carbon, with an atomic number (Z) of 6, the electron configuration is $1s^2 2s^2 2p^2$ that would imply only the 2 outermost p-orbitals are available for bonding. Contrast this with the knowledge that carbon readily forms 4 bonds. This is explained by a process known as hybridisation, whereby

atomic orbitals may overlap/mix to form hybrid orbitals – it is this process that accounts for the profound differences in the electrical properties of PI/PE/PP and the semiconducting materials that lie at the heart of OSCs [25, 29].

Consider ethane (C_2H_6), sp3 hybridization occurs whereby one 2s-orbital and three 2p-orbitals (p_x, p_y, p_z) mix to create four hybrid orbitals with similar characteristics (Figure 2-1a). In this case hybridisation is possible owing to the small energy difference between the 2s and the 2p-states. Each sp3 orbital contains an unpaired electron that can form a sigma (σ) or single bonds. In the case of ethene (C_2H_4) sp2 hybridisation refers to the mixing character of one 2s-orbital and two 2p-orbitals (p_x and p_y) to create three hybrid orbitals with similar characteristics. The hybridised orbitals together form a trigonal structure, creating a molecular geometry of 120 ° (Figure 2-1.b). Each hybrid orbital can form in-plane σ bonds. The remaining unhybridized p_z orbital, lies perpendicular to the plane, and can overlap to form a delocalized orbital above and below the plane of the molecule – termed a π bond, Figure 2-1.b). Finally, in the case of ethyne (C_2H_2) sp hybridisation occurs, referring to the mixing character of one 2s-orbital and one 2p-orbital (p_x) to create a hybrid orbital. The hybridised orbitals form a linear structure, creating a molecular geometry of 180 ° (Figure 2-1.c). Each sp hybrid can form in-plane σ bonds. Two carbons can share one sp electron to form a σ-bond. The remaining unhybridized p_y and p_z orbitals lie in a perpendicular plane to the sp orbital and are both perpendicular to each other. The unhybridized p_z orbitals on each carbon overlap to form delocalized orbitals above and below the plane of the molecule – forming two π bonds [30-32]

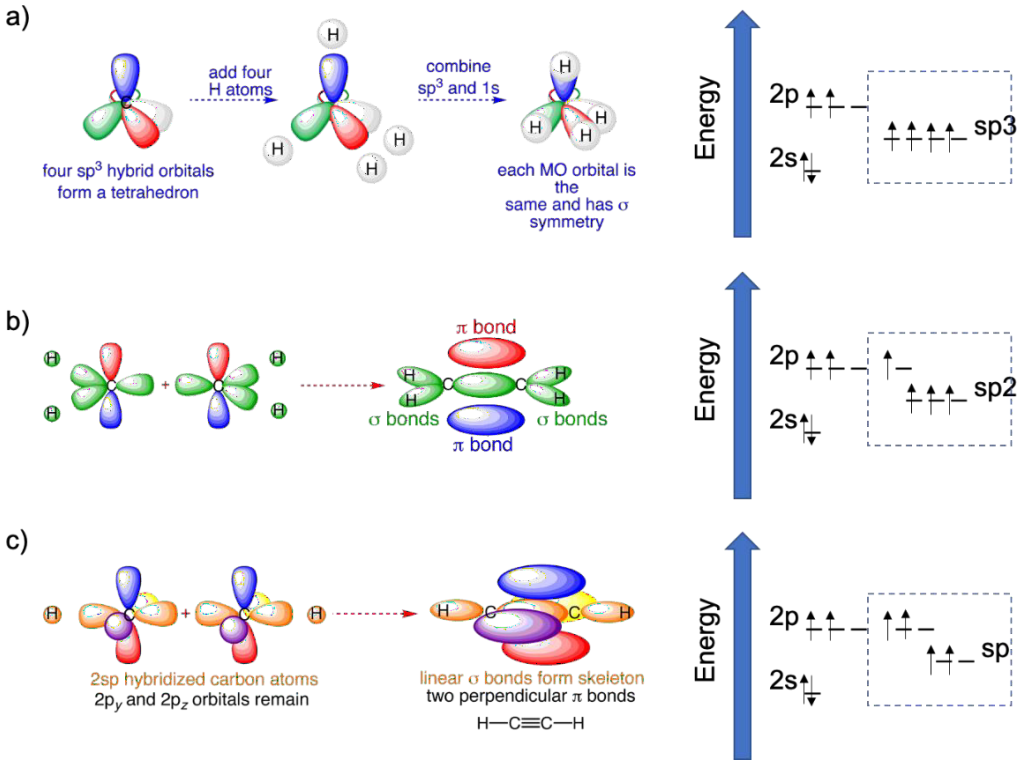

Figure 2- 1 a) Energy level diagram and bonding orbital of sp3 hybridization in ethane. b) Energy level diagram and bonding orbital of sp2 hybridisation in ethene. c) Energy level diagram and bonding orbital of sp hybridisation in ethyne. Taken from [32].

A molecular orbital may be approximated by a linear combination of atomic orbitals (LCAO). In the simplest case we can consider the combination of two 1s orbitals of two H atoms as the atoms approach. Rather than the 1s orbitals overlapping, they combine to form 2 completely new orbitals. It is important to note that when orbitals combine, the number of orbitals before the combination takes place must equal the number of new orbitals that result, so in this case the combination of 2 1s orbitals results in the formation of H_2, the result is two MOs, sigma (σ) orbitals. According to molecular orbital (MO) theory, the first sigma orbital is lower in energy than either of the two isolated atomic 1s orbitals – this is referred to as a bonding molecular orbital. The second, sigma-star (σ*) orbital is higher in energy than the 1s orbitals, and is referred to as an anti-bonding molecular orbital, as illustrated in Figure 2-2 [31, 33].

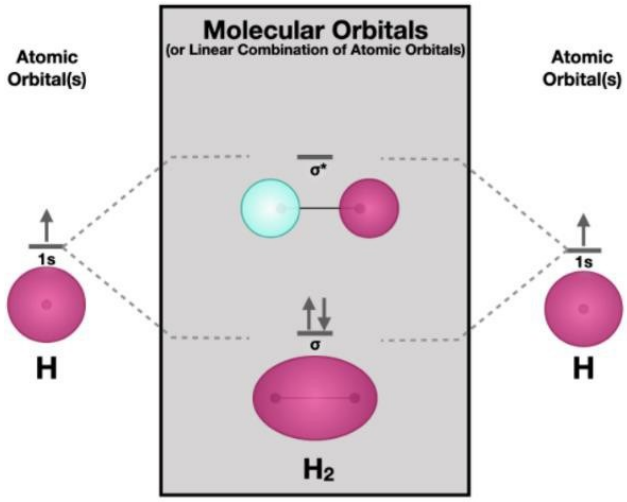

Figure 2- 2 Schematic representation of Linear combination of atomic orbital and the resulting of bonding and anti-bonding molecular orbitals in hydrogen. Adapted from:[34].

According to MO theory, the two atomic 2pz orbitals combine to form two π-MOs, one a low-energy π bonding orbital and one a high-energy π* anti-bonding molecular orbital. In the bonding orbital, the two shaded lobes of the 2pz orbitals interact constructively with each other, as do the two unshaded lobes, therefore there is increased electron density between the nuclei in the molecular orbital which is the origin of this being a bonding orbital. In the higher-energy anti-bonding orbital, the shaded lobe of one 2pz orbital interacts destructively with the unshaded lobe of the second 2pz orbital, leading to a node between the two nuclei and overall repulsion, hence anti-bonding orbital (Figure 2-3) [33].

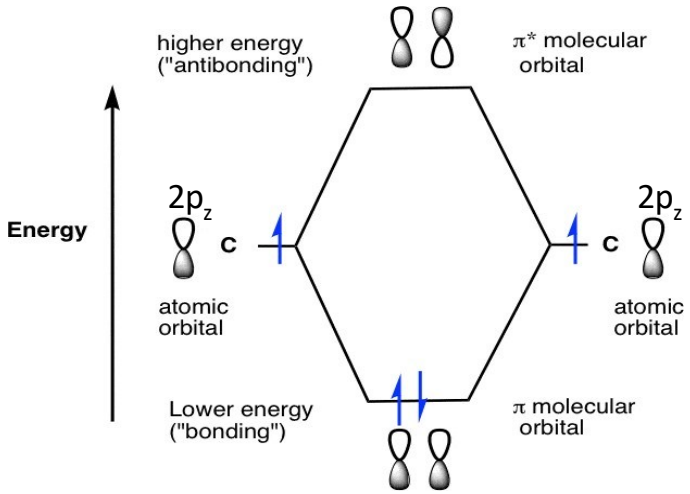

Figure 2- 3 Energy diagram of two 2pz atomic orbital combining resulting in two π molecular bonding one with higher energy π antibonding and a lower energy π bonding. Adapted from [35]. ©Copyright 2020, Master Organic Chemistry*

If we then consider a more complex molecule such as benzene, a cyclic, aromatic compound containing 6 carbon atoms where each carbon is bonded to a neighbouring carbon by a σ-bond (sp2 hybridisation). Each carbon however also has an unhybridized 2pz orbital containing an electron. The overlap of the 2pz electrons results in the formation of a delocalised electronic system both above and below the plane of the molecule (Figure 2-4)

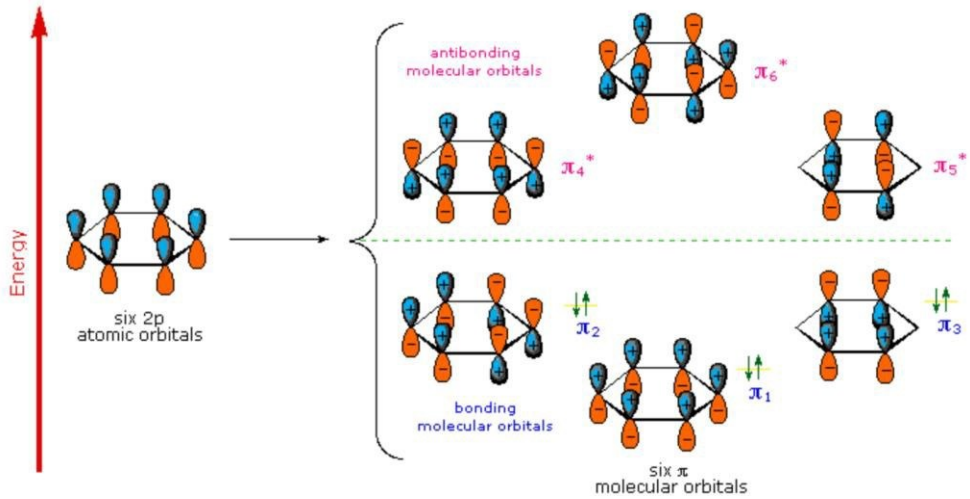

Figure 2- 4 The π molecular orbital of benzene. The dashed line represents the energy of an isolated p orbital, all orbitals below this line are bonding whilst all orbital above the dashed line are antibonding. Benzene has six electrons in its π orbitals thus, all the bonding molecular orbitals are fully occupied. Taken from [36] ©1999 William Reusch.

When we move to larger systems, such as polymers, we can extend this understanding to explain the origin of conducting and semiconducting properties. If we take ethyne (acetylene) as discussed above and form from it a polymer, polyacetylene Figure 2-5a, we have a polymer containing alternate sigma and pi bonds. In fact, it was the demonstration of conductivity in this polymer by Heeger, MacDiarmid and Shirakawa that gave rise to the field of organic electronics and earned the inventors the 2000 Nobel prize for Chemistry [37].

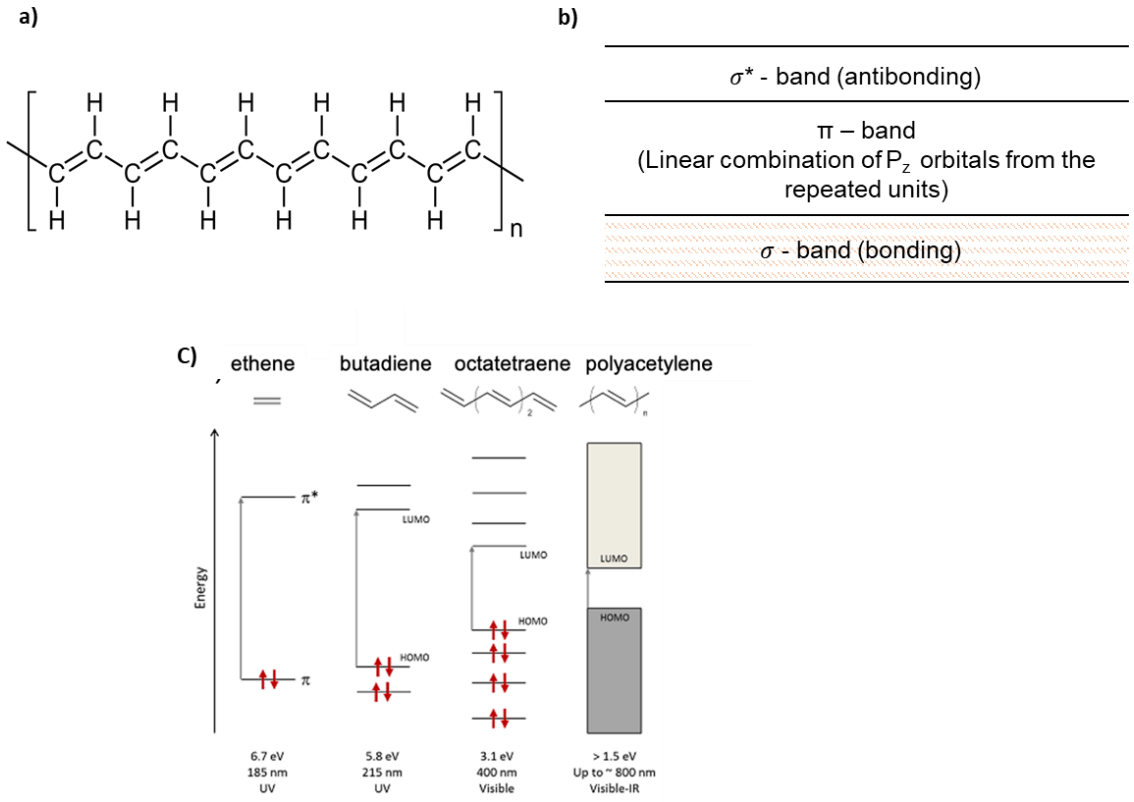

Figure 2- 5 a) polymerisation of acetylene to form trans-polyacetylene and b) schematic energy band diagram for a generic conjugated polymer c) the formation of σ and π bonds in conjugated organic molecules. Adapted from [38] © 2021 University of Cambridge.

It is the sigma bonds that hold the molecule together and the pi-bonds that create the interesting electrical and optical properties. The π-band, Figure 2-5b, originates from the p_z orbitals from each carbon atom in the polymer chain with the size of the band determined by the number of carbon atoms in the chain, Figure 2-5c. We have now, in essence created a bandgap that we can consider to be analogous to that seen in inorganic systems and where charge transport can occur owing to the extended delocalisation and charges can be

generated optically or electrically depending on the magnitude of the bandgap. We now consider transitions between the highest occupied molecular orbital (HOMO) and the lowest unoccupied molecular orbital (LUMO) rather than the valence and conduction bands of inorganic systems [39, 40]

2.2 Organic Photovoltaics (OPVs)

The main difference between OPV and inorganic photovoltaic (IPV) is the photocarrier generation process. In an IPV the free charge carriers are generated directly through the bulk of the semiconductor which in most cases consist of a single material. Whereas a mobile exciton (which consist of Coulombically bound electron and hole) is almost always the product of light absorption in OPVs [41, 42]. However, in an organic semiconductor, the electron and hole transport levels are the conduction band (CB) and the valence band (VB) respectively. Thus, making their equivalent in an organic semiconductor are the LUMO and HOMO levels respectively (Figure 2-6) [39].

To explain more, when a photoactive organic material absorbs a photon, electron excitation occurs from the HOMO level to the LUMO level. However, the electron and hole are still attracted to each other by Coulomb potential thus, forming an exciton with exciton binding energy within the range of 0.3 to 0.5 eV [43]. In such cases, the hole is present in an intragap energy level just above the HOMO level whereas the electron is occupying another intragap energy level below the LUMO energy level. This means, if the electrical energy gap is the difference between the HOMO and LUMO levels, then the optical bandgap has a smaller magnitude as it is equal to the different between HOMO and LUMO minus the exciton binding energy. The presence of the Coulomb potential around the charges causes the exciton to have a lifetime within the orders of nanometers. This lifetime length is referred to as diffusion length which has a value of around 10 nm [40].

Naturally, electrons are bounded in to a solid. Thus, at the out most surface of the material they are prohibited to escape to vacuum by an energy barrier that is capped the vacuum level

(E_{vac}). Evac can be defined as the electron's energy level to be located at rest within the outside of a solid material. Thus, having zero kinetic energy with respected to the material's surface [44]. Assuming there are no electrons present at the LUMO (in an organic material) or the conduction band (in an inorganic material) because of doping for example. Then the closest electrons to Evac level are those residing at valence band or HOMO level. Therefore, the minimum energy required to remove an electron from the system is known as the ionization potential (IP). On the other hand, the energy attained by adding an electron to a neutral molecule which will reside at the conduction band/LUMO is defined as electron affinity (EA) (Figure 2-6) [45].

The occupancy of the energy band is annotated by the position of the Fermi level (E_f). therefore, in a system under thermodynamic equilibrium, it is defined as the energy state with the 50% probability of electron occupation. consequently, above the Fermi level reside the unoccupied energy states in the Conduction band and below the fermi level reside the fully occupied energy state [39]. Therefore, in a metal, because the Fermi level marks the borders between the unoccupied and occupied states as a continuum of states, then it can be said that the that the work function (WF) is equal to both IP and EA (Figure 2-6). In a semiconductor however, work function depends on the location of both Evac and E_f , and these two parameters depend on temperature, density of state, carrier density and the doping concentration in a material [39, 46].

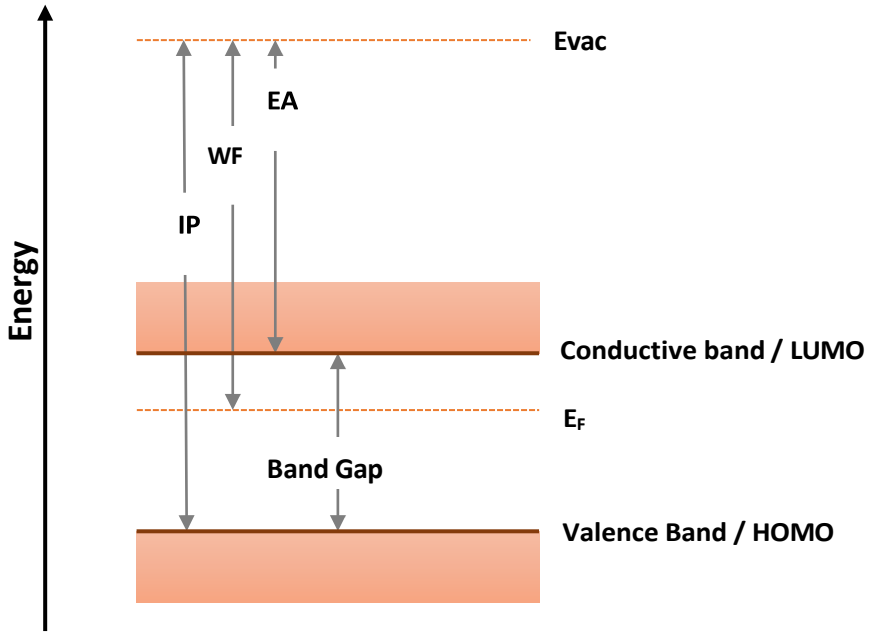

Figure 2- 6 Flat band energy level diagram illustrating energy levels in both organic and inorganic semiconductor. Where (IP) is the ionization potential which represents the minimum energy required to remove an electron from the system, (WF) is the work function and it is defined as the amount of energy which is required to pull out an electron from an atom, (EA) is electron affinity and definded as the energy attained by adding an electron to a neutral molecule which will reside at the conduction band/LUMO. Finally, (Ef) is the work function and it marks the borders between the unoccupied and occupied states

Operational mechanism

As explained above, light absorption by itself does not lead directly to photocurrent generation, owing to the high binding energy of the exciton. Which is why a recombination process between the hole and electron may occur, such recombination process in referred to as geminate recombination. However, if the exciton reaches an interface region between the photoactive material and another compound, the energy offset that the interface provides could overcome the binding energy resulting into exciton dissociation [47, 48]. In an OPV, the exciton dissociation is realised by blending a photoactive material which is also knows as a donor as it is the material that donates the electron, in this work, this material is (PBDB-T)[a] which is a polymer with an acceptor compound. In this work, the acceptor material is a small molecule known as ITIC[b]. Further information about the material used and their properties will be discussed later in Chapter 3.

[a] Poly[[4,8-bis[5-(2-ethylhexyl)-2-thienyl]benzo[1,2-*b*:4,5-*b'*]dithiophene-2,6-diyl]-2,5-thiophenediyl[5,7-bis(2-ethylhexyl)-4,8-dioxo-4*H*,8*H*-benzo[1,2-*c*:4,5-*c'*]dithiophene-1,3-diyl]] polymer

[b] 3,9-bis(2-methylene-(3-(1,1-dicyanomethylene)-indanone))-5,5,11,11-tetrakis(4-hexylphenyl)-dithieno[2,3-d:2',3'-d']-s-indaceno[1,2-b:5,6-b']dithiophene

The morphology of the blend is critical, owing to the relatively short lifetime of the exciton generated during photoexcitation. In general terms the diffusion length is considered to be of the order of a few to a few tens on nm, thus controlling the morphology of the blend *i.e.* the spatial distance between donor and acceptor is critical [49]. A bulk heterojunction (BHJ) morphology, Figure 2-7 has been widely used in OPVs. Such mixture allows for domain sizes of both materials to be within orders of nanometres and hence compatible with the exciton diffusion length [25]. In a BHJ blend, the electrons hop from the LUMO of the donor to the LUMO of the acceptor and the hols hope from the HOMO of the acceptor to the HOMO of the donor. At this stage, the electrons and holes are in different molecules, but because they travel at proximity of each other along the interface region, a bimolecular recombination could occur across the two molecules. Interestingly enough, such recombination could occur between an electron and a hole that are from different exciton origin. It is worth noting that BHJ require a high level of control during mixing to achieve the desirable morphology. In some cases, a non-continuous pathway to the other layers of the cell may result in trapping the electrons in isolated region of the acceptor material. On the other hand, high density of interfaces regions can increase the chances of bimolecular recombination [25].

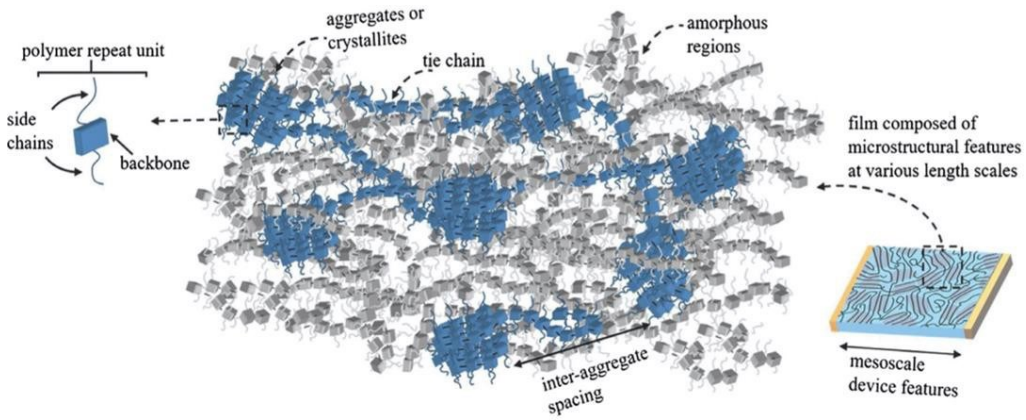

Figure 2- 7 Systematic representation of the microstructure of a conjugated polymer used as an active layer. As shown, the polymer layer comprises of ordered region which could be either crystalline or aggregated and amorphous region both of which are much smaller than the device dimension. The ordered domains are typically connected by the polymer tie chains. Adapted with permission from [50].

In addition to the blend morphology the energetics of the active layers and the surrounding charge selective interlayers and electrodes must be considered.

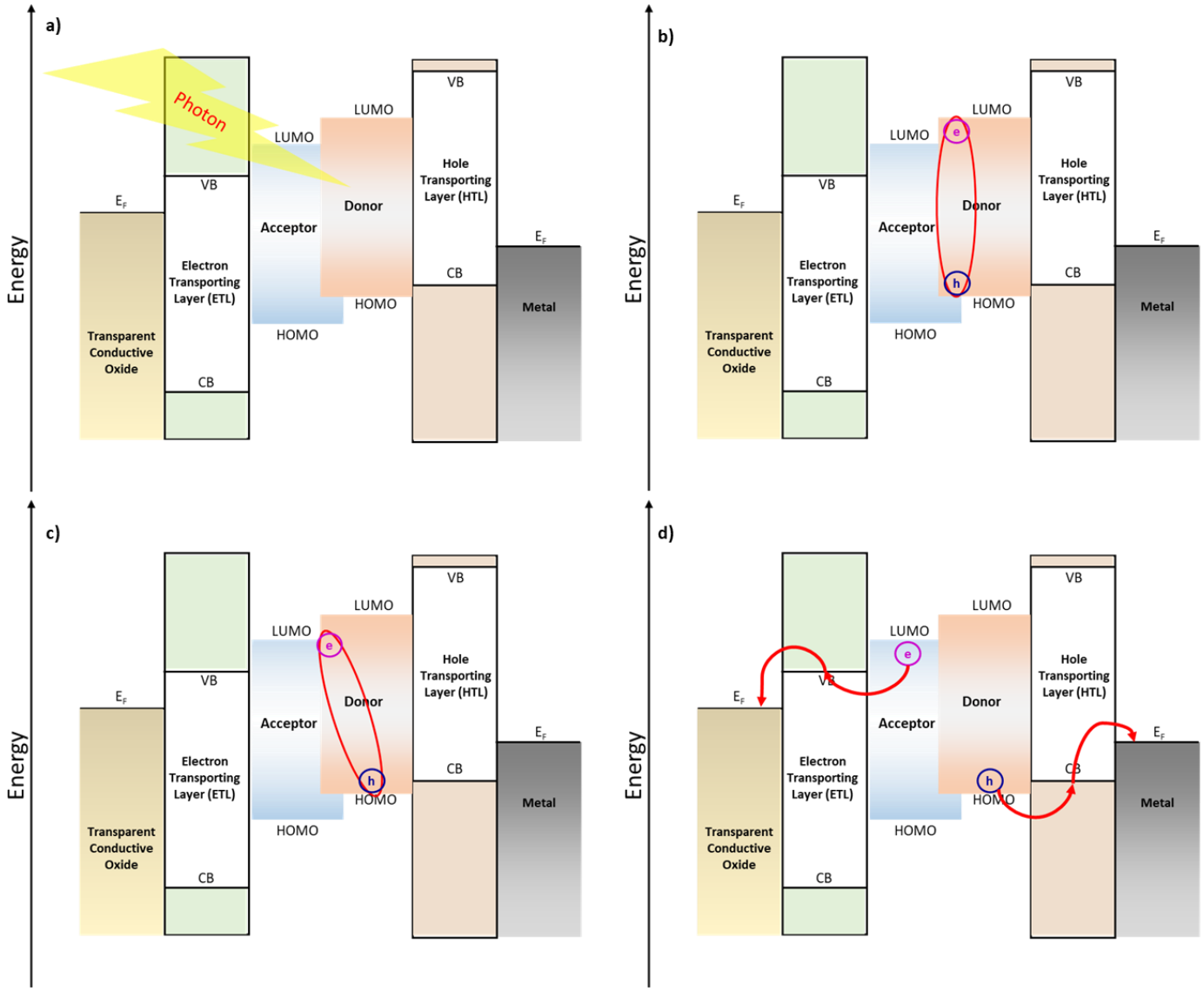

Figure 2- 8 Schematic representation of the energy levels and operation mechanism of a an OPV. a) the photon is absorbed by the active layer (Photon absorption). b) an electron is promoted to an exited state which creates a localised and bounded electron-hole pare (exciton generation). c) the exciton must dissociate in order to generate and photocurrent, this step occur at the interface between accepting and donating semiconductor (exciton dissociation). d) the dissociation results in transient charge transfer state at which the electron and hole are now in different molecules. Which is then followed by the electron and hole hoping into their perspective charge transporting layer (charge transport and extraction).

In the OPV structure illustrated in Figure 2-8a, the photon will be absorbed by donor. The resulting generated exciton will diffuse through the polymer until it recombines or reaches an interfacial region with the acceptor (Figure 2-8a-b). One of the main factors that limits the

efficiency of an OPV is the large energy loss (E_{loss}) which is attributed to both radiative recombination loss due to the considerable energy-level offset between the donor and a large non-radiative recombination loss generated by the extremely low electroluminescence efficiency of OPV materials [51] In general, it is known that the energy level offset between donor and acceptor should be larger than 0.3 eV. This is important to provide a driving force for excitor dissociated at the interface between donor and acceptor [52]. The electron then hops into the LUMO of the acceptor and the hole remains within the donor's molecules. They diffuse within their respective materials but alongside each other attracted by a much-reduced Coulomb potentials, and assuming bimolecular recombination does not occur, they eventually reach the charge extraction layers (CELs) (Figure 2-8c). Ideally an electron transport layer must have a shallow E_F providing by that, a desirable energy aliment with the LUMO level of acceptor molecules. On the right-hand side, the hole transporting layer must have a deep E_F and thus, creating an excellent energy alignment with donor's HOMO level [53].

Unlike OPVs, Si solar cell has p-n junction structure, thus, the driving force to separate the charge carriers towards the electrodes is provided by the built-in voltage at the p-n interface. Whereas as explained above, in an OPV, the exciton dissociation is promoted by the interfaces of the active layers. A built-in field does not exist to direct the charges towards the electrodes to be collected to the external wires. A small electric field only appears when both electrodes are put in electrical contact. This is because the electrodes E_F must equalise before a net flux of charges passes between them. this electric field is what helps navigate the charges towards their respective electrodes which shows the importance of device architecture in OPV operation mechanism.

Charge extraction layers function as a charge selector. This is important to note as the devise structure in this work is known as inverted structure (Figure 2-8). At which the ITO acts as a cathode and the metal that is more ambient stable and has high WF acts as an anode. In comparison, conventional structure has charge extraction layers of low WF metal such as aluminum (Al) as an anode. For fabrication, this requires a high temperature and high-cost vacuum evaporator that is not compatible to roll-to-roll process for large area printing. It has also been reported that using a more air-stable transition metal oxide (TMO) a charge extraction layer and high-WF metal as an electrode improves the stability of a device which is

an important parameter for wearable electronics [54]. As the anode and the cathode in an inverted OPV are reversed, this results in changing in polarity of the charge collection within the device. Due to this reverse polarity, the surface energy deference would induce a self-optimized vertical phase redistribution between the donor and acceptor. It has been found that thermal annealing is a critical fabrication process that can be controlled to further optimise the BHJ donor - acceptor vertical phase morphology. Adding additives or applying external electrical fields have also been reported as successful measures to improve vertical phase morphology [55]

2.3 Device performance parameters

Quantum efficiency

PVs can be represented as two terminal devices that conduct electricity in the dark in a similar manner as a diode and when illuminated, generate a voltage. Furthermore, when a PV is illuminated, it produces a photocurrent at short circuit conditions that depend on the intensity of the incident photon. The relationship between the induced photon and the photocurrent density (J_{sc}) can be described by the quantum efficiency (QE). QE is defined as the probability of delivering a single electron to the external terminal of the circuit. It is important to note that QE is independent of the induced photon spectrum. QE however, does depend on the charge separation and charge collection efficiencies in addition to the coefficient of absorption of the material used in the solar cell [31]. Given that the QE is a function of energy, Equation 2-1 can be used to characterise different solar cells behaviour into a QE versus wavelength curve.

$$E = \frac{hc}{\lambda} \qquad \text{Equation } 2-1$$

Where (h) is Plank's constant, (c) is the speed of light in vacuum and (λ) is the wavelength of the absorbed photon [31].

J-V characteristics

In the literature, there are numerous models that represent the J-V behaviour of a PV system [56]. Some of these models will incorporate more than one physical variable whilst other, take a simpler approach by designing a model based on a set of assumptions [57]. The equations presented in this section are derived based on an ideal single diode circuit. Where J_{sc}, positioned at the intercept point with the current axis, represents the short circuit current which is the maximum allowable amount of current that can be obtained when no bias is applied under illumination conditions. J_{sc} highly depends on the dissociation process of the exciton, the absorption efficiency of the active layer material and the successful transportation of charges cross the CELs to the electrodes that are in electrical contact. The fact that organic semiconductors have high absorption coefficient, allows the active layers materials within the device structure to be thin. However, because their energy level is localised, absorption can only occur over a small range of wavelengths from the overall flux of incident photon coming from sun, and as QE has a strong wavelength dependence, one can observe that QE reduces away from the visible spectral region, towards the blue and again towards the red region. The largest number of photons absorbed can be found at wavelengths of around the value of 6oo nm [58]. It is worth mentioning that non-absorbed light can be reflected back to the device by the electrodes, increasing by that the chances of absorption [59]. Moreover, choosing a transparent charge transfer layer with high refractive index can redistribute the light intensity and thus, maximising the light intensity [60].

The open circuit voltage (V_{oc}) is the intercept point at the voltage-axis, which represents the maximum voltage when zero current is passing through the terminals of the system. To explain more, increasing the voltage results in increasing the amount of charge recombination inside the system keeping them from passing through the terminals. Thus, at V_{oc} all the charges generated will recombine [61-63]. Ideally the area under the J-V curve, must be maximised to allow for high power generation. In a BHJ system, the V_{oc} dependence on the energy levels of the donor and acceptor can be illustrated in Equation 2-2.

$$V_{OC} = \frac{1}{e}\left(\left|E_{Homo}^{Donor}\right| - \left|E_{LUMO}^{ACCEPTOR}\right| - \Delta\right) \qquad \text{Equation 2-2}$$

The value of Δ ranges between 0.3 eV and 0.6 eV [64]. Thus, the value of the V_{oc} can be seen as the energy gap that results in electron and hole polarisation. Not to be confused the optical bandgap is the energy separating the bound electron and hole [65]. V_{oc} value is influenced by the operating temperature, film morphology and illumination intensity [25]. Its maximum values can be obtained by delivering the charge carries to the external wires without any drop in the voltage. Thus, an appropriate CELs must be selected to provide an Ohmic contact with the electrodes and therefore with the active layer.

Fill Factor

Another parameter that must be mentioned when studying the performance of a solar cell is the Fill Factor (FF). FF is the ratio between the maximum power obtained from a solar cell in the field and the maximum power generated from an ideal solar cell. A good value of FF will be around 0.8 whereas a poor value will be 0.4 [63].The solar cell parameters described in this section are evaluated in this work under standard test conditions (STC) which are at a 25 °C temperature of the cell, illumination of 1 kW m^{-2} and at solar spectrum of air mass (AM) 1.5 [66]. A study published by the Marks group shows that J-V plot can be divided into three regions that represent three different causes of mechanism losses, all of which affects the FF values and thus, the cells' power conversion efficiency (PCE) [67].

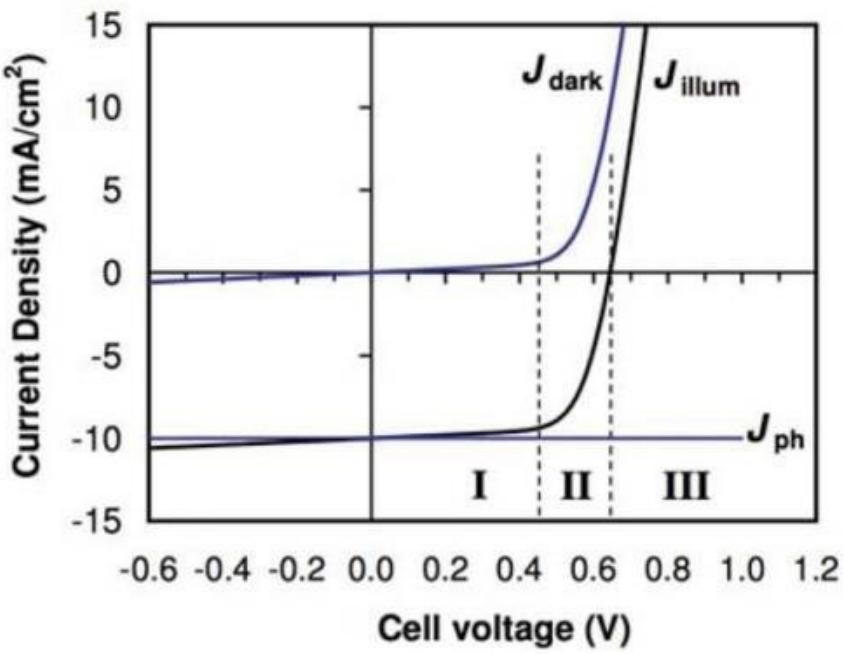

Figure 2- 9 J-V curve under dark and illumination for an OPV. the dashed line represents the three different region that indicate a specific losses mechanism. Region I) accounts for leakage current which in device parameters will translate as a reduction in the Rsh, Region II) accounts for recombination currents either due to potential difference between ETL and HTL or energy mismatch between HOMO/LUMO resulting in a drop in Voc and III) accounts for increase in series resistance. Adapted with permission from [67].

As illustrated in Figure 2-9 The first region (I) is located at the low positive biases, and it represents the current leakage, such defect can occur due to the presence of pinholes in the active layer or, cracks that initiated due to mechanical testing, which in device parameters will be a reduction in Rsh. The second region (II) is located at a moderated positive bias. The losses in here are due to recombination process which will effect Voc value and will be due to potential difference between HTL or ETL and/or energy mismatch between HOMO/LUMO level of donor and acceptor. The third region (III) is located at the high positive biases. The losses in there are governed by the internal resistance of the device and its component. Thus, giving a high value to the series resistance (Rs). Which means that in a J-V plot a high series resistance will result into a deviation from the vertical direction of the curve at voltages higher than the V_{oc}. Electrical properties of the interlayers and their interfaces must be controlled to ensure that R_S is at its minimum value. Under mechanical tests cracks may propagate causing isolated areas within one of the cells layers the cell, giving rise to R_S or may even lead to short circuit [68, 69]. However, this thesis will further investigate affects that mechanical testing would have on these parameters, and how one can prevent their degradation to insure the production of a practical flexible organic solar cell.

2.4 Transparent flexible electrodes for OPV fabrication

All layers within a device stack are critical for efficient device performance and it is important to consider the interaction and interfacial properties of all layers. Starting with the conducting electrodes, particularly the TCO through which light will typically enter a cell. The key parameters for the TCO are the optical transmittance and the sheet resistance, both having a significant impact on OPV performance [70]. The transparency is what allows the light to travel to the active layers improving by that the photon to current generation rate. Moreover, a mismatch between the thermal properties of the substrates and the films might cause the film to break during fabrication process, more specifically during annealing and cooling as well as the possibility of dimensional instability of the soft substrate. The substrate must also retain from releasing contaminates and unreactive against chemical processes which is very important during film deposition and evaporation of solvents during annealing [71]. Depending on the structure and type of flexible OPV, various electrodes have been employed and among these are, transparent conductive oxides (TCO), transparent nanomaterials (TNs) such as graphene and metallic nanowires such as silver nanowires [72]. In addition, one of the most well-knows and wildly used material for transparent electrodes in PV devices in general, is ITO.

Nonetheless, the integration of mechanical robustness and ideal transparency is an important specification for a substrate when used for the fabrication of an efficient flexible OPV, as these substrates must retain their optimum values of PCE and sheet resistance under different mechanical testes and deformations. Furthermore, their production must be scalable and continues to allow for fabrication techniques such as roll-to-roll [73]. Polymeric substrates such as polyethylene terephthalate (PET) and polyethylene naphthalate (PEN) that are modified with transparent conductive oxide such as ITO and FTO, have been attracting lots of attention as an alternative transparent flexible electrode [74]. This is due to the high flexibility the polymeric substrates over in addition to their low coast. As the integration of these material results in excellent electrical conductivity, lightweight as well as their feasibility to be mass produces for large scale [75]. However, it has been found that these hybrid substrates, brittle, rigid, chemically unstable and the plastic substrates could introduce

dimensional instability thus, hindering the performance of the cell [76]. It must be noted that these disadvantages are significantly linked to the temperature of the imprinting techniques of the ITO to the PET substrate [75, 77]. Another downside that must be mentioned regarding the use of the PET/ITO substrates is that their operating temperature must be below 150°C thus [78]. However, low temperature processed materials and simplified fabrication procedures that leads to long term stability are nowadays a high priority for many researchers that opens a numerous opportunities for novel structures of solar cells [79].

2.5 Mechanical properties for organic electronics

The main issue when considering mechanical properties for deformable organic devices, is the fact that the description does not specify whether qualities such as “flexibility” is attributed to the material dimensions or the material properties. As any material can be made flexible if it was sufficiently thin. “stretchable” is also another description that does not convey if the deformation is reversable (elastic) or permanent (plastic). In this work, a device that bends to a radius of curvature that ranges between 10 cm to 1 mm regardless of the thickness of the substrate is considered to be flexible. The device elongation range is not the focus of this work but in most literature, a device is said to be stretchable if the device can be elongated by around 5% of its original length [80].

In organic devices field, the most relevant mechanical properties can be viewed in Figure 2-10, which includes Elastic modulus (E) that is also referred to as Young’s modulus, elastic range (which is highlighted in grey), yield point and strain at fracture [81].

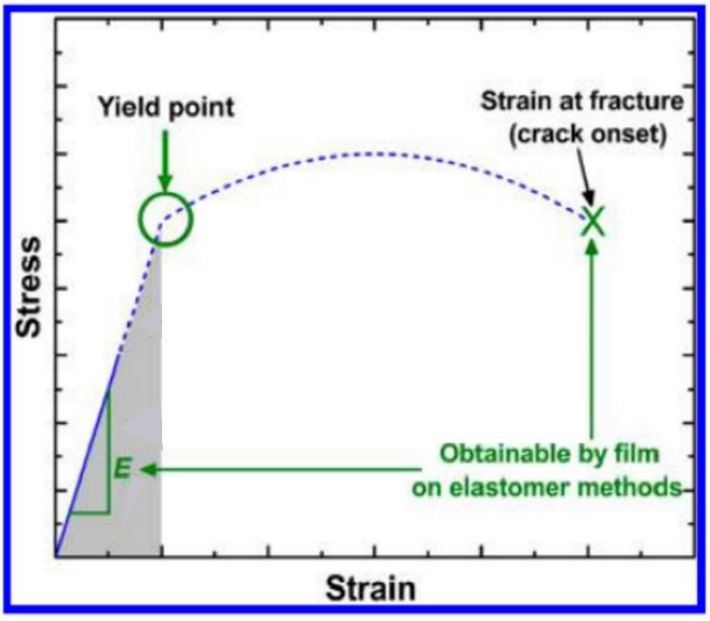

Figure 2- 10 Theoretical stress-strain curve for bulk polymer. Young’s modulus (E) is the slop of the elastic region (the material can retain back to its original shape- shaded in grey). the area between the yield point and crack-onset is plastic region (the material is permanently deformed). Reproduced with permission from reference [82]. Copyright © 2015 American Chemical Society.

Multiple factors determine these properties in an OPV including, the structure of the individual molecules in the material, how these molecules are packed in soled state, and the structure of the device and its interlayers [83]. there are challenges that one may encounter when measuring these mechanical properties, as it is difficult to handle thin films for some tests followed by then the reality that not enough material can be obtained or produced by laboratory scale synthetic procedures, that would allow the fabrication for a large number of films [84, 85]. This work is more focused on the evolution of the entire device performance during mechanical deformation and its effects on the device's interlayers.

Young's modulus

The ability of a material to store mechanical energy reversibly is known as Young's modulus (E). It refers to the amount of force required per a given area (stress (σ)) to uniaxially deform a material causing a change in its original length (strain (ε)) in a reversible manner [82].

$$\sigma = \frac{F}{A} \qquad Equation\ 2-3$$

$$\varepsilon \frac{l - l_0}{l_0} \qquad Equation\ 2-4$$

$$E = \frac{\sigma}{\varepsilon} \qquad Equation\ 2-5$$

Where F is the force applied, A is the unit area, l is the deformed length and l_0 is the original length at equilibrium position. Young's modulus unite is force pre unit surface (N m^{-2}) also known as pascal (Pa).

Table 2- 1 *Shows the values of Young's modulus of typical materials used in fabricating an organic solar cell.*

Layer	**Material**	**Young's Modulus (GPa)**	**Reference**
Substrate	PEN	6.1	[86]
Substrate	PET	2.7	[86]
Substrate/Encapsulation	PI	4	[86]
Substrate/Encapsulation	Glass	90	[87]
Transparent electrode	ITO	150	[88]
Transparent electrode	Graphene	1000	[89]
Transparent electrode/ HTL	PEDOT:PSS	0.8	[90]
HTL	MoO_x	86	[91]
ETL	ZnO	96.1	[92]
ETL	TiO_2	288	[86]
ETL	LiF[c]	65	[86]
Donor	PBDB-t	NA	-
Donor	P3HT[d]	0.25	[93]
Acceptor	ITIC	1.63	[94]
Acceptor	PCBM[e]	3.06	[95]
Electrode	Ag	74	[86]
Electrode	Al	70	[87]

It must be noted that the method followed to obtain such properties have a high effect on the values recorded. There are several approaches to attain Young's modulus such as nan-indentation, recording the mechanical resonance by imaging techniques such as Transmission electron microscopy (TEM) and tensile bending of thin films [96]. As the work in this thesis heavily rely on cyclic loading and failure of the devices thus, the results of tensile testing method were used to record the values at Table 1-1 from different references. Moreover, the mechanical properties of the thin films often differ from those of bulk samples of the same material [97]. Thus, when considering the effects of an overall working device, thin films would produce more insightful results that are more compatible the properties the material exhibit in a device structure.

The values of Young's modulus are only valid within the elastic regen of the material before any permanent plastic deformation occurs (the slope of the curvature in the leaner region). For flexible electronics, this value incredibly important as it can be controlled to reduce

[c] Lithium fluoride

[d] poly(3-hexylthiophene-2,5-diyl)

[e] Phenyl-C61-butyric acid methyl ester

interfacial stress between interlayers of the devise as well as between the device and the skin in case of wearable electronics [98]. The phase of the solid material directly influences the molecular mechanisms that is responsible for storing elastic energy. For example, in crystalline and semi-crystalline solids, the molecules movement from their equilibrium position in the lattice, results in the production of a restoring force. The restoring forces in van der Waals solids can be described by Lennard-Jones bonding potential. Lennard-Jones potential is a function of the distance between the centres of two partials. When the two particles that are not bonded to each other are at an infinite distance, their potential energy is said to be zero. Upon mechanical deformation, the distance between the two particles decreases until they bound. At this stage, their potential energy drops from zero to a negative quantity and the particles each an equilibrium. Any further mechanical deformation beyond this stage, will lead the particles to pass their equilibrium distance and a repulsion mechanism occurs. This repulsion is associated with forcing the electors to occupy each other's orbitals thus, repulsion will continue until the electors are at places at their own original orbitals [99].

Yield Point

The termination of the elastic region of a solid material can begin by the start of plastic behaviour or brittle fracture. At this point, the storing force (i.e., the energy stored by the molecules during the deformation at the elastic region) is converted into plastic deformation. At this stage, the molecules alter themselves to a new configuration. Thus, for van der Waals, the molecules will slide past reach other which is facilitated by the side chains. On the other hand, for semi-crystalline materials, the amorphous region can interlink in the crystallites, thus, a strong intermolecular force is present thus, the material displays brittle fracture at the yield point [82, 100]. For semiconducting materials, the extend of the plastic deformation on the microstructure affect the optical abruption and charge transport properties [101]. In applications that require the OPV to be attached into moving parts (human body or machine) it is more desirable to operate within the elastic region as the device will experience repeated deformation. Whereas, if the flexible OPV is integrated into building or a lens (*i.e.* attached to curved surfaces permanently) it is acceptable to for the solar cell to bent beyond the yield point (i.e., permanently deformed and can't retain its original flat shape) as long as the deformation isn't deteriorating the device performance [100, 102, 103].

Crack Onset

Once the total energy absorbed by the spacemen up to the point of crack (toughness) is exceeded by the mechanical energy applied, the bulk structure of the sample fractures. For organic materials, this depends on the molecular weight and the soled phase. For small molecular semi-conductors such as ITIC, fracture occurs when the mechanical energy density overcomes van der Waals forces. For crystalline solids, the fracture occurs between grain boundaries [104, 105].

The initiation of crack within an OPV is not necessarily catastrophic. The mechanical degradation of the device performance depends on the extend of the crack and the direction of the flow of the charge carries within the device [106]. In OPV, the direction of charge transportation is perpendicular to the device plane thus, crack propagation in direction of the charge transport can results into the illusion of having multiple devices that are connected in parallel. Nonetheless, a crack that extends from the electrodes through the active layer will short circuit the device and result in complete failure [107].

Adhesive fracture energy and interfacial strength

Poor adhesion between the adjacent inter layers of a device can lead to misalignment and delamination specially when the device undergoes mechanical deformation. Different processing techniques of each layer as well as the difference in the mechanical properties of the layers can also lead to poor adhesion. Four-point bending can be used to quantify fracture energy [108, 109]. Fracture or adhesion energy (G_c) (J m^{-2}) is defined as the energy needed to propagate a delamination at the interfacial region between the adjacent layers [110]. This occurs once the strain energy overcomes the adhesive fracture energy which is expressed in Equation 2-6.

$$G_c = \frac{21(1-v^2){P_c}^2L^2}{16Eb^2h^3} \qquad Equation\ 2-6$$

where P_c is the load, E and v are Young's modulus and Poisson's ratio of the substate. L is the distance between the outer and inner pins of the four-point bending, b and h are the width and half the thickness of the sample [110].

Using four-point bending technique to measure involves placing the OPV stack between two beams usually being glass or silicon wafers using epoxy resins and applying a load the four-point bending pins. As seen in the schematic representation in Figure 2-11. The upper layer of the sandwich is notched to ensure that the propagation of the crack into the weakest interface rather than propagating a crack throughout the thick substrates [110].

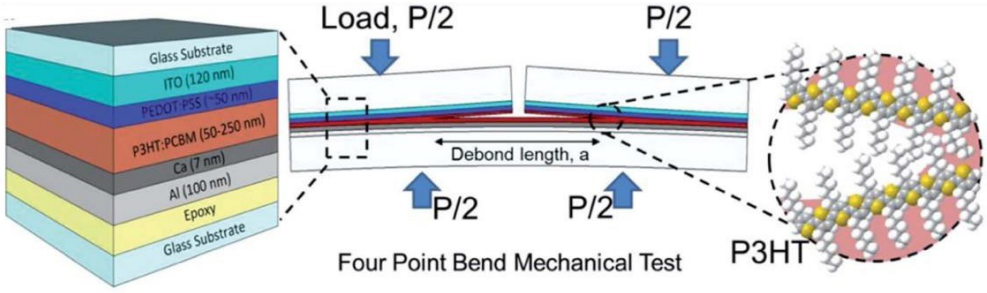

Figure 2- 11 Schematic representation of four point bending test designed to measure the adhesion energy of the P3HT–PCBM active layer in an organic solar cell. Adapted with permission from: [111]

For flexible OPV, multiple factors affect the value of G_c such as, the composition of each layer, the annealing temperature and any post treatment, type of hole transporting layer used and deposition rate and thickness of the metal electrode. It has been reported that metal oxides layer that are typically used as CELs such as (MoO_3 ,V_2O_5 and ZnO) lower adhesion energy [110]. As these materials relay on the inter-particulate interaction to remain in cohesion, thus having G_c values to be below 0.7 J m^{-2} [112]. The intermolecular forces of solution processed molecular materials such as C60 fullerene layers are weak due to the absence of strong iconic or covalent bonds which resulted in low values of G_c (0.1-0.5 J m^{-2}) [112]. Whereas semiconducting organic materials such as P3HT and PTAA, have higher values of G_c that ranges between 2.5 to 8 J m^{-2}. Higher values of adhesion energy from high molecular weight polymer, results from the presence of chain entanglement and interactions, thus, upon any fracture due mechanical deformation, these covalent bonds must be broken. In BHJ mixture in a flexible OPV, the presence of fullerene materials could negatively impact the value of G_c because of the reduction of chain interaction in these polymers [113].

Another method worth mentioning that allows for measurements on adhesion strength in different applications, is peeling test. In this test, a laminate is bonded either to another laminate or to a thick substrate, and the test begins by pulling the laminate off from the other laminate or the substrate at a constant rate as indicated in Figure 2-12 [114]. The peeling force is recorded during debonding and depending on the application the peeling angle is decided, T-peel test (ASTM D1876) is typically utilised for flexible bonded materials such as

flexible OPV applications. In such applications, the samples would have the following structure: (laminate layer/device layers/laminate layer), and during the peeling test, rupture occurs either at a weak interface or within a weak layer of the of the whole device [115]. Therefore, the measured peeling strength is only representative of the ruptured area which is identified via the use of Scanning electron microscopy (SEM) with energy dispersive X-ray spectrometry (EDX) [115]. During test, the machine records the applied force across the displacement, which in case of T-peel test would be upward movement of the rig. Thus, a force/displacement curve is generated, and the peeling strength is then calculated as average load divided by the width of the specimen [114].

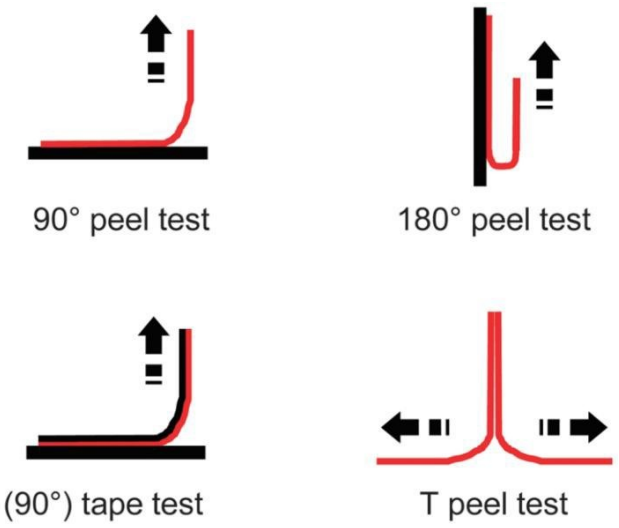

Figure 2- 12 Illustrates different peeling tests with different angles of peeling. Red represents the laminate layer while black represents a substrate. Taken from [116] © The Royal Society of Chemistry 2016.

2.6 Encapsulation of flexible OPV

Depending on the device structure and material selection, one of the degradation routes that an OPV suffers from is caused by moisture and oxygen when the cell is exposed to air. Moreover, when compared to glass substrates, PET and PEN lead to faster degradation routes due to their abilities to transport gases. To avoid these paths of degradation, and improve device lifetime and stability, encapsulation (i.*e.* barrier material) can be introduced to the device structure [117]. Moreover, due to the thickness the substrate and the encapsulation material have, they are mainly the responsible layers within the device with the mechanical strength to keep it intact [118]. Thus, material properties that describe the ability of the material to store mechanical energy, is less important for the organic semiconductors and other interlayers within the OPV and more important for the plastic substrate the encapsulating materials. For the organic semiconductors and other interlays within the device, having low Young's modules vales and height crack-onset is more important to consider to minimises interfacial stress. This can be done by adding an encapsulating layer on top and bottom of the sandwich device, moving by that the neutral axis to the midplane of the device protecting by that any weal interfaces from strain that would cause delamination [109, 110]. The encapsulation material for flexible OPV should bear properties such as, high optical transparency, low permeability of moisture and oxygen, photochemical and thermal stability, strong adhesion to the substrate, mechanical flexibility and cost effective [119].

2.7 Mechanical bending

Mechanical characterisation techniques for flexible electronics applications can be sub-divided into two categories: Testing to determine the mechanical properties of each material (constants) and testing to track the evolution of the device performance. The latter, in the focus of this work and the information of the device performance under stress or strain can be extracted using number of techniques. The best experimental designs entirely decuple the experimental procedures from human involvement by automating the test. Thus, ensuring that a uniform bending strain over the entire sample is being imposed and controlling the bending stress, strain rates and forces. Moreover, it is important to ensure minimum contact with the device and automatically measure the device's parameters [120, 121].

The most common test used to determine the mechanical properties of a material along with their fracture properties, is the bend test. In such testing, the material is subjected to a bending load. bending tests enables the control of the load distribution over the specimen. During any bending tests, pressure is applied to the specimen with loading pin that has either a circular or rectangular cross section [121, 122]. Once the loading pin, is in direct contact with the specimen that is perpendicular to its cross section, the specimen will gradually be bent. In this work, the OPV will be subjected to a cyclic loading of bending and relaxing movements up until the failure point of the device's performance [121, 122]. Depending on the loading method, there are two types of bending test: three-point bending, and four-point bending as illustrated in Figure 2-13

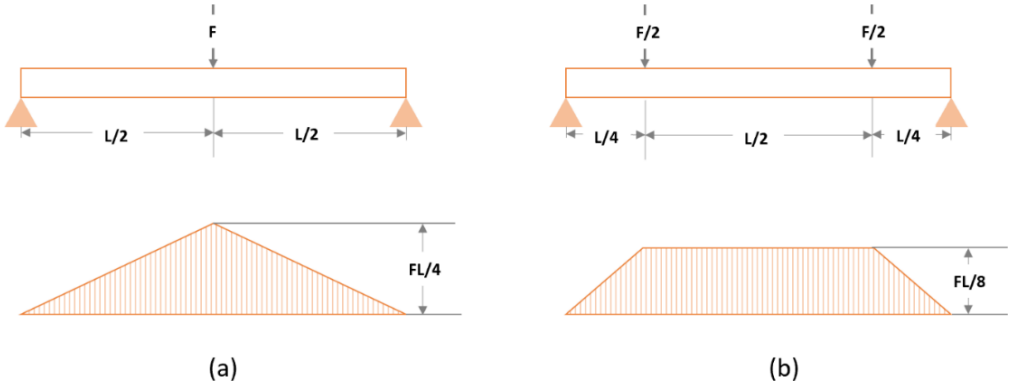

Figure 2- 13 A schematic representation of (a) three-point bending along with the distribution of bending moment (moment = force x distance from the pivot) along the length of the specimen where the maximum moment is allocated at midspan. (b) In four-point bending the maximum moment is allocated between the two loading pins.

In the case of three-point bending, the maximum bending and thus the maximum pressure are located at the midspan zone. In here the substrate rest on two support pins and the load pin is positioned at the centre of the specimen. Materials that do not fracture or fail under maximum strain during three-point bending, could be more suited to be tested via four-point bending. The main difference between the two methods, is the distribution of the maximum bending moment and maximum axial stress [123]. In four-point bending, the maximum axial stress is located between the loading noses. Such tests fall under the American Society for Testing Material (ASTM) standards D790 which is specifies the testing method for flexural bending properties of plastics [123]. It is important to note that for flexible devices failure modes during bending tests can be indicated by delamination or cracking [124, 125]. However, the literature lacks on how these deformation modes effect the performance of the OPV.

Bending mode tests have been studied in literature for OPV applications, however, the power profile of the incident light has been reported to complicate the study [126]. In most solar simulators, the spatial power distribution is calibrated to deliver 100 mW cm^{-2} uniformly at a specific plane. As the device bends, both spatial and spectral power disruption of the light could depart from the typical measurement plane. Moreover, light abortion and reflection are both affected by the incident light angle, all these effects could lead to some uncertainties when measuring the OPV performance parameters [127, 128]. Thus, researchers may accept

uncertainties or else there have been couples of methods that has been reported that could reduce these possibilities of errors such as: flattening the device before conducting evaluation measurements or preform cyclic testing at different radius of curvatures [126, 128]. In general, bending is an important deformation mode of testing that allows the development of flexible devices.

Neutral axis and critical values

The neutral axis in a bent sample, is a region within the cross section that does not experience any elongation or compression. Looking at the bent sample in Figure 2-14, it is clear that the top section of the sample's cross section, experiences compressive strain and thus, undergoes compression. Conversely, the lower section of the sample's cross section undergo tensile strain and thus experiences tensile stress. This is true in case of a downward force, the opposite must be considered if the loading pin had an upward direction. However, a plane in between these two sections, dose not increases or decreases in length and hence experiences zero strain. Ideally for flexible electronics, by introducing a substrate and the encapsulation layer with similar Young's modulus values and similar thickness would move device structure must be places in this neutral axis region. Consequently, avoiding any deformation due to bending and thus, abstain from device failure [129].

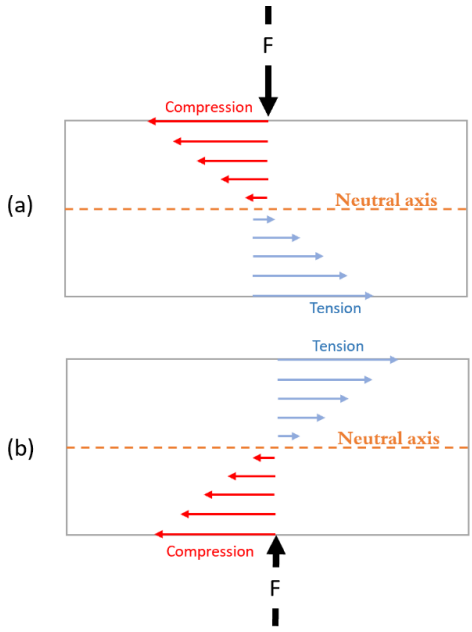

Figure 2- 14 schematic representation of the stress distribution along the cross section of the sample.(a) indicates a downward load direction (b) indicates an upwards load direction.

The critical strain (ε_c) is a point beyond which the external forces apply causes mechanical damages and hence, the device functionality deteriorates. This indicates that the critical strain, is corelated with the critical radius of curvature. The critical bending radius is defined as the value of radius at which the device components mechanically or electrically fail. Since maximum strain can take place at one of the surfaces of the device and as most flexible devices and more specifically flexible OPV have metallic contact or insulating material as a final top layer, the stain at the topmost surface becomes critical. In literature, a flexible device is one that it's component can sustain (ε) < 2% and withstand bending with a range of r_c from 10 cm to 1 mm [130].

The Maximum strain value that is located on the top surfaces of the substrate can be calculated using the following equation [131, 132]

$$\varepsilon_{peak} = \frac{t}{2r_c} \qquad Equation\ 2-7$$

Where (t) is the substrate thickness. This equation shows the relationship between the maximum strain value, substrate thickness and radius of curvature for homogeneous sheets.

It is clear from Equation 2-7, that thinner sheets would experience lower maximum strain values compared to thicker substrates. Nonetheless, the strain would change under the presence of compressive and tensile stress on either surfaces and thus on each layer. The variation in a homogenous film is liner but more complexed for layered structures, which will be further discussed in Chapter 5 in which both the substrate's and ITO layer's thicknesses and Young's modulus values will be taken into consideration [120].

Built-in residual stress

Build in residual stresses are produced during the fabrication process of the devices and thus they depend on the deposition conditions such as: thermal treatment and machining of each material. Such cases are very frequent at laboratory scale fabrication as the substrate as small and the fabrication processes are not automated and well designed. The causes of the residual stress can be categories into two sections:

- Mechanical treatment: When handling the substrates during fabrication, the substrates could undergo non-uniform deformation across the across section of the material. In this case, the region closes to the external force applied could deform plastically and further regions could deform elastically. Hence, upon the removal of the external force, the elastically deformed regions would try to restore their original conditions, but the plastically deformed regions would prohibit this recovery. Consequently, the elastically deformed region will only partially recover. Thus, remining at a stress state.
- Temperature variation: After annealing process, during the cooling stage, the outer section that is in contact with ambient ait, cools faster than the underlaying layers. Thus, causing contraction. As these regions contract differently stress withing the material starts building up.

Although this work will not focus mainly on the effects not the measurements of residual stress within the devices, it is however important to note that these residual stresses can cause shape distortion, allow for crack propagation [129, 133]. As the devises in this work are fabricated in the laboratory, it is important to track such changes.

Chapter 3

Experimental methods

In this chapter the methods employed to fabricate OPVs, analyse their constituent layers and to characterise the mechanical and optoelectronic properties of flexible devices will be discussed. A description of the various characterisation techniques employed in this thesis will be given, these techniques are divided into the following categories: mechanical testing, optical and electronic methods, structural and morphological characterisation.

3.1 Substrate preparation

Two principal substrate types were utilised in this study, glass (1.2 cm x 1.2 cm) and PET (1.2 cm x 8 cm) with thickness of 0.21 mm, both of which are pre-patterned with ITO (13.6 Ohm/□) with 8 mm strip design and acquired by PsiOTec Ltd. Figure 3-1 shows a schematic diagram of the PET substrate.

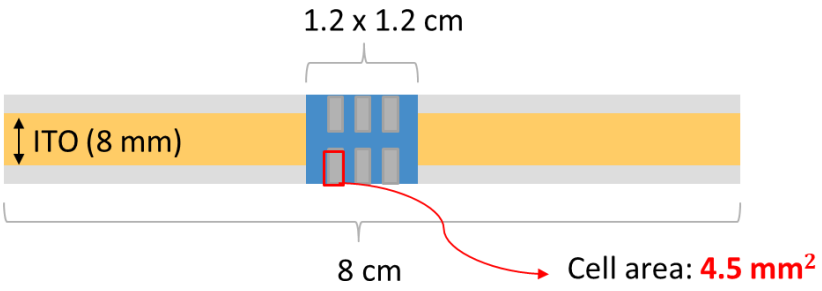

Figure 3- 1 A schematic representation of the PET substrate with ITO stipe design. The 1.2 cm x 1.2 cm is the area of where six pixels are fabricated with each pixel being a device. each device area is 4.5 mm^2

Prior to use, glass substrates were sonicated in an ultrasonic bath for 10 minutes intervals sequentially in acetone, isopropanol and finally deionised water. The same process was repeated for the PET substrates with the acetone removed and replaced with aqueous detergent to avoid degradation and damage of the PET surface. All substrates where then dried using a nitrogen gun and then placed in the UV-ozone cleaner for 20 minutes before further processing.

3.2 Photovoltaic device fabrication

This section will cover the fabrication method of the OPVs used in this work including the fabrication process of each individual layers and their deposition conditions. The device structure utilised in this work is the inverted structure (see Figure 3-2), discussed in more detail in Chapter 2.

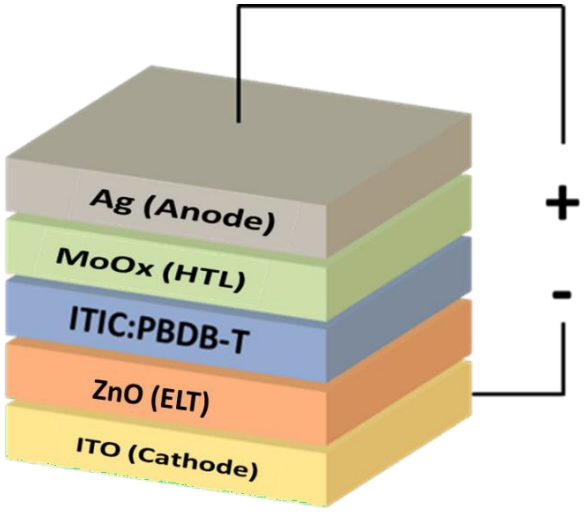

Figure 3- 2 Schematic drawing of the inverted device architecture utilised in this study. Here ITO serves as the cathode, ZnO serves as the electron transport layer, ITIC:PCE12 as the active layer/absorber layer, MoO_x as the hole transport layer and finally silver as the anode.

Electron transport layer deposition

Zinc acetylacetonate hydrate ($Zn(acac)_2.xH_2O$) (Sigma Aldrich) was dissolved in 2 ml of anhydrous 2-methoxyethanol (Sigma Aldrich) and 60.4 µl of ethylamine. The solution was

stirred overnight at room temperature. subsequently ZnO layers were deposited by spin coating in air under ambient conditions at 3900 rpm 60 seconds for PET substrates and 4500 rpm for 45 seconds when using glass substrates, each followed by a 15-minute thermal anneal at 150 °C in air. In each case this resulted in the formation of a 30 nm ZnO film that uniformly coated each substrate. To ensure optimum wettability, before depositing the active layer, ZnO layer underwent 5 minutes of UV-Ozone treatment.

Active layer deposition

The bulk heterojunction used throughout his study comprised polyy[(2,6-(4,8-bis(5-(2-ethylhexyl)thiophen-2-yl)-benzo[1,2-b:4,5-b']dithiophene))-alt-(5,5-(1',3'-di-2-thienyl-5',7'-bis(2-ethylhexyl)benzo[1',2'-c:4',5'-c']dithiophene-4,8-dione)] (**PBDB-T, PCE 12**) as the donor and 3,9-bis(2-methylene-(3-(1,1-dicyanomethylene)-indanone))-5,5,11,11-tetrakis(4-hexylphenyl)-dithieno[2,3-d:2',3'-d']-s-indaceno[1,2-b:5,6-b']dithiophene (**ITIC**) as the acceptor – which is referred to as (PBDB-T:ITIC). These materials were kindly supplied by Professor Martin Heeney at Imperial college London. The molecular weights were 117.406 kg mol^{-1} (PBDB-T) and 1.430 kg mol^{-1} (ITIC). The two materials were mixed in a 1:1 weight ratio in a and total concentration of 20 mg ml^{-2} of chlorobenzene:1,8-diiodooctane with a 99.5:0.5 volume ratio. The solutions were stirred overnight in the dark on a heated hotplate at 75 °C and subsequently spin coated at 2000 rpm for 60 s directly on top of the ZnO layer in air under ambient conditions resulting in 100 nm thick BHJ layer.

MoOx and silver deposition

Following deposition of the active layer films were transferred into a thermal evaporator to sequentially deposit MoO_x and silver layers. The evaporation was carried out a base pressure 2 x 10^{-6} mbar. First a 10 nm layer of MoO_x was deposited at a rate of 0.5 $Å s^{-1}$, followed by a 100 nm layer of Ag at a rate of 1.5 $Å s^{-1}$ for glass substrates and 0.5 $Å s^{-1}$ for PET substrates. As the PET is a soft substrate, a slower evaporation rate was selected to reduce any accumulation of residual stresses and the stress due to thin film deposition as discussed in Section 2.7 in Chapter 2. The final device structure is shown in Figure 3-3. Each pixel (total of six) is a single

device. The pixel area (0.45 mm^2) of the device is determined by the spatial overlap of the electrodes.

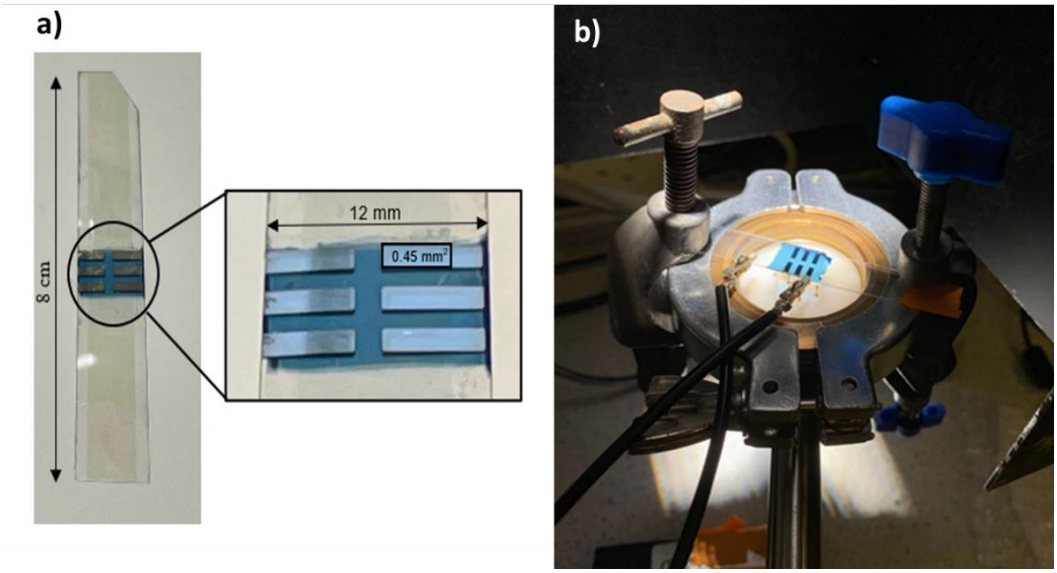

Figure 3- 3 a) Photographs showing an example of the OPVs fabricated on PET substrates, magnified image shows active layer materials with the device area shown for clarity, b) Photograph of PET based device under 1 Sum illumination whilst obtaining J-V characteristics.

Upon completion of devices their photovoltaic (PV) parameters were explored using a Newport Thermal Oriel Sol3A (Class AAA) Model 92250A-1000 solar simulator at an intensity of 1 Sun illumination (100 mW cm^{-2}, 1.25 mA, AM 1.5 G spectrum).

3.3 Device encapsulation

A thermal laminator was used to encapsulate the PET based devices. The lamination medium was 0.15 mm thick PET sheets sourced commercially. Prior to device encapsulation conductive tape was applied to the cathode contact of each pixel with the aid of carbon conductive paste, to which an electrical wire was soldered to allow electrical connectivity to the encapsulated layers (see Figure 3-4a). Lamination was then carried out, although the

internal laminator temperature wasn't recorded by the manufacturer, the temperature of the sample as it leaves the laminator was determined to be ~45 °C.

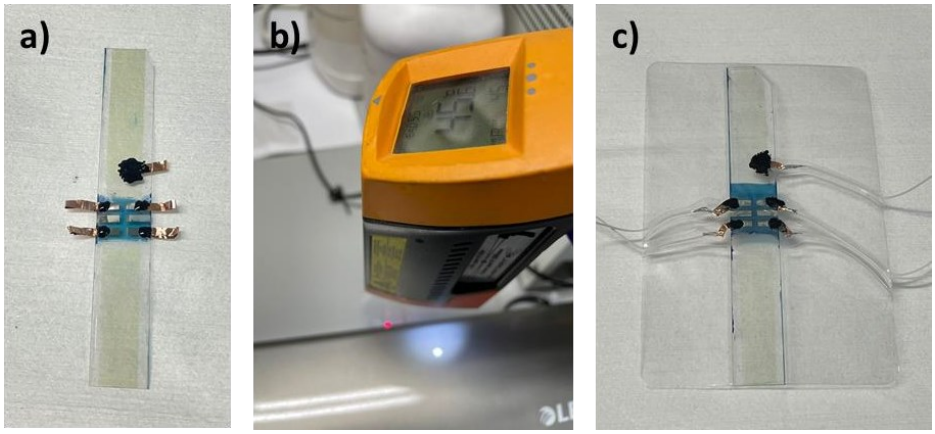

Figure 3- 4 a) PET based OPV with conductive tape attached to the pixels with the aid of carbon conductive paste. The cut on the top right side of substrate was made in all samples to distinguish the conductive side after cleaning the substrates. b) Infra-red thermometer showing the measured temperature samples after c) Encapsulated OPV with the wires attached to the pixels.

3.4 Mechanical characterisation

Three-point bending test

To study the influence of bending radius and cyclic bending on device performance, mechanical tests were carried out using a ZwickiLine Z2.5 (Zwick Roell) 3-point bend test instrument operated in cyclic loading mode. The system is fully digitalised as it uses a motor encoder and a load cell to collect data during the test. The load cell is attached to the top load frame, Figure 3-4a. The test protocol *i.e.* speed, distance and direction were pre-determined and subsequently uploaded to the software. A stainless-steel loading pin (attached to loading cell) measuring 1 cm in diameter was in contact with the back of the PET substrate, to avoid scratching or damaging the cell.

A compressive load was applied directly to the centre of the PET, which is aligned with the centre of the device as shown in Figure 3-4a, this ensured that the device would experience

maximum bending moment and maximum axial stress. To protect the device from scratching or damaging due to direct contact with loading pin, the PET side was put in contact with loading pin. Thus, it is believed that the OPV was under tension stress while the PET substrate was under compressive stress (see figure 4-3b). The neutral axis location was calculated and confirmed by FEA which will be further discussed in Chapter 5. The supporting pins were set to a separation distance of 70 ± 3 mm. The designed cyclic loading programme varied the distance travelled by the loading pin at a speed of 30 mm s^{-1}.

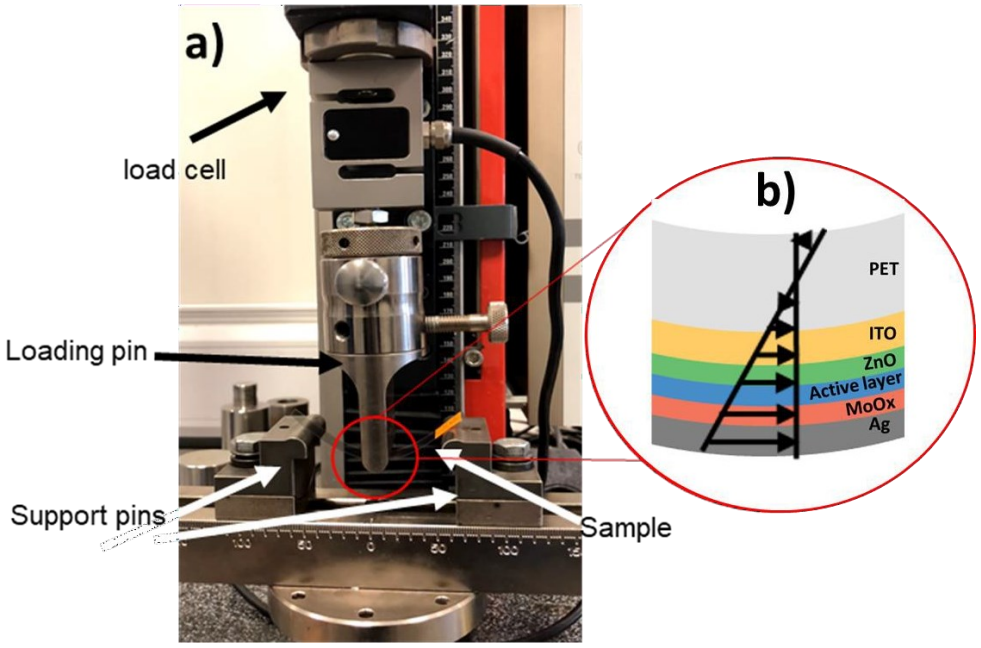

Figure 3- 5 a) Photograph of the Zwick Roell 3-point bending machine used. The sample is under 3- point bending resting on support pins separated by 7 cm with the loading pin directly at the centre of sample above the PV device. To reduce any damage caused by contacts the PET film side was placed in contact with the loading pin. b) Schematic representation of the expected stress distribution of tension and compression that was experienced by the OPV.

When programming the test protocol, the distance travelled by the loading pin (depth) (h) had to be added manually to obtain the required bending radius. This was calculated using differential geometry. In differential geometry, radius of curvature (r_c) is defined as the radius of a circular arc which approximates the curvature at that point. Hence, the radius of

curvature is infinite for a straight line and large for a line on bending path [129]. If the circular segment was used as an analogy with the three-point bending instrument shown in Figure 3-5a. Then Figure 3-6 can be used to set some assumptions to calculate the travel distance of the loading pin.

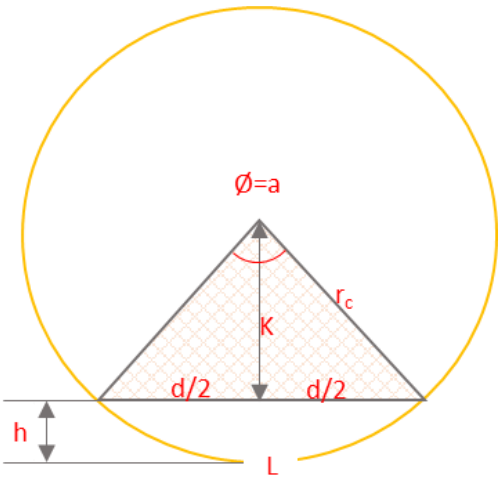

Figure 3- 6 Circular segment used to calculate the distance travelled by the loading pin (h) to bend the sample to a bending radius = r_c.

In Figure 3-6. L is the is length of the specimen (the length of the OPV substrate), h is the depth, d is the separation distance between the two supporting pins that the substrate rests on, r_c is the radius of curvature (bending radius) and *a* is the bend angle. Thus, (h) would be the distance travelled by loading pin (depth) to induce bending to the specimen equal to a bending radius of r_c. The depth can be expressed and calculated as follow:

$$h = r_c - K \qquad \text{Equation 3-1}$$

$$\therefore h = r_c - r_c \,.\cos\left(\frac{L}{2r_c}\right) \qquad \text{Equation 3-2}$$

Table 3- 1 The calculated distance travelled by the loading pin to allow for the required bending

Bending radius (cm)	2.7	5	10
Loading pin travel distance (mm)	25	15.3	7.9

Considering the device's potential application in consumer wearable electronics, the lower and upper limits of the bending radius were chosen as representative of a device curvature when worn around an adult's mid-upper arm of average circumference ($c \approx 33.1$ cm, $r_c \approx 5.3$ cm), and placed along the curvature of a human head of average circumference ($c \approx 55.2$ cm, $r_c \approx 8.8$ cm) [134]. Data were collected after 10, 50 and 100 bending cycles.

In-situ resistance measurements

To further understand the influence of 3-point bending on the resistance of the device, an in-situ experiment was designed, as shown in Figure 3-7.

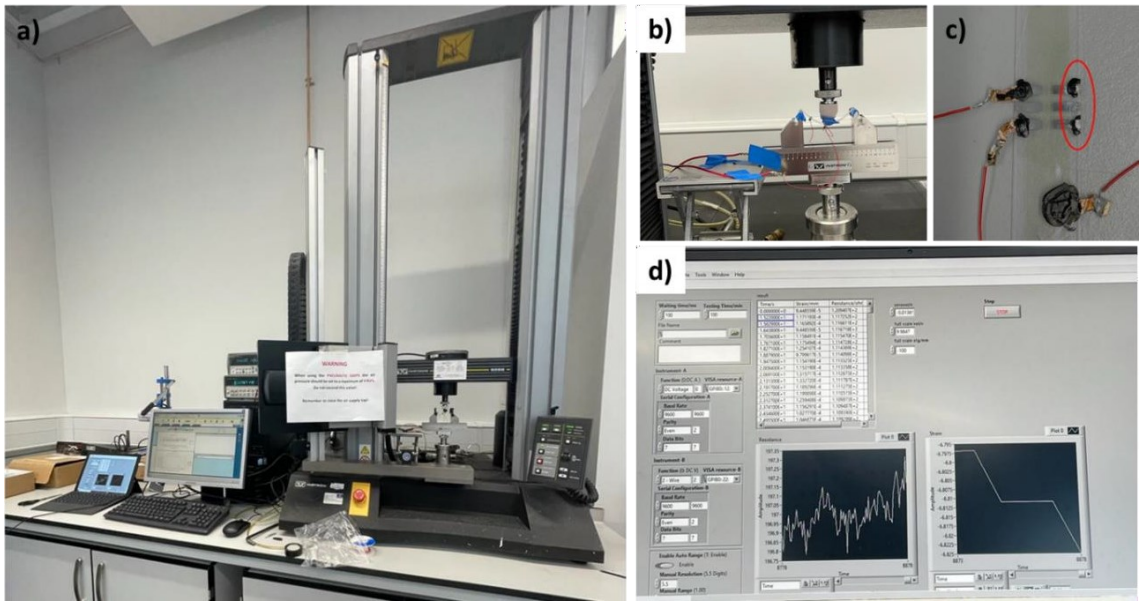

Figure 3- 7 a) Shows the in-situ setup to measure resistance while bending using a 3-point bending Instron (design 5566), attached to a digital multi-meter. b) The 3-point bending set up with insulating tape to isolate the sample from the metallic frame of the machine with wires attached to the digital multi-meter using crocodile leads. b) shows the method the sample was wired using carbon paste to glue the conductive tape to the electrons and the solder the wires on the other end of the tap. d) shows the LabVIEW software that was used to record the resistance and the displacement of the loading pin with respect to time.

Thin copper wires were attached to the electrodes (Ag and ITO) of the devices and placed on the 3-point bending setup on Intron model 5566 while being connected to an Agilent 34401A digital multi-meter. As explained above, the PET substrate was in direct contact with loading pin, thus the device experienced downward bending (See figure 3-7b). The metallic parts of the 3- point bending set up that are in direct contact with the device were covered with an insulating tape to provide electrical insulation between the machine frame and the sample. Both the mechanical data (compression) and the resistance were recorded simulatability via a LabVIEW code (Figure 3-7d).

The designed cyclic loading program varied the distance travelled as shown in Table 3-1 by a speed of 2 mm s^{-1} with total of 5 bending cycles. A slow speed such as 2 mm s^{-1} was chosen to avoid any movements of the connected wires to the device as indicated in Figure 3-7b, as going any higher than 2 mm s^{-1}, would oscillate these wires and thus, produce noisy signals. An upper and lower safety limit of the bending (distance travelled by the loading pin) were set to 0 mm and -100 mm respectively (the negative sign indicates the downward movement of the loading pin). This in return determined the range of voltage the digital multi-meter is operating in which was between -0.01375 V at 0 mm *i.e.,* when the sample is in a flat condition. A voltage of 9.9848 V at -100 mm was applied. Although the upper limit was never reached as the maximum travel distance was set to be 25 mm for 2.7 cm bending radiuses. It was chosen however to minimize noises when recording the data.

Creating contacts with the sample was a challenging part in this experiment. As it was done manually using conductive tape and carbon paste, the initial resistance of each pixel varied this can be seen in Chapter 5, Section 5.3. This is mostly owing to the fact at after attaching the wires to the pixels, and ensuring conductivity with carbon paste, the hot soldering that followed this step, would affect the adhesion of the conductive tape and, in some cases, it would snap off the sample due to handling and connecting thee wires with the digital multi-meter crocodile leads (see Figure 3-7c). This “snap off” within the program would be recorded as a resistance overload which could be interpreted as phenomena of mechanical damage within the device structure (delamination or fracture). Thus, it was important that when an overload of resistance occurs such as the cases noted in Figure 5-5a-b and Figure 5-10a, the entire sample is examined closely to ensure that it did not occur due to faulty wiring. Section 5-5 of this thesis will further elaborate on the wiring systems refinements.

However, it must be noted that the loading cell sensitivity *i.e.*, the accuracy of the mechanical data collected by loading cell is around 2% of its loading capacity. Thus, for a thin flexible sample (0.21 mm thick) such as those used in this work, a load capacity of 10 N in would ideally be the threshold, above which, the data collected of force/displacement are noisy as shown in Figure 3-8 and thus, might not be reliable. Both the ZwickiLine Z2.5 and Instron design 5566 mechanical testing machines had a loading cell of testing capacity of 5000 N. Thus, forces and stress analysis were obtained using finite element analysis (FEA). However, these machines allowed for cyclic loading tests for the bending radius that were of interest to this work.

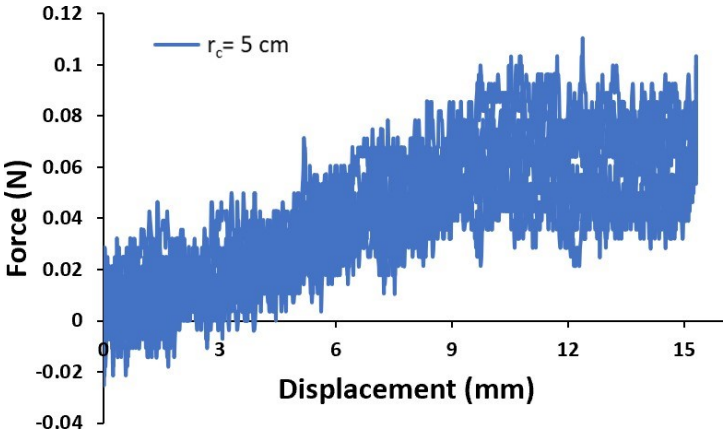

Figure 3- 8 Shows an example of the force/displacement figure extracted from the Instron during the 3-point bending cyclic test of an un-encapsulated cell with bending radius of 5 cm. The figure shows a noisy signal as the loading cell capacity is higher than the ideal limit (10 N) for thin samples like the ones used in this work.

Finite Element Analysis (FEA)

Finite Element Analysis (FEA) uses numerical technique to solve differential equations and is capable of simulating many physical effects, including stress, vibration, motion, heat transfer and fatigue. In this work, FEA was employed to quantify the stress distribution across the thickness of the OPV structures, to determine the position of the neutral axis as well as to study the impact of encapsulation of the stress distribution. Acknowledgements to Gorge Morgan who helped conducting these simulations.

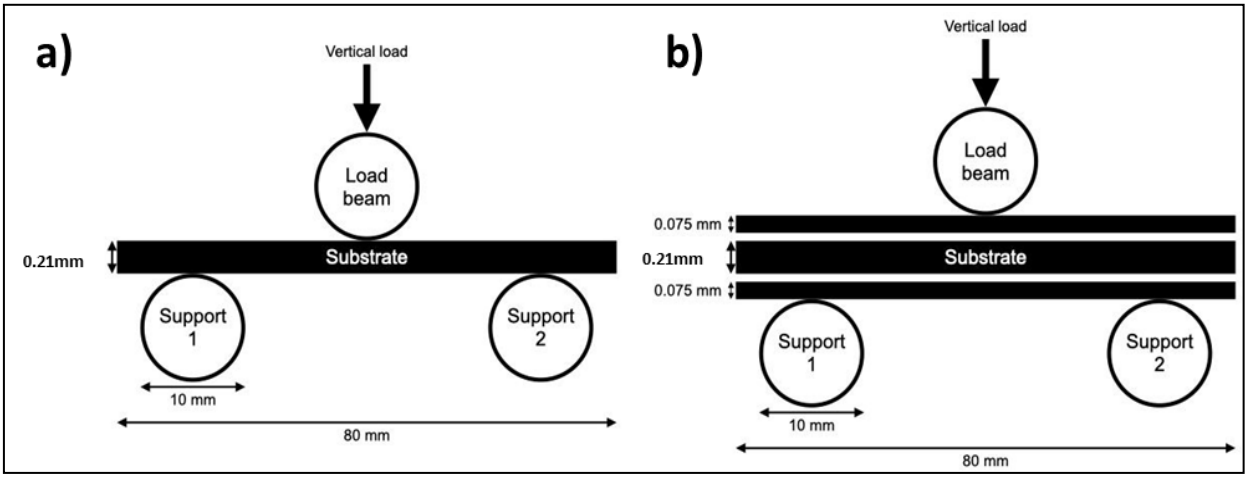

Figure 3- 9 Schematic representation simulated skitch. a) shows the dimensions and supports used for simulating 3 -point bending of un-encapsulated cell while b) represents the dimensions and supports used to simulate 3-point bending of encapsulated cell. It was assumed that the mechanical characteristics will be drawn from the PET substrate thus, only PET substrate was taken into accurate. This assumption was made because the device layer's thickness is negligible compared to the PET substrate thickness.

COMSOL Multiphysics software was used in this study. A base of 1.2 cm x 8 cm PET substrate was sketched with thickness of 0.21 mm (See Figure 3-9a). The software library had PET pre-loaded meaning that key material properties *i.e.* Young's modulus, Poisson's ratio, bulk and shear moduli were accessible. As indicated in Figure 3-9, constraints were added to the lower edge of the substrate to mimic the real case scenario and loading pin was added. The simulation conducted in this work, was based on displacement control rather than force control. Meaning, that that loading pin was simulated to move downward to different displacement length to simulate the required bending radius. These distances were as per the calculations made in Table 3-1. Nonetheless, through the simulation the forced required for such bending were extracted, which are presented in Table 3-2. Although the simulated forces do not match those raw force/displacement exported from the 3-point bending test, this could be due to the sensitivity of the load cell.

Table 3- 2 Shows *the exported via the FE analysis to result in a 3-point bending of un-encapsulated cell with the required bending. Understanding by that the forces used by the 3-point bending machine*

Bending radius (cm)	**2.7**	**5**	**10**
Force (N)	0.425	0.260	0.134

The main challenge in fabricating the device multilayers is that some of the materials used in fabricating OPV are novel and consequently their intrinsic mechanical properties are not widely studied and/or reported. In addition, the small thickness of some of the layers (≥ 10 nm) meant that running the simulations was computationally intensive and would often crash. Thus, the simulation focused only on the PET, as the main mechanical characterises extracted from the simulation originated from the PET layer. To simulate the encapsulation layer, (see Figure 3-9b) the tool "section" was utilised, and upper and lower layer of the encapsulating poach were sketched each with thickness 0.075 mm. These layers are then "attached" together via a "partition tool" which meant that now all the layers behave like one isotropic body. Which means that delamination between the interlayers or within the encapsulation would not be detected in the simulation. The forces extracted from simulating encapsulated substrates are in Table 3-3. Nonetheless, FEA provided information about the neutral axis as well as the impact of encapsulation on the stress distribution on the substrate which will be disused later in Chapter 5.

Table 3- 3 The force used in FEA to result in a 3-point bending of encapsulated cell with the required bending analysis.

Bending radius (cm)	**2.7**	**5**	**10**
Forces (N)	2.016	1.234	0.637

3.5 Optoelectronic characterisation

Uv-Vis's spectroscopy

UV-Vis's spectroscopy was used to measure the optical transmittance and reflectivity of the materials and substrates over the 220 - 1400 nm wavelength range. In this work, a Shimadzu UV-2600 instrument was used, an integrating sphere was added to measure the reflectivity. A background correction of the data was obtained by subtracting the spectra of glass/ITO and PET/ITO substrates.

3.6 Electrical characterisation

Four-point probe

Sheet resistance (R_{sheet}) is an electrical property used to characterise thin films with conducting and semiconducting materials. As the name indicates, it's a lateral resistance technique, which means it measures the resistance between the opposite sides of the sample square. Sheet resistance can be defined as follows:

$$R_{sheet} = \frac{\rho}{t} \qquad \text{Equation 3-3}$$

Where ρ is resistivity and t is the film thickness. The unit of this equation is Ω/□ as it represents the resistance between the opposite sides of the square rather than the bulk resistance [135]. The primary technique for measuring sheet resistance is a linear four-point probe which consists of four electrical probes as illustrated in Figure 3-10. Measurements are made by applying a current across the outer two probes while measuring the voltage drop across the inner probes. The method was used to measure the sheet resistance of ITO before and after bending. This was done by one of our group members Ryley Ratnasingham.

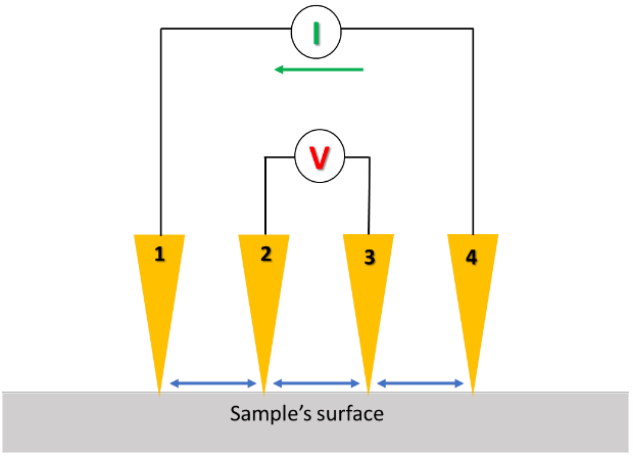

Figure 3- 10 Shows a schematic representation of four-point probe. The four probes equally spaced and are shown here in contact with the sample's surface. A current (I) is passing through probe 1 and collected by probe 4, while probes 2 and 3 are measuring the voltage drop.

3.7 Structural and morphological characterization

Surface profilometer

Profilometry was used to measure the thickness of the as deposited layers and complete devices (Dektak D150). In this technique a stylus tip is drawn down in contact with the sample. The tip then moves across the layer until reaches an interface at which the substrate is exposed. The tip maintains contact via a force applied by the machine, the movement across the sample (vertical displacement) is plotted by the software to keep track of the interface region. With the glass substrate when measuring the thickness of the active layer (soft sample; polymer), the substrate was exposed by simply scratching. However, with the PET substrates, tape was used to mask a section of substrate while spin-coating, the tape was removed during the thickness measurement. This was done to avoid permanent deformation of the substrate by scratching which could affect the measurements.

Atomic force microscopy

Atomic force Microscopy (AFM) was utilised in this study to image the surface of the thin films to analyse film morphology and roughness. AFM is advantageous as it provides high resolution lateral imaging, 0.1 nm, of a variety of surfaces, soft and hard, without the need for additional sample preparation steps [136]. Measurements are carried out in air. The instrument is well-insulated from vibration. AFM has three modes of operations; tapping, contact and non-contact. Regardless of the operating mode, AFM set up consists of a sharp tip (made of Si) that measure forces and is connected to a spring cantilever. The vertical movement of the spring cantilever is measured and recorded. This vertical movement is resulted from the tip interaction with the topological features of the sample. Feedback electronics then measure the changes between the tip/sample interaction and correct the parameters to maintain a constant distance between sample and the tip. In the system used in this study, the back side of the cantilever is coated with a highly reflective material which then reflects the laser off the tip into a photodiode. The signal produced from the photodiode is then analysed and the surface topography is imaged [136]. When the tip is at a finite distance of the sample and there is no interaction, the force between the two is zero. However, as the tip approaches the sample, an attractive weak long-range van-der Waal's forces are detected by the tip resulting in a non-contact operational mode. As the distance between the tip and the sample reduces, an attractive short-range van-der Waals forces are detected by the tip. As the tip approaches the sample's surface, short-range repulsive forces are generated between the tip and sample's surface. In a tapping mode, the tip is operating by an alternative short-range attractive and repulsive forces whereas in a contact mode, the tip is operating under repulsive forces only. Although contact mode allows for high resolution images, it is not suitable for soft substrates and polymers used in this work [137]. Therefore, for this work, tapping mode was utilised. Thus, the tip is within intermittent contact with the sample. This means that spring cantilever oscillate closer to its resonance frequency and as the tip gets closer to the sample, the feedback electronics edit the amplitude and reduces it, to ensure that the force applied to the sample is kept constant. For this work, a Bruker Innova AFM was utilised to scan an average of five 5 x 5 μm^2 with the amplitude of 1 Hz. Image analysis and roughness as a root mean square values were extracted using Gwyddion software.

Chapter 4

Fabrication of flexible OPV and initial testing of performance parameters under 3-point bend testing

4.1 Introduction

In this chapter, we begin with a detailed analysis of the optical and morphological properties of ITO coated PET substrates used for the preparation of flexible devices and the impact of processing on the intrinsic properties. The performance of OPV devices prepared using PET substrates will be evaluated after optimisation and compared with conventional devices prepared using rigid glass substrates. A direct comparison between devices is in this case was possible as both are obtained from a common supplier with an ITO thickness of around 250 nm and measured sheet resistance of 13.6 Ω/□. This chapter will also cover the ambient stability of PET based OPV devices as the devices have been fabricated and mechanically tested under ambient conditions. Finally, this chapter will showcase the initial results regarding the Influence of 3-point bend testing on flexible OPV device performance.

4.2 Device optimisation

To fabricate flexible OPVs it was necessary to optimise the recipe used for the overall device structure. The first step in this process was to evaluate the PET based ITO and compare with ITO on glass by measuring the optical, electrical, and morphological properties of each. The BHJ processing PBDB-T:ITIC was selected as an active layer (Chapter 3, Section 3.3) as similar had been previously reported with a device PCE of 11.2 % reported on glass/ITO substrate [53]. The same structure and blend of BHJ was fabricated on PET/ITO based substrates with an 8.86% champion PCE reported (note device area of 1 cm^2) [138]. Although the group of Ma

have reported that a device with PBDB-T:ITIC BHJ which was fabricated on PET/ITO substrate, maintained 89% of the initial PCE after 1700 hours of aging inside the glovebox under N_2 [139]. A main concern within this study was the ambient air stability which wasn't reported in literature, whereas in this work, the fabrication process, mechanical testing, and performance parameter were all carried out under ambient conditions within the laboratory environment. This section will cover the steps taken to optimise the device performance in order to allow tracking the effect of mechanical bending on the device's performance. This section will also cover the ambient stability test of an un-encapsulated device.

Optical properties

The first step was assessing the transparency and reflectivity of the substrates before and after the addition of 30 nm of ZnO, which serves as the electron transport layer (ETL) in completed devices. The data in Figure 4-1 shows the measured transmission and reflectance data. The transmittance spectra for both substrates are comparable, with the glass substrates having a slightly better transparency across the UV and visible spectral regions. In PTE/ITO/ZnO reflectance spectra a Fabry Perot oscillations can be observed, these are indicative of a sharp optical interface between the substrate and the ZnO layer.

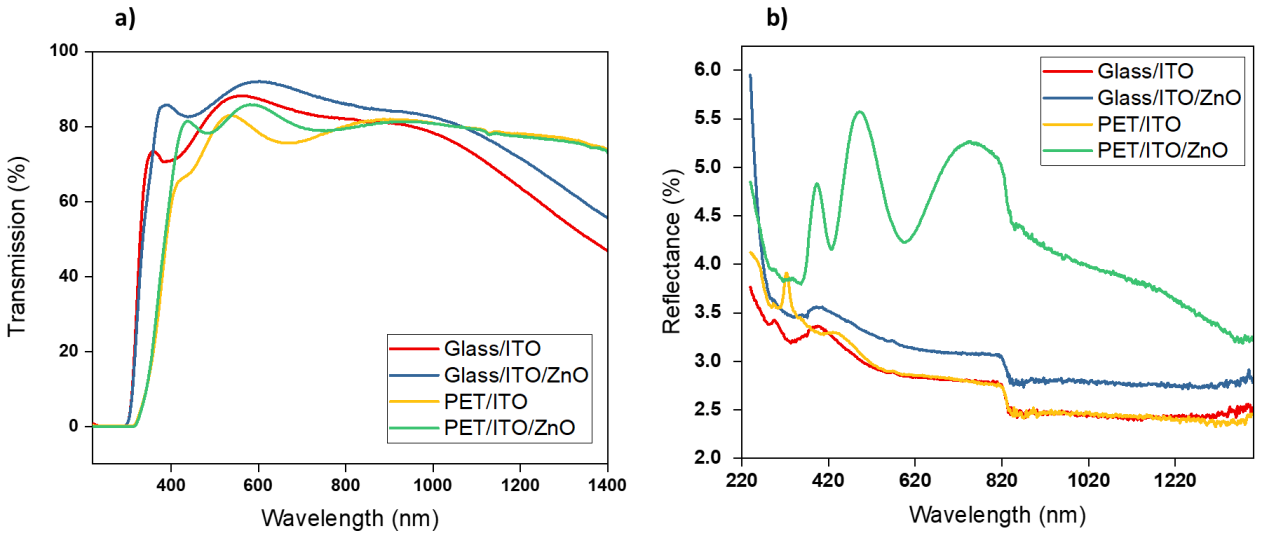

Figure 4- 1 a) Transmission spectra of glass/ITO and PET/ITO before and after the addition of 30 nm thick spin coated ZnO on both substrates. b) Reflectance spectrum of glass and PET substrates with pre-patterned of 250 nm ITO layer and after the addition of 30 nm thick electron transporting layer ZnO.

Film Morphology

The topography of the substrates before and ZnO layer deposition, were examined via atomic force microscopy (AFM). Images were obtained here in tapping mode and show that the ITO film on PET has a significantly lower root means squared roughness (RMS roughness, 1.32 nm, compared with the ITO on glass (RMS = 5.43 nm), (See Figures 4-2 a and c). To account for these differences in RMS modifications, spin coating conditions of ZnO had to be altered to rectify the difference in roughness between the two substrates. In which, ZnO spin speed was 3900 rpm for 60 seconds for PET/ITO substrate, whereas the spin speed of ZnO on top of glass/ITO substrate was 4500 for 45 seconds. Thus, ensuring the thickness of ZnO for both substrates would be 30 nm. This was important to ensure that the fabrication of PET/ITO based devices would be optimised and comparable to published glass-based devices for the structure used. After spin coating ZnO layer, the morphology and resultant RMS roughness where comparable for both substrates (see Figures 4-2 b and d).

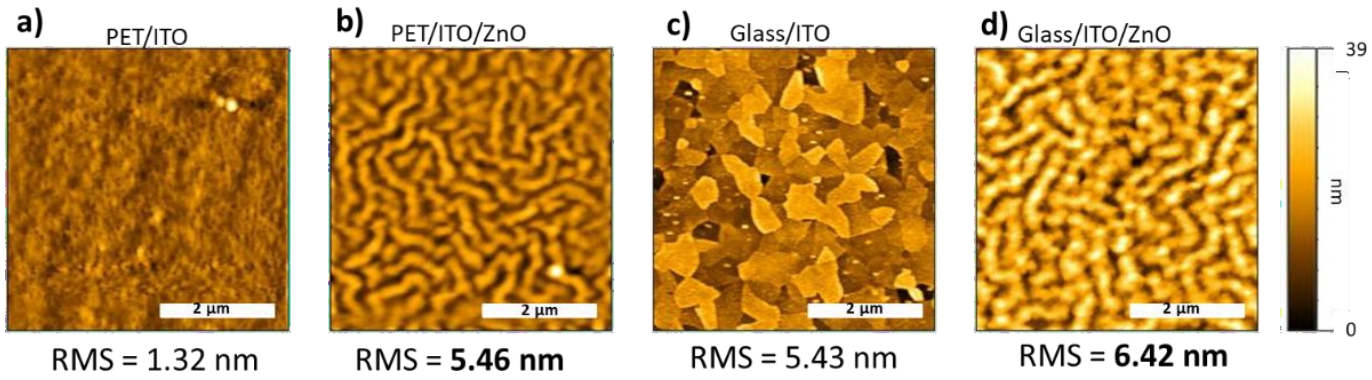

Figure 4- 2 Tapping mode AFM height images of a) PET substrates with pre-patterned 250 nm of ITO (as obtained from supplier). b) PET/ITO substrate with spin coated 30 nm thick ZnO layer. c) Glass substrate with pre-patterned 250 nm of ITO (as obtained from supplier). d) PET/ITO substrate with spin coated 30 nm thick ZnO layer. ZnO layers in all substrates wear subjected to 150 °C post- deposition treatment. The RMS roughness values are an average of 5 different areas within the sample.

OPV Performance parameters

As mentioned above, the device recipe and structure were taken from a pre-stablished and optimised recipe based on a glass/ITO substrate [53]. Therefore, to fabricate the same recipe, on a PET/ITO based and obtaining a compatible device performance to the glass/ITO based device, three things be factors had to be taken into consideration. Starting with, the roughness of the PET/ITO layer, in which, had the spin conditions remained the same for ZnO in both glass/ITO substrate and PET/ITO substrate, the thickness of the ZnO layer was around 6 nm. This in return effected the performance of the PET/ITO (See Figure 4-3a). The second factors that reduced the performance parameters of PET/ITO based devices, was observed upon fabricating different batches of devices on different days, was solution aging. It was noticed that if the active layer solution was older than one week, then the device performance would reduce (See Figure 4-3b). It must be noted that the active layer solution was prepared under ambient conditions and was stirred on top of the hot plat at 75 °C outside the glovebox. The final factor that was taken into consideration from the very beginning, is the evaporation

rate of MoOx and Ag layers. As the PET/ITO substrates is soft, lower evaporation rates of 0.5 $Å s^{-1}$ was chosen for both layers. Figure 4-3d shows the optimised devices, after taken all three factors into consideration.

As seen in Table 4-1, show examples of individual devices, where flexible OPVs 1 and 2, show the effect of thin ZnO layer, in flexible OPVs 3 and 4, the thickness of ZnO was optimised to 30 nm but the active layer solution used was a week old. Finally, Flexible OPVs 5 and 6, are the optimised devices in terms of ZnO thickness and freshness of the active layer solution. A lot of studies have been published regarding the effect of ZnO thickness on the performance of OPV, in which literature reports that reducing ZnO thickness in an OPV device below 10 nm thick, ZnO layer's transport properties would suffer due to a large surface to bulk ration, which in returns create morphological defects resulting in electron trapping [140]. In addition, low thickness of ZnO layer could mean poor coverage over the electrode and thus, creating current leakage due to pin holes, increasing by that the shunt resistance, and thus reducing the FF as the shape of the J-V curve would be affected [140, 141]. This was observed in both flexible OPVs 1 and 2, where when compared to the optimised devices, the shape of the J-V curve is improved after increasing the thickness of ZnO to 30 nm, as well as improvements in FF, V_{oc}, J_{sc}. Moving to flexible OPVs 3 and 4, it becomes clear using a fresh solution impacts the value of J_{sc}, thus, it is expected that aging the active layer solution has an impact on the light absorption efficiency. Although the effect of solution aging is outside the scope of this work, it was important to ensure that the active layer solutions are made no longer three days from the day the devise were fabricated.

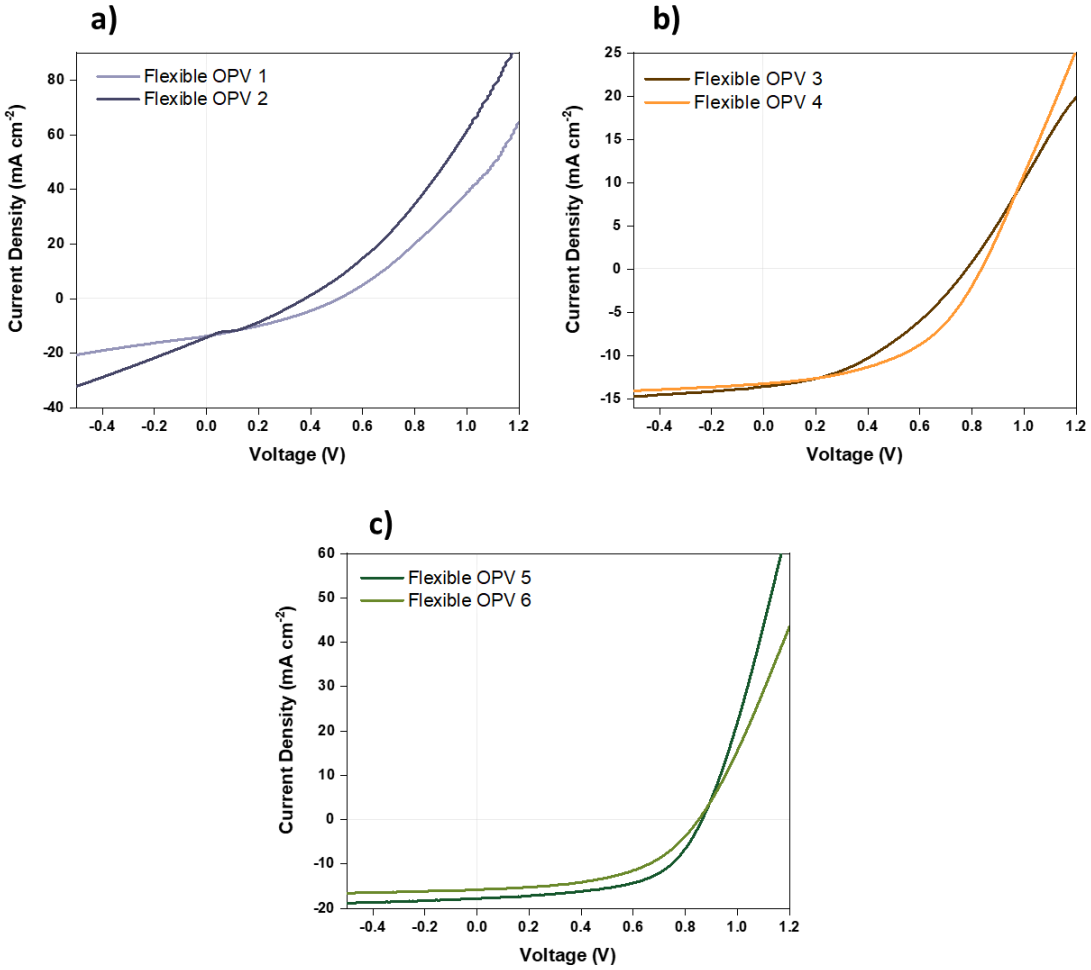

Figure 4- 3 J-V curves of flexible OPV devices where a) the devices were affected by thin ZnO layer b) devices were affected by the active layer solution aging and c) devices with optimised ZnO thickness and fresh active layer solution.

Table 4- 1 Performance parameters of flexible OPVs effected by thin ZnO layer, flexible OPVs that were affected by the active layer solution aging and flexible OPVs with optimised ZnO thickness and fresh active layer solution.

		J_{sc} (mA cm^{-2})	V_{oc} (V)	FF	PCE (%)	R_s (Ω)	R_{sh} (Ω)
Effect of thin ZnO layer	Flexible OPV 1	-13.8	0.53	0.32	2.27	13.46	52.5
	Flexible OPV 2	-15.2	0.39	0.28	1.66	13.73	36.7
Effect of solution aging	Flexible OPV 3	-13.6	0.78	0.42	4.51	25.46	306.29
	Flexible OPV 4	-13.2	0.84	0.48	5.27	18.2	233.7
Optimised devices	Flexible OPV 5	-17.8	0.87	0.56	8.67	8.14	542.8
	Flexible OPV 6	-15.8	0.85	0.51	6.87	12.42	253.9

It must be noted that even after optimisation, the devices' performance parameters would vary from batch to batch as seen in Tables 4-1 and 4-3, nonetheless, it is the trends and changes in the performance parameters with mechanical testing that was taken into consideration. Therefore, optimising the device was important to allow observation of the changes due to mechanical degradation. Figure 4-4 shows the J-V curves of devices prepared on glass and PET, the performance metrics obtained from these data are summarised in Table 4-2. The deviation of the PET based OPV towards the right in the first quadrant indicate a loss due to series resistance. This could arise from contact resistance with the electrodes due to the way the flexible OPV was measured using mini crocodile clips leads. This effect is also observed by the fluctuation of R_s values between batches as presented in Table 4-1. The behaviour of PET based OPV and glass based OPV are comparable. The results show that the fabrication of a flexible OPV under ambient conditions was successful.

Table 4- 2 Performance parameters of glass based OPV and PET based OPV.

	J_{sc} (mA cm^{-2})	V_{oc} (V)	FF	PCE (%)	R_s (Ω)	R_{sh} (Ω)
Glass based OPV	-15.5	0.87	0.58	7.78	8.9	203.1
PET based OPV	-17.8	0.86	0.56	8.6	11.1	209.8

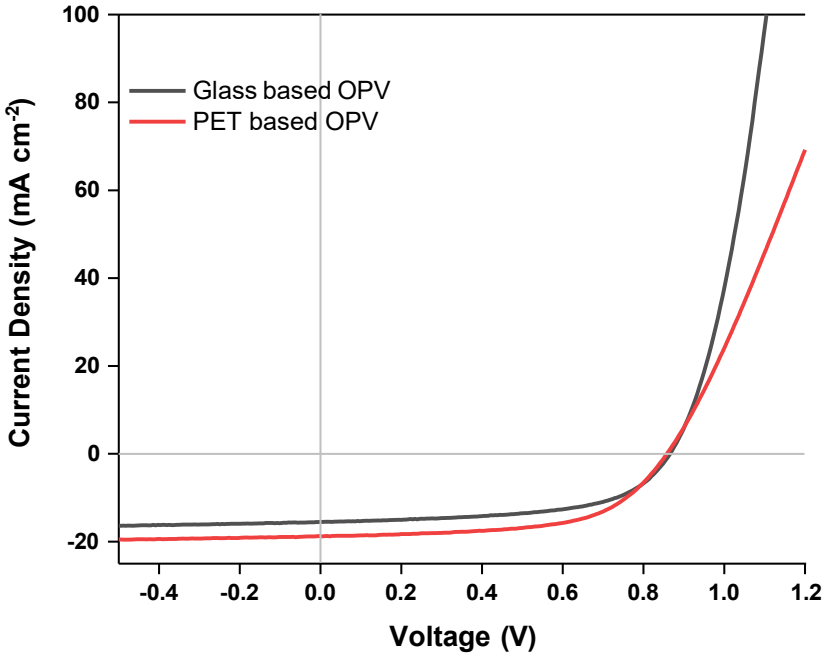

Figure 4- 4 J-V curves illustrating the performance of the best preforming *glass based OPV and PET based OPV under illumination.*

Ambient stability of flexible OPVs

As previously discussed, reports in the literature of ambient stability of an un-encapsulated flexible OPVs and more specifically with the structure and BHJ blend used in this work are lacking. Whilst fully understanding the degradation mechanisms and pathways is beyond the scope of this work, it was necessary to understand the timeframe over which degradation would occur. This, in order to define a window of time in which mechanical testing can be carried out. Device testing was carried out at regular intervals over a 53 hour period, with the devices being stored and also tested in ambient conditions, Figure 4-5. It can be seen that all performance metrics remain within 10 % of their initial values for around 20 hours, after which device performance drops off dramatically. The J_{sc} drop could be the result of active layer degradation process which effected the light absorption efficiency or due to a drop in exciton dissociation efficiency at the donor/acceptor interface within the blend. It has been reported that, PBDB-T:ITIC BHJ blend show a continuous vertical phase separation when aging in ambient air at different timing ranging from 20 minutes to 25 hours. Thus, forming a PBDB-T rich top surface and ITIC-rich bottom surface of the active layer [142]. These changes induce unfavourable exciton separation resulted from poor interface between donor and acceptor. In addition to that, it has been reported that when PEDOT:PSS is used as hole transporting layer, the interfacial interaction between 2-(3-oxo-2,3-dihydroinden-1-ylidene)malononitrile (INCN) within ITIC molecules (upon the vertical phase separation) and the acidic PEDOT:PSS, leads to degradation of the ITIC molecules. Thus, reducing the V_{oc} of the device [142, 143]. However, it has been reported that upon replacing PEDOT:PSS with MoOx, the V_{oc} of the device can maintain stable when aging under ambient conditions [144]. Which agrees with the data collected in this work (See Figure 4-5) in which, the stability of the V_{oc} could suggest that the electrodes and electrode/active layer interface remained intact. When comparing the stability test of this work and published work in literature, for an inverted ITIC:PBDB-T based OPV, the devices maintained their ambient stability for up to 10 days. However, it must be noted that all these published studies reported in this section have been conducted on encapsulated glass based OPV that have been fabricated inside the glovebox. This could explain the intensity and speed of the ambient degradation of the devices fabricated in this work. Nevertheless, the permeability and water absorption of PET doesn't play a major role in this case, according to literature, the contact resistance between PET substrate and ITO

layer experienced sharp increase only after being in a relative humidity of 90% for 55 days [145]. Whereas the work in this thesis was conducted under ambient conditions of a laboratory of at temperature ranges from 20 °C to 25 °C with humidity of around 30%. In addition to that, water absorption percentage of PET is considered one of the lowest when condensing plastic based flexible substrates which ranges between 0.4% to 0.6% [146]. From these results the window in which mechanical testing was to be carried out could be defined. Each device discussed in this work has been fabricated, mechanically tested, and analysed within 24 hours. Furthermore, batches of devices were prepared such that the same batch was used at each bend radius to ensure the data could be compared meaningfully.

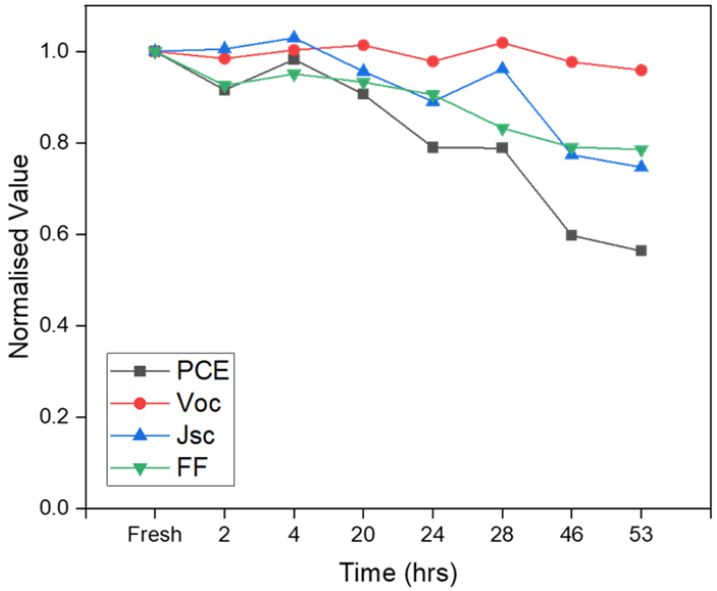

Figure 4- 5 Evolution of performance of un-encapsulated OPVs measured over 53 hours. Devices were stored and tested in ambient conditions.

4.3 Influence of 3-point bend testing on flexible OPV device performance

Force/displacement curves of the PET substrate with the devices fabricated on top after cyclic 3-point bending of the three different inner bending radiuses, namely 10 cm, 5 cm and 2.7 cm that were used in this study are illustrated in Figure 4-6. To minimise the noises in the curve, the force/displacement curves are only for the first 10 cycles. As stated in Chapter 3 Section 3.4.2, the sensitivity of the loadcell hinders the accuracy of the results and thus, data presented in Figure 4-6 are noisy. Nonetheless, a trend can be extracted from the cyclic force/displacement behavior as the bending radius reduces. At 10 cm bending radius, the PET sample was tested within its elastic region (Figure 4-6a). At 5 cm bending radius, once the loading pin moved downwards a distance of around 9 mm from the flat position, the samples enter its plastic region. However, as noted by the unloading behavior, the sample exhibits a recovery of the non-permanent deformation (Figure 4-6b) . This explains the fact that sample (PET substrate), dose not experience any permanent plastic deformation to its shape even after 100 bending cycles. The same features are observed at 2.7 cm bending radius, where samples surpass the elastic region into the plastic region (Figure 4-6c). Upon unloading and reducing the force experienced by the sample, a recovery of the non-permanent deformation occurs, keeping the substrate from changing its shape after the cyclic bending, meaning that, the sample experiences elastic strain during the cyclic bending test. Therefore, regardless of the bending radiuses or number of bend cycles studied, the flexible OPVs' substrates did not experience any permanent plastic deformation to their shapes. However due to the noise it is hard to extract any further information regarding the force/displacement behaviour of the PET based devices. Nonetheless, upon encapsulating and increasing the thickness of the sample, the curves become less noisy, and the trend of elastic strain becomes clearer. This is presented in Append

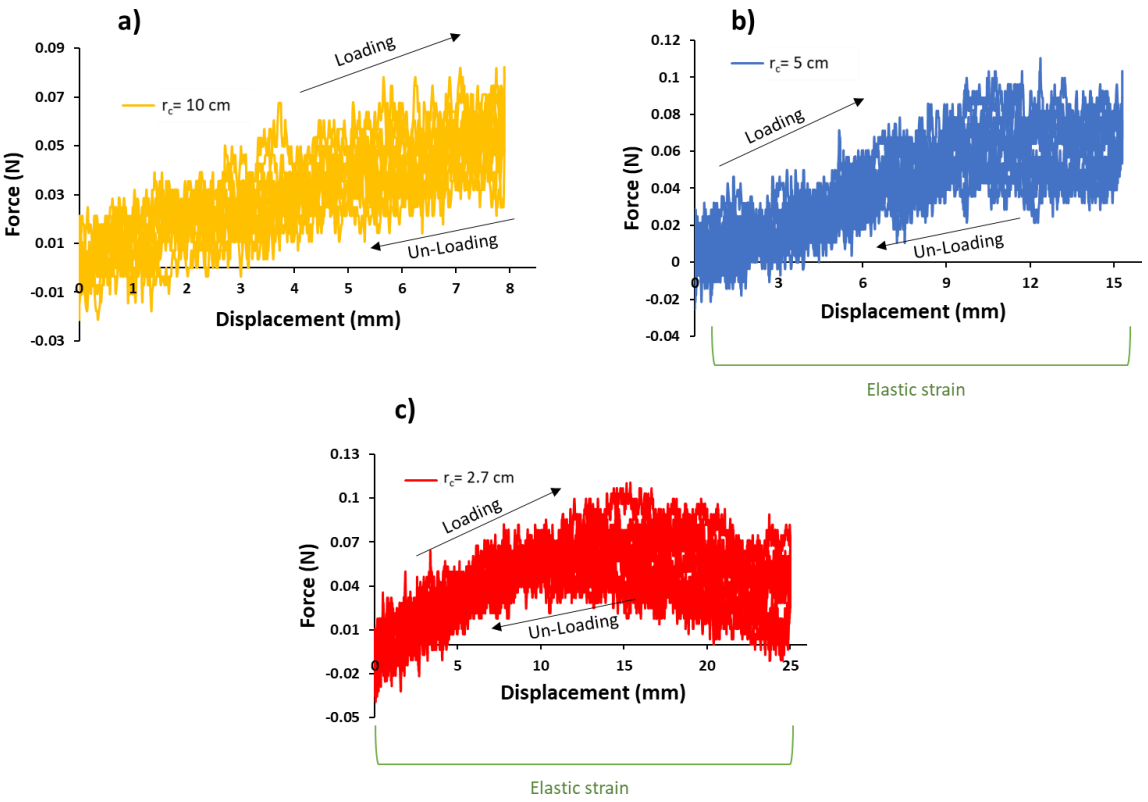

Figure 4- 6 Force/displacement curves of cyclic 3-point bending of PET substrate with devices fabricated on top a) 10 cm bending radius, b) 5 cm bending radius, and c) 2.7 bending radius.

Here the initial results investigating the influence of 3-point bend testing on the performance parameters of flexible OPVs is investigated. With the three bending radiuses, 10 cm, 5 cm and 2.7 cm. As shown in Figure 4-7, each cell was measured for a total of 100 bending cycles under each condition with J-V data obtained on pristine films, and following 10, 50 and 100 bend cycles.

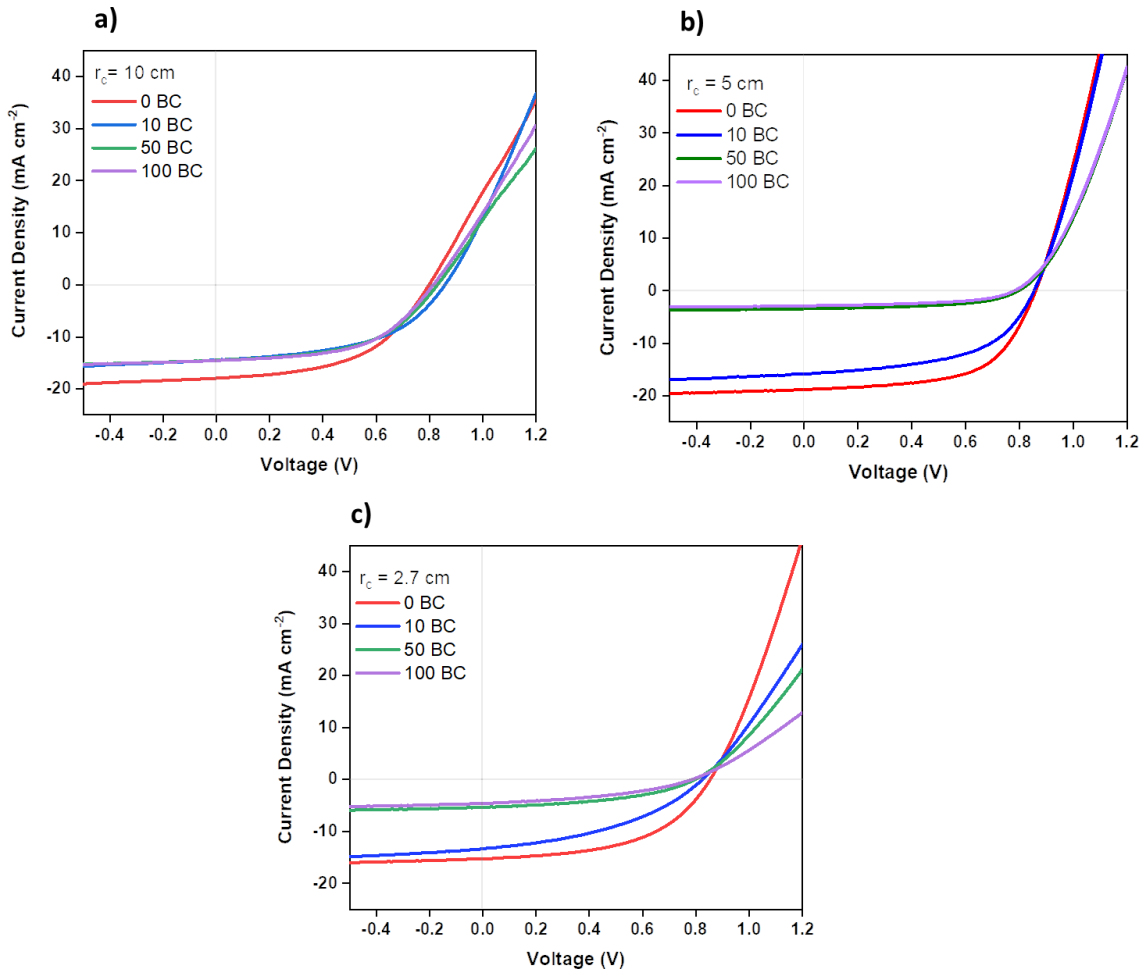

Figure 4- 7 Shows the evolution of device J-V properties for devices under 3-point bend testing with a) r_c= 10 cm b) r_c= 5 cm and c) r_c= 2.7 cm. Each curve is obtained from a single OPV

Table 4- 3 shows the effect of 3-point bending on the performance parameters of 3 different flexible OPV after undergoing 10, 50 and 100 bending cycles, each with different bending radiuses of 10 cm, 5 cm and 2.7 cm.

Bending Radius (r_c)	**Bending cycles (BC)**	**J_{sc} (mA cm^{-2})**	**V_{oc} (V)**	**FF**	**PCE**	**R_s (Ω)**	**R_{sh} (Ω)**
10 cm	0	-18.2	0.80	0.51	7.29	11.6	436.9
	10	-14.5	0.86	0.50	6.23	13.9	399.7
	50	-14.5	0.83	0.52	6.23	15.5	310.5
	100	-14.5	0.81	0.53	6.32	15.8	340.1
5 cm	0	-18.8	0.86	0.60	9.62	7.61	525.6
	10	-15.9	0.85	0.54	7.27	9.1	320.7
	50	-3.45	0.80	0.53	1.45	33.6	416.5
	100	-2.9	0.78	0.53	1.18	40.7	680.4
2.7 cm	0	-15.3	0.85	0.51	6.69	12.2	252.4
	10	-13.4	0.83	0.41	4.50	20.7	310.8
	50	-5.3	0.80	0.44	1.87	38.3	540.3
	100	-4.6	0.79	0.40	1.45	57.4	576.6

Analyses of the bend test data reveal that for all bending radiuses, the start of bending results in a drop in device performance, specifically a reduction in J_{sc}. With a bend radius of 10 cm J_{sc} remains constant after 10 bend cycles and the overall device performance remains unchanged following more bending cycles (Table 4-3). As mentioned, the PET substrates did not experience any change in their shapes regardless of the bending radius used or number of bending cycles, thus, the reduction noticed in J_{sc}, indicates that the permanent deformation is within the device itself has occurred while bending. The V_{oc}, J_{sc}, FF, PCE, R_s and R_{sh} are

plotted as a function of bending cycles in Figure 4-8. Which shows the average data of four flexible OPVs, all normalised to their pre-bending values. Analysis of the R_s data Figure 4-8b, shows that R_s increases when bending starts for all bending radiuses however remains fairly constant for a bend radius of 10 cm. Increasing the bend radius to 5 cm similar behaviour is seen up to 10 bend cycles, followed by a sharp increase in R_s that continues with more bending. At 2.7 cm there is again an increase for 10 bend cycles that continues to increase with increased bend cycles. From analysis of these data, it is clear that devices subjected to bend test with radiuses of 2.7 cm and 5 cm, are significantly affected by the testing, with J_{sc} (Figure 4-8d) being the parameter that is reduced owing to increases in device Rs.

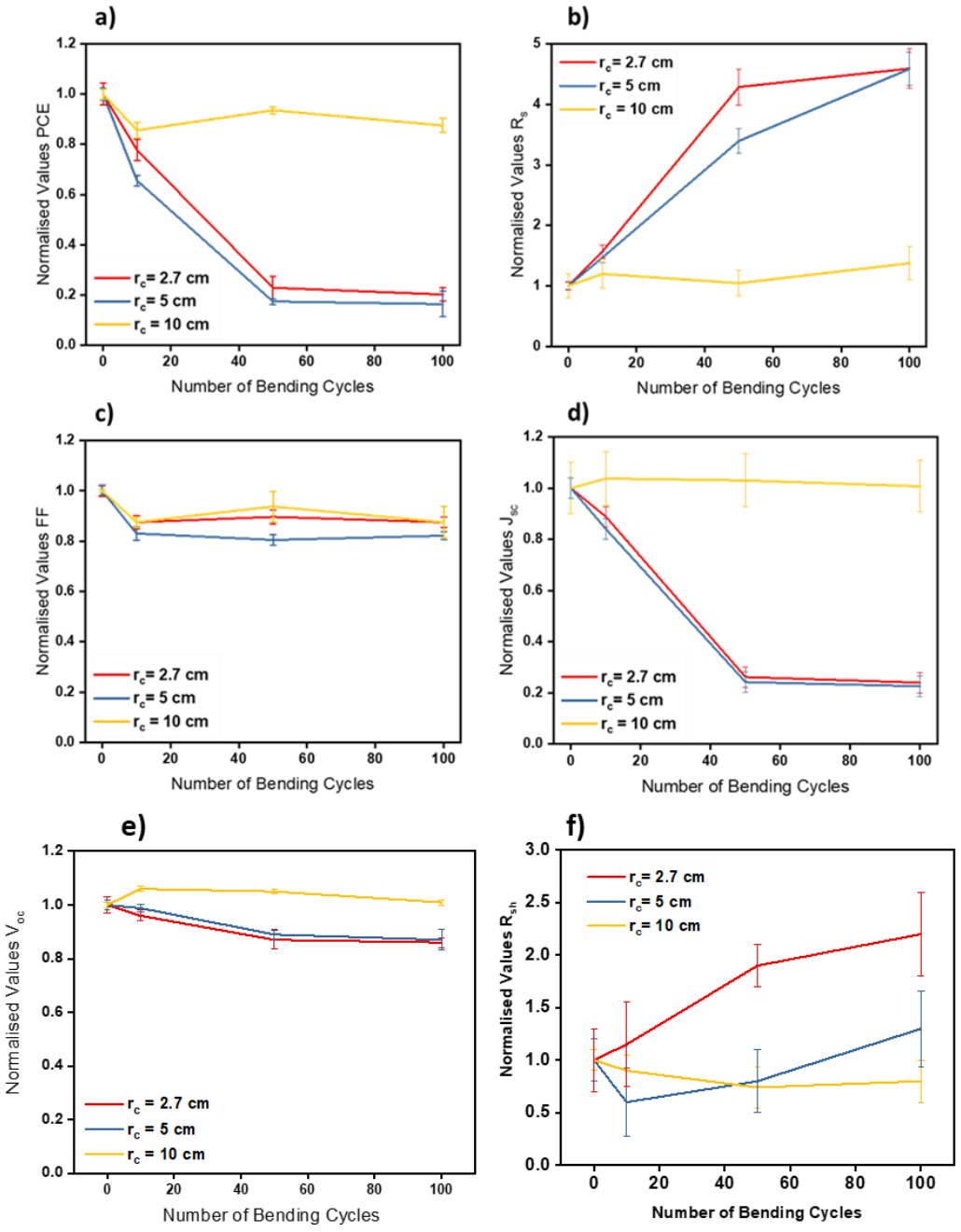

Figure 4- 8 illustrates the normalised values of the flexible OPV performance parameters after 10, 50 and 100 bending cycles with different inner bending radius of 2.7 cm, 5 cm and 10 cm. The normalised values are an average of 4 flexible OPV.

From the trends observed by the normalized values of the parameters presented in Figure 4-8, the drop in PCE of the devices are affected by both the drop in J_{sc} and the rise in R_s. although it must be noted that both are not necessarily independent phenomena. It is also clear that the trends aren't reversible meaning a permanent mechanical damage within the device has occurred.

Starting with J_{sc}, the dramatic drop of J_{sc} in both 5 cm and 2.7 cm bending radiuses meant that the mechanical degradation influenced either the efficiency of photon absorption of the active layer or the collection of the generated holes and electrons. Thus, the mechanical bending had either degraded the active layer, or effected the dissociation rate of the hole and electron i.e; influencing by that the active layer itself or the interfaces between the active layer and the HTL or ETL where even with a successful dissociation, the electron or hole might not pass to their respective collecting layer. Meaning, a delamination might have occurred between the active layer and either HTL or ETL.

As discussed, the dissociation rate depends on the interfaces between donor and acceptor within the active layer, therefore, any mechanical deformation within the active layer that could create some sort of fracture, would lead to a electron or hole trap would eventually lead to reduction to the charge carrier transformation. Now consequently, there will be a dramatic increase in R_s. However additionally, the mechanical bending could have affected the contact resistance between the interlayers or an increase in the sheet resistance of the ITO layer upon bending. Therefore, the next chapter will focus on investigating these aspects of the device to further understand the effect of bending on the device performance. This will be done by conduction a 4-point prob to the electrodes (Ag and ITO). Moving to V_{oc} and FF (Figure 4-8c and e), the stability of FF and V_{oc} compared to the other parameters, indicates that there are no ohmic losses within the device, this in return, validates the wiring system of the device throughout the test (See Chapter 3). Although as mentioned, the sheet resistance of the electrodes will be measured, the stability of FF and V_{oc} do give an initial indication that electrodes are not damaged mechanically.

In addition to that, all these changes are indicative of fact that the device is located either in the compression or tension region within bending stress and is not located on the neutral axis. This will be further confirmed via calculations and FEA simulation presented in Chapter 5. The investigation started with obtaining a cross sectional images via Transmission Electron Microscopy (TEM) show complete flexible device stacks before bending (Figure 4-9a) and after 100 bending cycles at bending radius of 2.7 cm (Figure 4-9b). In each case a distinct layer structure can be resolved showing all device components. Through collaboration with the group of Prof Thomas Anthopoulos (KAUST) efforts were made to study the evolution of interface integrity and any evolution of microstructure following mechanical testing, in this case utilising TEM. Unfortunately, issues associated with beam damage of the PET substrate meant that delamination and/or deformation could not be observed.

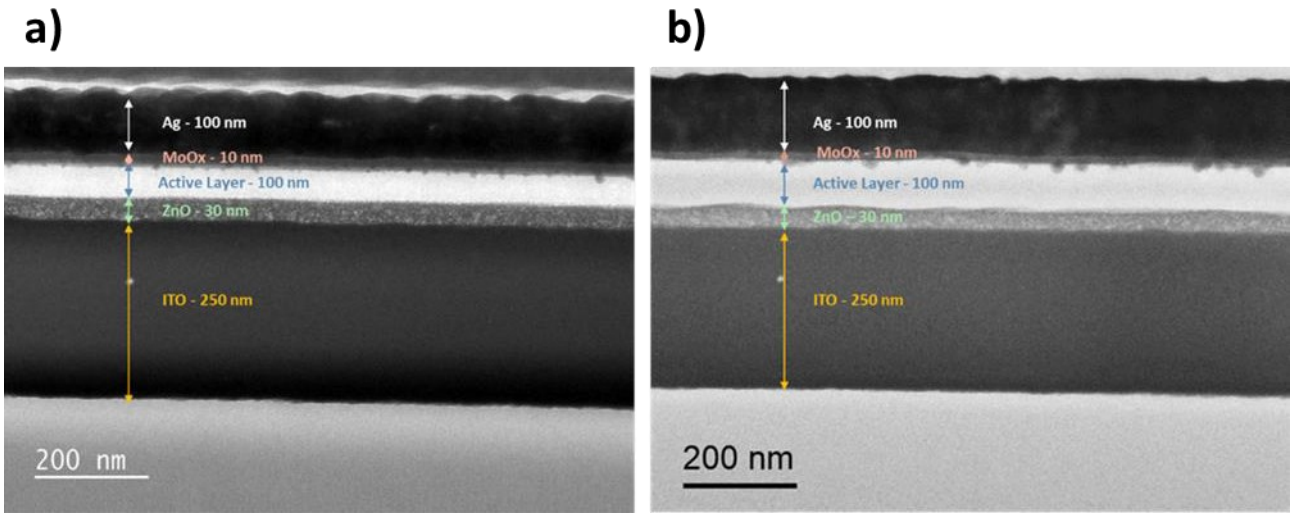

Figure 4- 9 Transmission Electron Microscopy (TEM) image of the flexible PET-based OPV structure, illustrating the thicknesses of each layer, a) a reference flexible OPV that did not undergo any mechanical testing, b) flexible OPV that underwent 100 bending cycles with bending radius of 2.7 cm

The lake of answers in literature as to the changes within the flexible device performance after and during mechanical deformation was the main drive of this work. In the next chapter, a further investigation of each layer of the device will be carried out to further understand the process of mechanical degradation.

4.4 Conclusion

It was shown that the optical properties of PET based OPV is compatible to the glass. PET based OPV devices were successfully fabricated under ambient conditions and device ambient stability was investigated. The device ambient stability test showed that within 20 hours the device is stable, allowing a window to mechanically test unencapsulated device under ambient condition without having an effect of environmental ambient degradation. The 3-point bending of the devices bending radiuses of 2.7 cm, 5 cm showed a dramatic decrease in the PCE, J_{sc} which is associated with an increase in R_s. It also showed that most of the mechanical damage occurred between 10 bending cycles and 50 bending cycles, after which most parameters remained constant expect for R_s. The stability of both FF and Voc indicated that the device's temperature did not increase during the test and that there aren't any ohmic loess within the device indicating that the electrodes (Ag and ITO) are intact and it validates the wiring system used. None the less, the overall trends of the device indicates that the device dose not lay within the neutral axis. TEM was utilized to obtain visual evidence of mechanical deformation within the device cross section, issues associated with beam damage of the PET substrate meant that delamination and/or deformation could not be observed. To further understand the effect of mechanical bending on the microstructure of the device, each individual layer within the device must be examined along with the interface.

Chapter 5

Understanding the influence of 3-point mechanical bending test on OPVs

5.1Introduction

In chapter 4, the evolution of performance parameters of flexible OPV under 3-point cyclic bending tests were studied. Here the origins of the observed behaviour *i.e.* the underlying reasons behind the mechanical deterioration and the effect of bending cycles and bending radiuses were investigated. The devices were examined, starting with the electrodes, the active layer, and the interfaces between the interlayers of the device. This was done by utilising a novel in-situ system that tracks changes in resistance within a device while bending. An in-situ bending of flexible OPV under illumination was also conducted to further understand the changes in performance parameters when the flexible OPV is under bending compared to when in flat conditions. The effect of encapsulation on the behaviour of the device before and after 3-point bending was also investigation along with the use of FE analysis,

5.2 Examining the PET substrate and ITO layer.

The first step of the characterisation was to consider the ITO layer, recall this has a thickness of 250 nm on around 0.21 mm PET. First the electrical properties were measured using a four-point probe, whereby the sheet resistance was measured using as-received (reference) ITO and using films that had undergone 100 bend cycles, of 10 cm, 5 cm and 2.7 cm, the results are summarised in Table 5-1.

Table 5- 1 shows the calculated sheet resistance of ITO after 100 bending cycles with three different bending radiuses 10 cm, 5 cm and 2.7 cm. The reference sample did not undergo any mechanical testing and was measured immediately after cleaning.

Bending radius	*Sheet resistance*
Reference	13.6 Ω/□
10 cm	13.6 Ω/□
5 cm	13.6 Ω/□
2.7 cm	13.6 Ω/□

From Table 5-1 it is clear that within the bending radiuses range investigated and the number of bending cycles used in this work, the sheet resistance of the ITO appears not to be affected. Lim *et al.* conducted a study to determine the flexibility of ITO on polysulfone (PES), PET and PEN substrates under cyclic bending test, their study concluded that the conductive stability of ITO electrode is significantly affected by Young's modulus of substrate [147]. They concluded that with lower values of Young's modulus, the more resistive a substrate is to plastic deformation when experiencing tension or compression. As such, PET has superiority when compared to other candidates of plastic sheets due to its low Young's modulus values (see Table 2-1 in Chapter 2). Whilst different substrates were not investigated in the present work the PET substrates underwent no visual deformation as discussed in Chapter 3, and the

consistency of the sheet resistance measurements confirm that the ITO underwent no degradation. Another study reported that when a 3-point bending test was performed on ITO/PET substrates it resulted in delamination and cracking of the ITO, where after 100 bending cycles with 2.5 mm bending radius, an increase of 50% of sheet resistivity of ITO was noticed [148]. In which the PET thickness was around 0.127 mm and the ITO thickness was around 200 nm. The study indicated that, such mechanical failure was attributed to the flexural strain that the samples has experienced of around 1% tensile strain [148]. In order to compare this to the work done in this thesis, the fractural strain must be calculated. Nonetheless, the maximum strain equation in Chapter 2 (see Equation 2-7) does not represent the actual flexural strain in case of a bilayer material such as PET/ITO substrates. However, before calculating the flexural strain, it is important to note if the strain calculated is a tensile or compression nature. Therefore, the location of the neutral axis must be calculated. The location of the neutral axis

in a bilayer system with different Young's modulus values can be calculated using equation 5-1 where (b) is the distance from the outer surface to the mechanical neutral axis.

$$b = (\frac{t_f+t_s}{2})\frac{(1+2\eta+x\eta^2)}{(1+\eta)(1+x\eta)} \qquad \text{Equation 5-1}$$

Where t_f and t_s are the thin film (ITO) and substrate thickness respectively and r_c is the bending radius, η is the thickness ratio between the film and the substrate and x is the Young's modulus ratio between the film and substrate respectively [149]. Thus, the terms are defined as follow:

$$t_f = 0.00025\,mm \therefore\ t_s = 0.21\,mm\ \therefore x = \frac{E_f}{E_s} = \frac{150}{2.7}\ \therefore\ \eta = \frac{t_f}{t_s} = \frac{0.00025}{0.21}$$

Thus, according to calculation the location of the neutral axis is located at 0.11 mm from the outer surface for the PET/ITO substrate used in this work. Meaning that the neutral axis is located around the centre of the PET layer. This means that the ITO layer is experiencing tensile strain giving the bending configuration used in this work (See Chapter 3, Section 3.4). Using Equation 5-2 the flexural strain sustained by the ITO layer in this work can be calculated where r_c is the bending radius.

ε

$$\varepsilon_{ITO} = \left(\frac{t_f + t_s}{2r_c}\right)\frac{(1+2\eta+x\eta^2)}{(1+\eta)(1+x\eta)}$$ Equation 5-2

The calculated values of the flexural strain were 3.89×10^{-3} %, 2.11×10^{-3} % and 1.10×10^{-3} % for bending radiuses of 2.7 cm, 5 cm and 10 cm respectively. These calculated values are smaller than the strain values reported in the study mentioned above. Many papers have been published to understand the electrical and mechanical reliability of ITO on PET substrates. Lim *et al.* preformed another study to indicate a critical bending radius, above which ITO layer conductivity is preserved. The paper concluded that for 150 nm thick ITO layer a bend radius of 6 mm is the lower limit at which bending could occur without impacting conductivity [150]. The results determined experimentally in the present work are thus consistent with the established literature and it can be concluded that under the mechanical bend testing carried out that the electrical properties of the ITO are preserved. Although Equation 5-1 can be further developed to locate the position of the neutral axis for multilayer systems OPV an OLED devices [150-152]. It requires a heavy mathematical modelling which is outside the scope of this work. In addition, for the OPVs fabricated for this work, the active materials are new and their material properties such as Poisson ratio and Young's modulus are not yet established. Therefore, the work reported herein will continue with the assumption based on multiple studies, that the neutral axis remains in the flexible substrate [153-158].

5.3 In-situ bending method of examining mechanical degradation of OPV's interlayer and their interfaces.

Following the analysis of the ITO layer and determination of the neutral axis position it is now possible to explore the additional layers that comprise the completed device. In addition to the organic active layer key properties of the hole- and electron-transport layer, MoOx and ZnO respectively, and the completed devices will be probed. To achieve this, we developed a novel three-point bending test that, in-parallel, allowed the *in-situ* measurement of change in resistance.

In general, for thin materials such as those within 100 nm thick and less, that are used in OPV device fabrication for example, mechanical techniques such as four-point bending test (sandwich beam test) and peeling test, provides information regarding adhesion properties between the interlayers as illustrated in Chapter 2. In which a measurement of fracture resistance can be obtained in the form of adhesion energy or peeling strength respectively [159]. Although It has been suggested in literature that devices with adhesion energy lower than 5 J m^{-2} would lack mechanical resilience during manufacturing and operation [160, 161]. There is a lack of information as to how any of these quantitative values translate in a 3-point mechanical bending test, in terms of bending radiuses and number of cycles along with the device's performance parameters, that's in addition to the lack of these specific measurements for OPV devices. Thus, comes the novelty and benefits of the in-situ bending while measuring change in resistance. At which user will be able to track the changes

occurring within the flexible OPV devices' interlayers in form of changes in resistance while obtaining information regarding limits to bending radius and number of bending cycles. Thus, here ZnO layer, MoOx layer and the full device will be examined utilising the in-situ bending system.

Investigating ZnO layer

Prior to conducting the in-situ test, and to further understand the effects seen in Chapter 4, PET/ITO/ZnO sandwich structure, underwent 100 bending cycles with the 3 bending radiuses in interest (10 cm, 5 cm and 2.7 cm). As no visual degradation *i.e.* macroscopic cracking could be observed by eye, hence AFM imaging was carried out to probe the ZnO surface and evaluate surface homogeneity and roughness. Figure 5-1 shows tapping mode AFM images of ZnO surfaces. It is clear that the changes in RMS roughness of the ZnO only increases slightly with reducing the bending radiuses at 100 bending cycles. This was good indication that the ZnO layer remained intact, and AFM could not detect any cracks present.

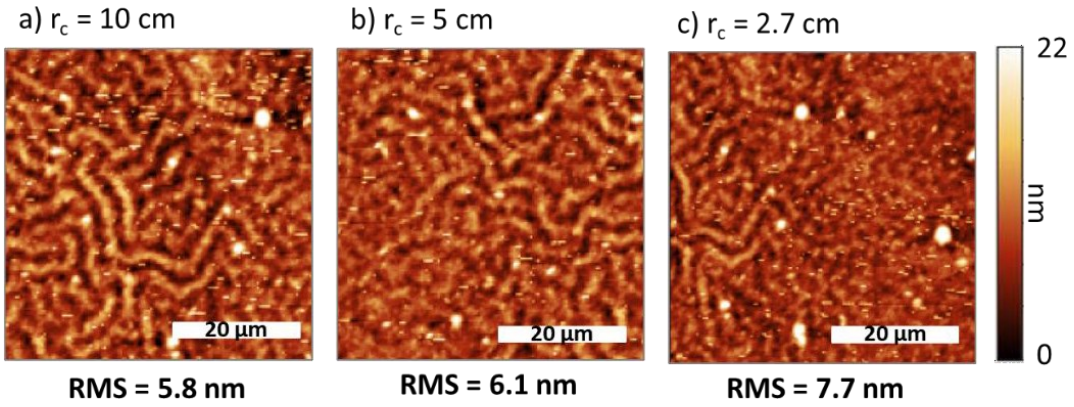

Figure 5- 1 Tapping mode AFM height images of PET/ITO/ZnO bent for 100 cycles at speed of 30 mm s^{-1} to mimic the experiment reported in chapter 4. a)PET/ITO/ZnO bent bending radius of 10 cm. b) PET/ITO/ZnO bent bending radius of 10 cm. c) PET/ITO/ZnO bent bending radius of 10 cm. The RMS roughness values are an average of 5 different areas within the sample

Thus, it is important to examine the changes between the interfaces of ZnO layer with ITO and Ag layers while bending. To do that, a 30 nm ZnO layer was spin coated onto PET/ITO substrates and a 100 nm film of Ag was then thermally evaporated directly on top the ZnO layer. A slow (2 mm s^{-1}) 5-cycles 3-point bending test was performed for bending radius of 2.7 cm, 5 cm and 10 cm whilst recording the resistance of the sandwich device. Assuming that the neutral axis remains at the PET substrate, the following bending mechanism is predicted to have occurred as shown in Figure 5-2, where the ITO, ZnO and Ag are under tensile strain.

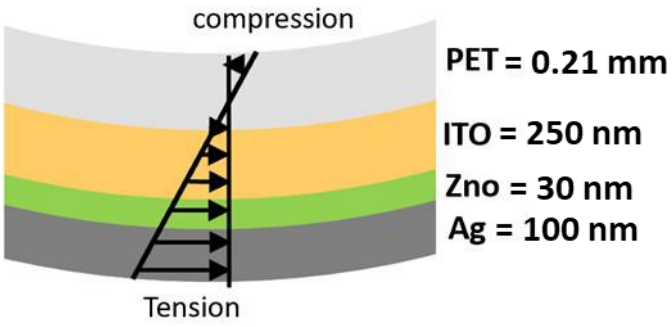

Figure 5- 2 A schematic representation of bending mechanism of the sandwich device with the loading pin being in contact with PET back surface. The point where the sample does not experience compression nor tension is the assumed position of neutral axis.

The resistance of the sandwich device during bending was plotted against the distance moved by the loading pin for 5 cycles. Results for bending radius of 2.7 cm, 5 cm and 10 cm are presented in Figure 5-3. Before analysing the results in Figure 5-3 it should be noted that the initial resistance values differ between samples. This is attributed to the wires connectivity issues to the external circuit, discussed in Chapter 3. Whilst it would have been better to have comparable initial values it is in-fact the overall change in resistance and the trend of changes during bending that are of interest here. It is also important to note that owing to the rate and number of data acquisition and facilities access as this experiment was done at Queen Mary University, we could not preform beyond 5 cycles for the in-situ test.

Looking at Figure 5-3, and considering first the films that underwent a 10 cm bending radius there is an observed increase in resistance during bending which is rather small, over the 5 cycles the resistance increases by around 1 Ω. Interestingly there is a greater increase, around 6 Ω after the first bending cycle but this appears to be reversible and overall, it can be concluded that at 10 cm bending radius the sandwich structure does not undergo significant, irreversible change in resistance. Thus, it is a good indication that at 10 cm bending radius no damages to the interface in observed nor to the ZnO layer itself. Reducing the bending radius to 5 cm results in more significant increases in resistance. During the 5 cycles the resistance increases by around 85 Ω, however, reversibility in resistance is also noticed. To have a clear

visualisation, each cycle was plotted individually and is presented in Figure C-1 in Appendix C. At the 2.7 cm bending radius, an overall increase of resistance of around 75 Ω was measured, interestingly here the data are resolved and the changes in resistance during each loading cycle can be clearly observed. The resistance increases on loading and unloading however the magnitude of the change reduces with bending cycle.

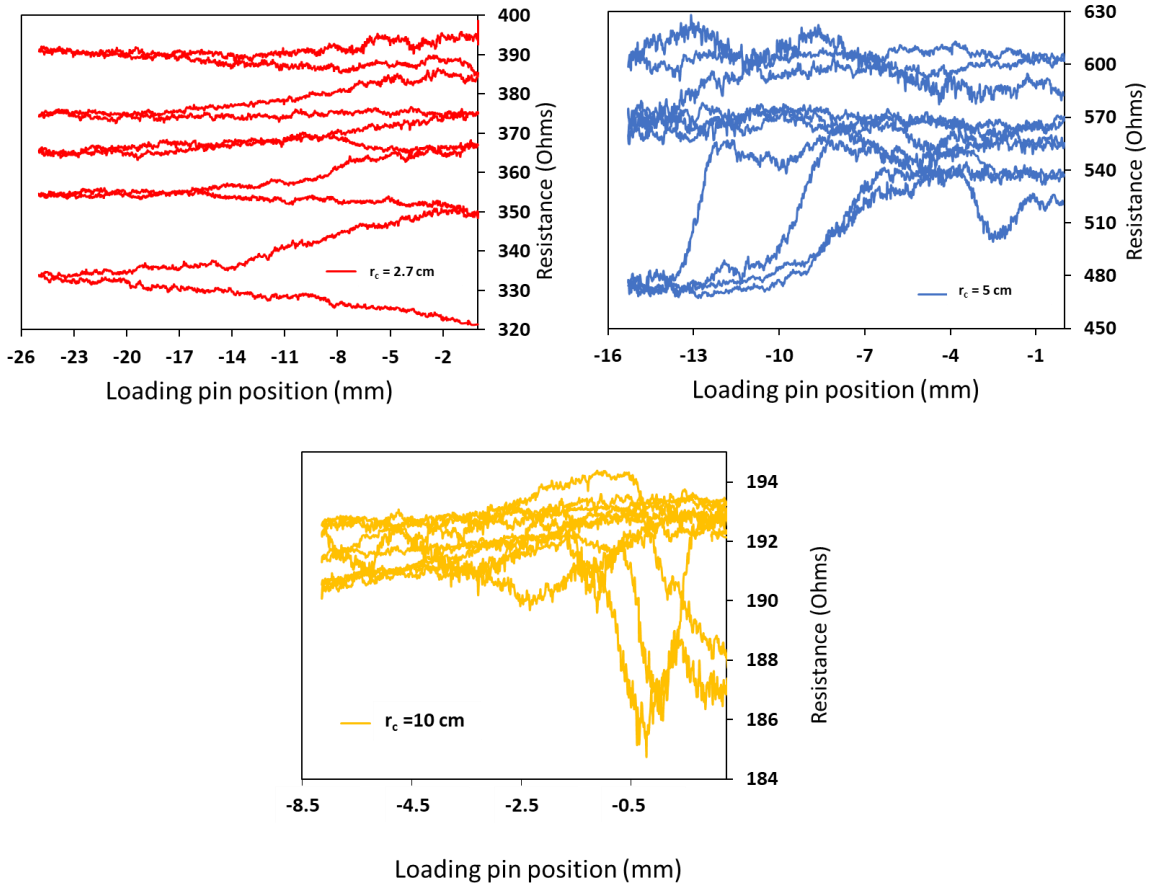

Figure 5- 3 Shows changes in the resistance of the sandwich device during bending. The negative signs in the loading pin position indicated the downward movement. When the loading pin is at 0 mm, the sample is flat. Loading pin position of 7.9 mm, 15.3 mm and 25 mm correspond the bending radiuses of 10 cm, 5 cm and 2.7 cm respectively.

As no damages to the ZnO layer was detected using AFM, it can be concluded that the changes in resistance experienced with both 2.7 cm and 5 cm bending radius are attributed to a defect within the interface between ZnO with either ITO or Ag layer such as delamination. Although no data reported in literature as to the effect of bending in general on the interface of ZnO and ITO, it has been reported that the peeling strength of ZnO layer on top of ITO layer can be increased with a short O_2-plasma or UV-ozone treatment [162, 163]. A paper has suggested that exposing ZnO layer to UV-ozone treatment for 2.5 minutes lead to an increasing in the peeling strength from 0.5 N cm^{-1} to 7 N cm^{-1} using T-peel test[115]. Literature suggests that this improvements in adhesion between ITO and ZnO after the exposure of either O_2-plasma or UV-ozone is associated with the removal of surface alkyl groups [164-167]. These alkyl salts

are present in commercial ZnO dispersions and are often result in poor interaction with oxide surfaces, including ITO, leading to poor adhesion.

As discussed in Chapter 3, the ZnO layer fabricated for this work, underwent a 5-minute UV-ozone treatment. This was done to enhance the surface properties to improve wettability of the ZnO before depositing the active layer. This agrees with the literature where it has been reported that UV-ozone exposure of ZnO layer leads to hydrophilic surface with nearly zero degree contact angle for water [168]. Figure 5-4 shows the effect of UV-ozone treatment on ZnO layer for 5 minutes on the contact angle measurement with the active layer solution made for this work. The contact angle measurements were conducted by Matyas Daboczi.

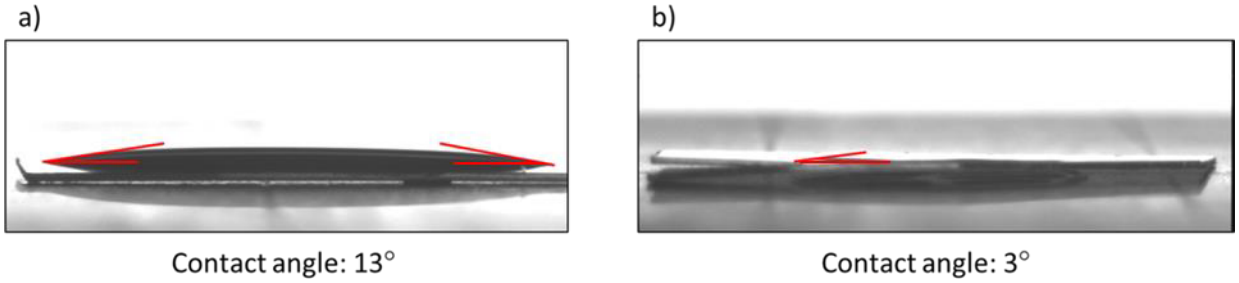

Figure 5- 4 shows the effect of UV-ozone treatment on ZnO layer for 5 minutes with the droplet being the active layer solution (PCE12:ITIC). a) Before UV-Ozone treatment and b) after the UV-ozone treatment. The UV-Ozone treatment resulted in a more hydrophilic effect on the ZnO layer.

To further examine the changes of bending behaviour on ZnO layer with ITO interface, the same experiment was repeated twice but, without the 5 minutes UV-ozone treatment to the ZnO layer. Figure 5-5, illustrates the *in-situ* experiment with 5 cm bending radius without UV-ozone treatment to the ZnO layer. In which it is clear that when literature reported low peeling strength for ITO/ZnO interface, the in-situ system introduced in this work, recorded resistance overload within the second cycle of bending radius of 5 cm at which delamination occurred. Whereas, after the UV-ozone treatment (going back to Figure 5-3), at 5 cm bending radius, the change in resistance is reversable at 5 cm bending radius, and at 2.7 cm bending radius, the magnitude of change in resistance reduces with bending cycles. Thus it can be concluded that a within the devices fabricated in this work, upon bending with 2.7 cm and 5

cm bending radius, the interface with ZnO/ITO did not cause the mechanical degradation of the devices observed in Chapter 4.

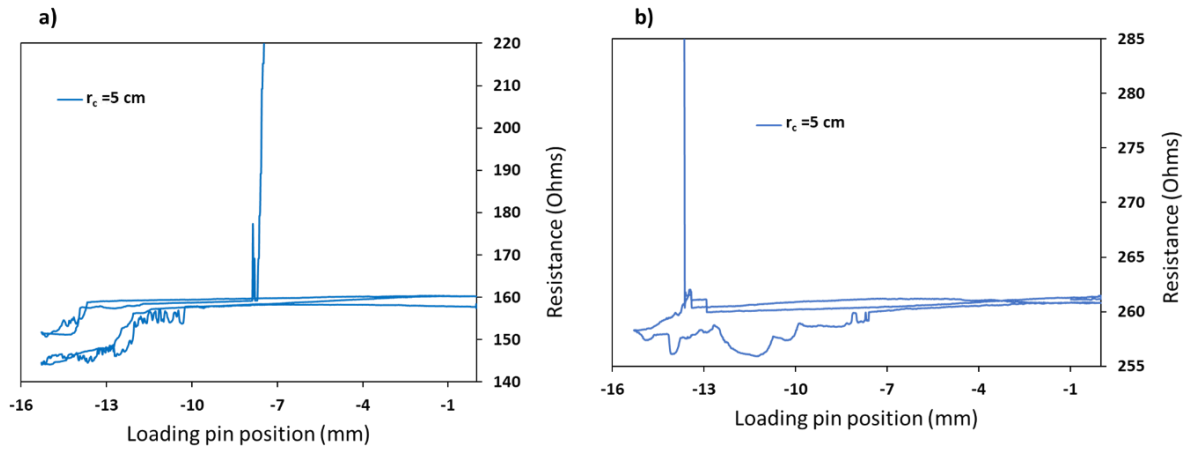

Figure 5- 5 Shows changes in the resistance of two sandwich devices (a and b) during bending with bending radius of 5 cm (PET/ITO/ZnO/Ag) without exposing the ZnO layer to UV-ozone treatment. The negative signs in the loading pin position indicated the downward movement. When the loading pin is at 0 mm, the sample is at a flat position.

Additionally, these results prove the reliability of the novel in-situ bending system introduced in this work. In which it became clear that users can track the maximum bending cycles an interface can withstand for a given bending radius, and it aligns with reported peeling strength values reported with literature. It must be noted that the resistance cut-off values in the y-axis in Figure 5-5, was not done manually. As these were the last recorded resistance value by the Keithley digital multi-meter before the overload was recorded. In this case the overload resistance value was 10 kΩ.

Although the ZnO/Ag interface won't be present in the completed devices reported here, it is important to rule out the possibility that delamination at this interface is influencing the results obtained during in-situ bend testing presented above. According to literature, It has been reported that at around 3 GPa of tensile stress, delamination occurs between ZnO/Ag interface, which was obtained using nano-indentation technique [169-171]. Although the finite element (FE) analysis shown later in this chapter will only simulate the stress distribution experienced by the substrate during bending, the simulations will indicate that for the mechanical bending done in this work, the maximum stress distribution through the

sample is below GPa range. Thus, it is believed that the ZnO/Ag interface is enact within this experiment. Therefore, by on the in-situ bending system, and from the AFM analysis carried out for ZnO layer, it can be concluded that the overload of resistance seen in Figure 5-5 is attributed to the interface between ZnO/ITO, which was enhanced upon UV-ozone treatment of 5 minutes as indicated in Figure 5-4. Thus, it is believed that mechanical degradation the OPV experienced and reported in Chapter 4 where not caused by ZnO layer nor its interfaces with Ag and ITO.

Investigating MoOx layer

Similarly to the case of ZnO, PET/ITO/MoOx sandwich structure, under went a 3-point bending test of 100 bending cycles with the three bending radiuses 10 cm, 5 cm, and 2.7 cm in order to investigate its change in morphology and surface quality after bending. Figure 5-6 shows the film morphologies observed for each bend condition for 100 bending cycles along with the RMS roughness values.

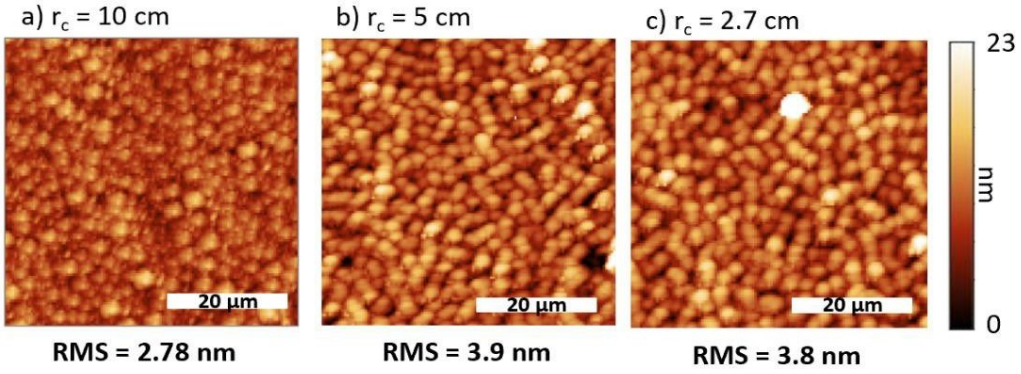

Figure 5- 6 Tapping mode AFM images of PET/ITO/MoOx bent for 100 cycles at speed of 30 mm s^{-1} to mimic the experiment reported in Chapter 4. a)PET/ITO/MoOx bent bending radius of 10 cm. b) PET/ITO/MoOx bent bending radius of 10 cm. c) PET/ITO/MoOx bent bending radius of 10 cm. The RMS roughness values are an average of 5 different areas within the sample

It is clear from the AFM images that no significant observable changes in surface morphology or roughness occurs during 100 bend cycles for any of the bend radiuses investigated.

Similarly, no defects *i.e.* cracks were observed. From there, the in-situ bending test was conducted to further understand the effect of bending on the interface of MoOx with ITO and Ag. In which a sandwich device of PET/ITO/MoOx/Ag was fabricated, Figure 5-7 shows a schematic representation of the bending mechanism of the sandwich device. Figure 5-8, shows the change in resistance of the device during bending.

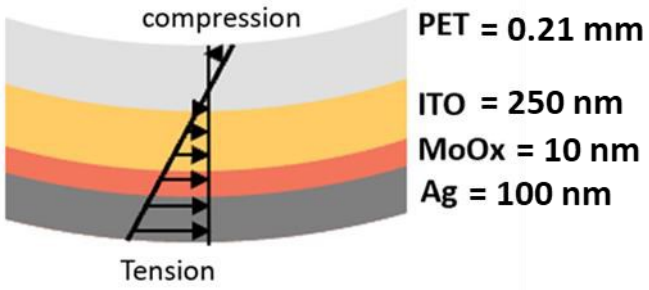

Figure 5- 7 A schematic representation of bending mechanism of the sandwich device (PET/ITO/MoOx/Ag) with the loading pin being in contact on the PET side. The point where the sample does not experience compression nor tension is the assumed position of the neutral axis.

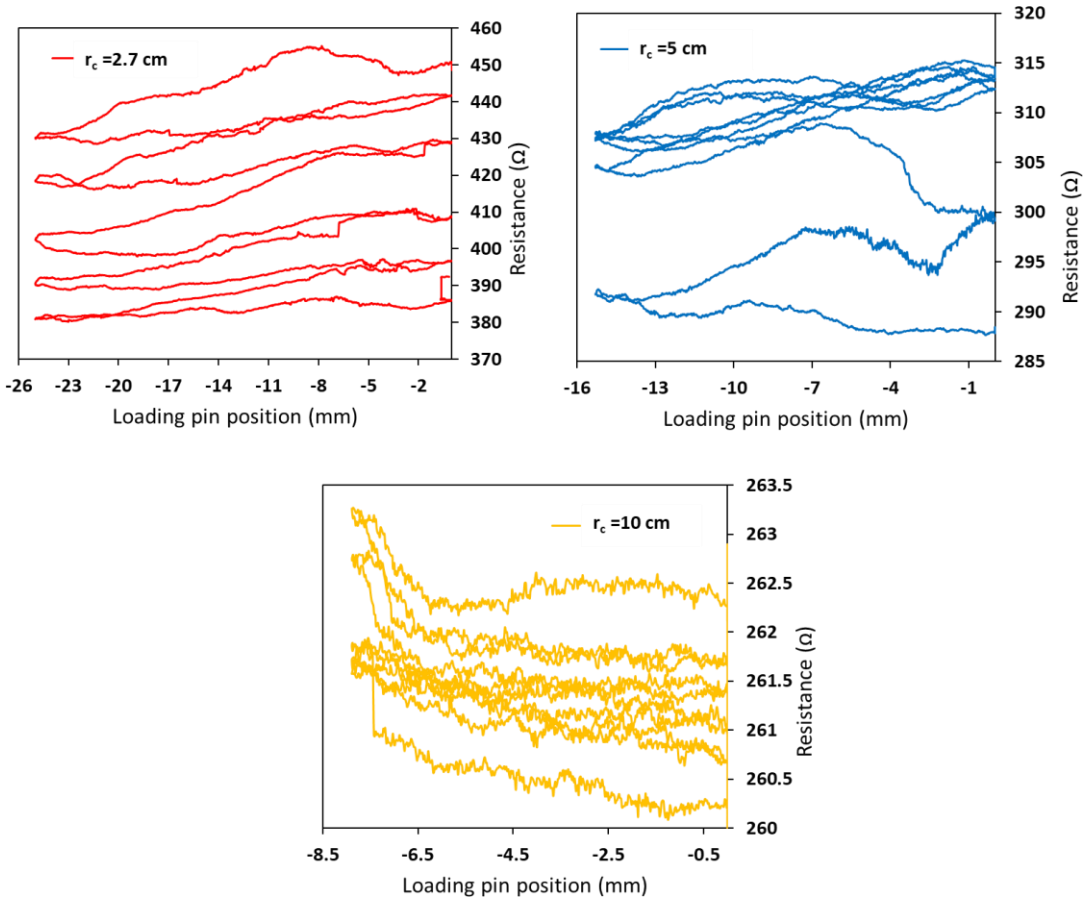

Figure 5- 8 The change in the resistance of the sandwich device (PET/ITO/MoOx/Ag) during bending. The negative signs in the loading pin position indicated the downward movement. When the loading pin is at 0 mm, the sample is flat. Loading pin position of 7.9 mm, 15.3 mm and 25 mm correspond the bending radiuses of 10 cm, 5 cm and 2.7 cm respectively.

Considering first the data for the 10 cm bend radius. It appears there is a very small ~ 2 Ω increase of resistance during loading that is reversible when the load is removed. At bending radius of 5 cm, the overall increase in resistance is around 26 Ω, however, it is clear that beyond 2 cycles, there is no changes in resistance is observed. This could indicate that no mechanical degradation is being experienced by the sandwich device during bending with bending radius of 5 cm. When moving to the 2.7 cm bending radius, the overall recorded increase in resistance with bending is around 65 Ω, and unlike the case of 5 cm bending radius there is no stabilisation observed in this bend regime. Thus, further investigation is required, to further understand the behaviour of MoOx under bending. However, as mentioned before, owing to the rate of data acquisition and facilities access, we could not preform beyond 5 cycles for the in-situ test.

Within a full device structure, the interface of interest in this case is MoOx/Ag layer and MoOx/ITIC:PBDP-T. Although multiple publications have studied the interface adhesion interface of devices with MoOx layer as a HTL [146, 172-178]. None have reported a weak interface between MoOx/Ag nor an interface adhesion energy value in any of the tests reported. Nonetheless, there remains two interfaces of interest which are ZnO/ITIC:PBDP-T interface and ITIC:PBDP-T/MoOx interface. Thus, the same analysis of in-situ bending while measuring the resistance was tested on the full device. This would help look at the entire device system while also further investigate the interfaces in interest.

Investigating the entire OPV structure

In here, the complete OPV device underwent the in-situ bending system. Figure 5-9 shows a schematic representation of the bending mechanism of the sandwich device. Figure 5-10, shows the change in resistance of the device during bending.

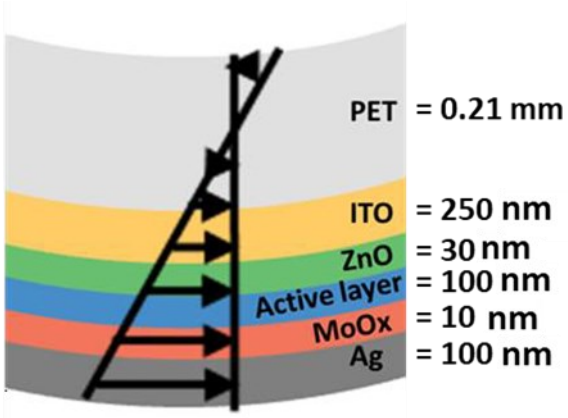

Figure 5- 9 A schematic representation of bending mechanism of the OPV used in this work with the loading pin being in contact with PET layer. The point where there the sample does not experience compression nor tension is the assumed position of the neutral axis.

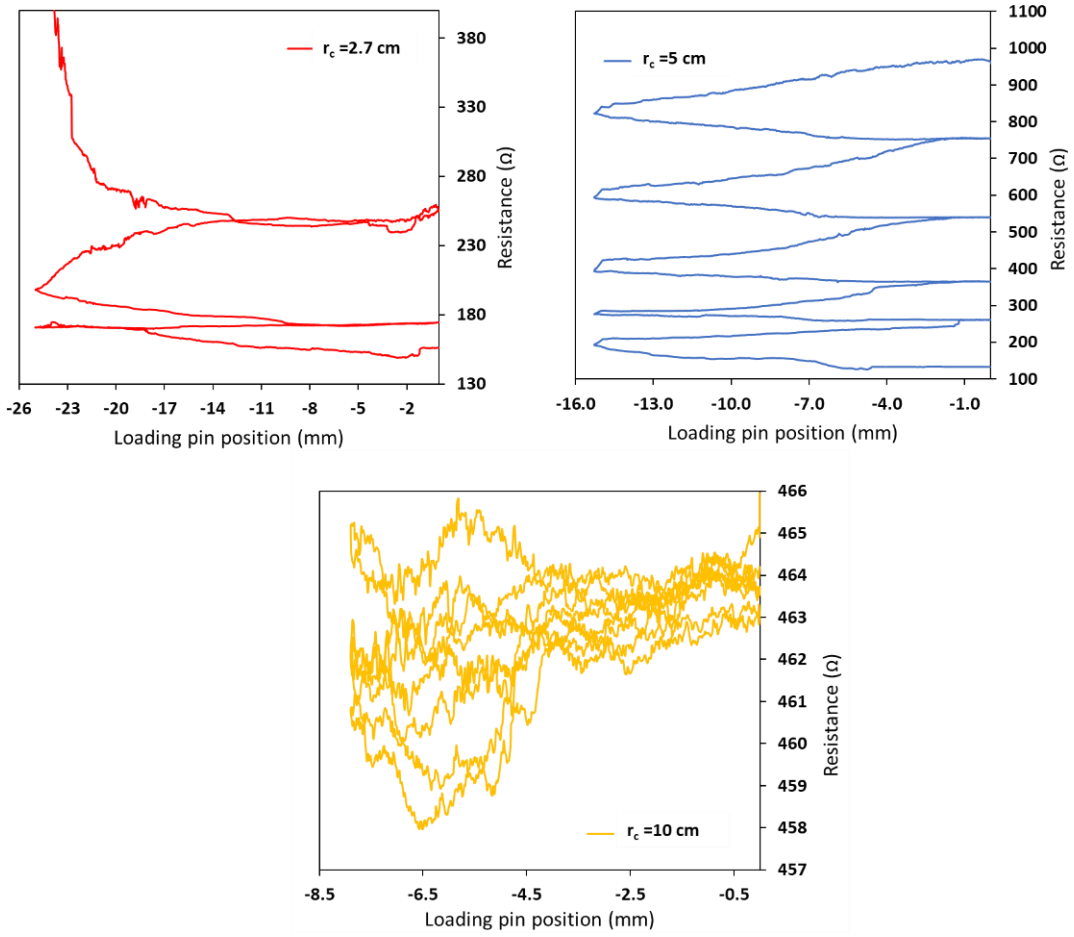

Figure 5- 10 The change in device resistance (PET/ITO/ZnO/ITIC:PBDP-T/MoOx/Ag) during bending. The negative signs in the loading pin position indicated the downward movement. When the loading pin is at 0 mm, the sample is flat. Loading pin position of 7.9 mm, 15.3 mm and 25 mm correspond the bending radiuses of 10 cm, 5 cm and 2.7 cm respectively.

From the data collected in Figure 5-10, at 10 cm bending radius the overall change in resistance is around 2 Ω. Such small change in resistance aligns with changed observed in ZnO and MoOx sandwich devices for 10 cm bending radius. Moving to 5 cm bending radius, an overall increase in resistance of around 880 Ω is recorded, this increase is consistent with each bending cycle and non-reversable. At 2.7 cm bending radius, the first cycle led to a jump in resistance by around 30 Ω, and by 70 Ω after the second cycle. However, by the third cycle, the device resistance overloaded. In order to ensure that such overload, is not due to wiring

issues or wire contact damage, the sample was brought back to flat conditions and the same pixel was measured again; the overload occurred at around 20 mm within the first half of the first cycle (See Figure 5-11a). Upon testing a new sample, in order ensure repeatability of the data and thus confirm the findings, it was found that resistance overload occurred at the start of the second half of the first cycle (see Figure 5-11b). Although resistance overload occurred earlier, it is clear that it is a feature related to radius of 2.7 cm. From Figure 5-11a, it can be concluded that when the sample is back at flat conditions, the resistance overload is reversible until bending starts again for the same pixel. This could be an indication of delamination feature, where upon bending the sample, the delaminated area is back in contact, and once bending continues, the separation between the two interfaces occurs again.

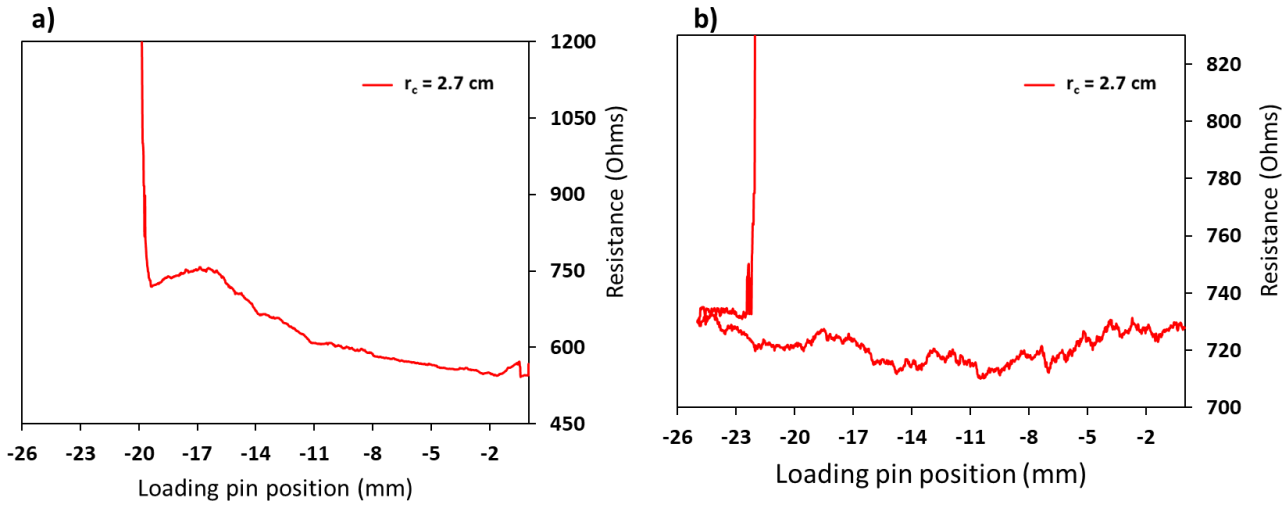

Figure 5- 11 The change in the resistance of the device (PET/ITO/ZnO/Active layer/MoOx/Ag) during bending with bending radius of 2.7 cm. a) repeated analysis of the same sample tested at Figure 5-10 for bending raids of 2.7 cm, shows reversibility of the resistance overload when the sample is brought back to flat condition. b) A new sample was tested at bending radius of 2.7 cm.

By measuring the whole device via the in-situ system, two new interfaces have been introduced, ZnO/ITIC:PBDP-T and MoOx/ITIC:PBDP-T. According to literature, the peeling strength of ZnO/P3HT:PCBM has been reported to be around 7 N cm^{-1} . Whereas, the peeling strength of MoOx/P3HT:PCBM is around 0.9 N cm^{-1} which were determined via T-peel test [115]. Additionally, by comparing the in-situ results of MoOx sandwich structure (Figure 5-8)

and the full device (Figure 5-10) at 5 cm bending radius specifically, we can conclude that the increase in resistance is not caused by a weak Ag/MoOx interface. And thus, by referring to of peeling strength in literature, it can be assumed that the resistance overload recorded at 2.7 cm bending radius, and the continues increase in resistance at 5 cm bending radius, is arising from the weak interface between the active layer and MoOx which translate into delamination at 2.7 cm bending radius. Ideally, an adhesion energy test or peeling strength should be associated with the in-situ bending system presented in this work to further confirm these week interfaces.

To further confirm this, a sample of flexible solar cell was laminated and then the top layer of the laminate was removed to mimic the performance of a peeling test manually, Figure 5-12 show clearly the layers that were removed with the top layer of the laminate.

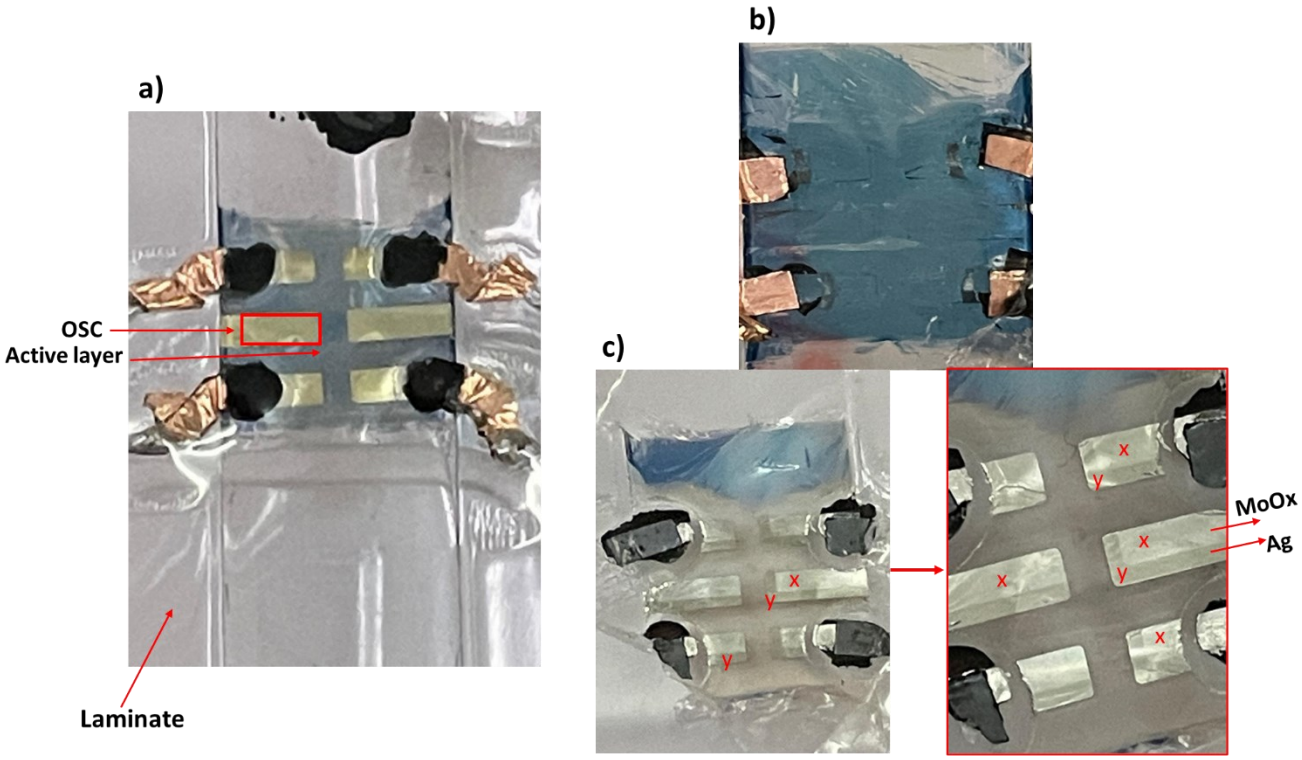

Figure 5- 12 a) The full device structure is shown after encapsulation. In b) and c) are the results of removing the top layer of the laminate i.e.; performing a manual peeling test. b) (bottom layer) shows what remained in the lower part of the laminate after peeling, showing a full coverage of the active layer. c) (top layer) shows the layers that were peeled with the top layer of the laminate; it clearly shows the complete removal of the silver electrode; it is also clear that there is an additional layer on top which is lighter in colour than the silver electrode which is believed to be the MoOx layer (marked by x) where the layer on top Silver is marked with y.

The manual peeling test that was performed on the encapsulated device (Figure 5-12a) shows clearly that after peeling the top layer of the laminate, the entire silver electrode was removed (see Figure 5-12c) however, it is also clear that within the silver electrode there is an additional layer removed which is lighter in color (marked in x) on top of the silver layer. This layer is believed to be the MoOx layer. Further confirming that the week interface is between MoO and the active layer. This is supported by the fact that the active layer seem intact and not damaged after the peeling test (see Figure 5-12b). For future work, it is recommended to utilize EDX to further confirm the composition of the top part of the laminate.

As indicated in Figure 5-13, Optical microscope was again utilized, to further visualise the effect of 100 bending cycle on the active layer with the three bending radiuses of 2.7 cm, 5 cm and 10 cm and thus, relating it to the results obtained in chapter 4.

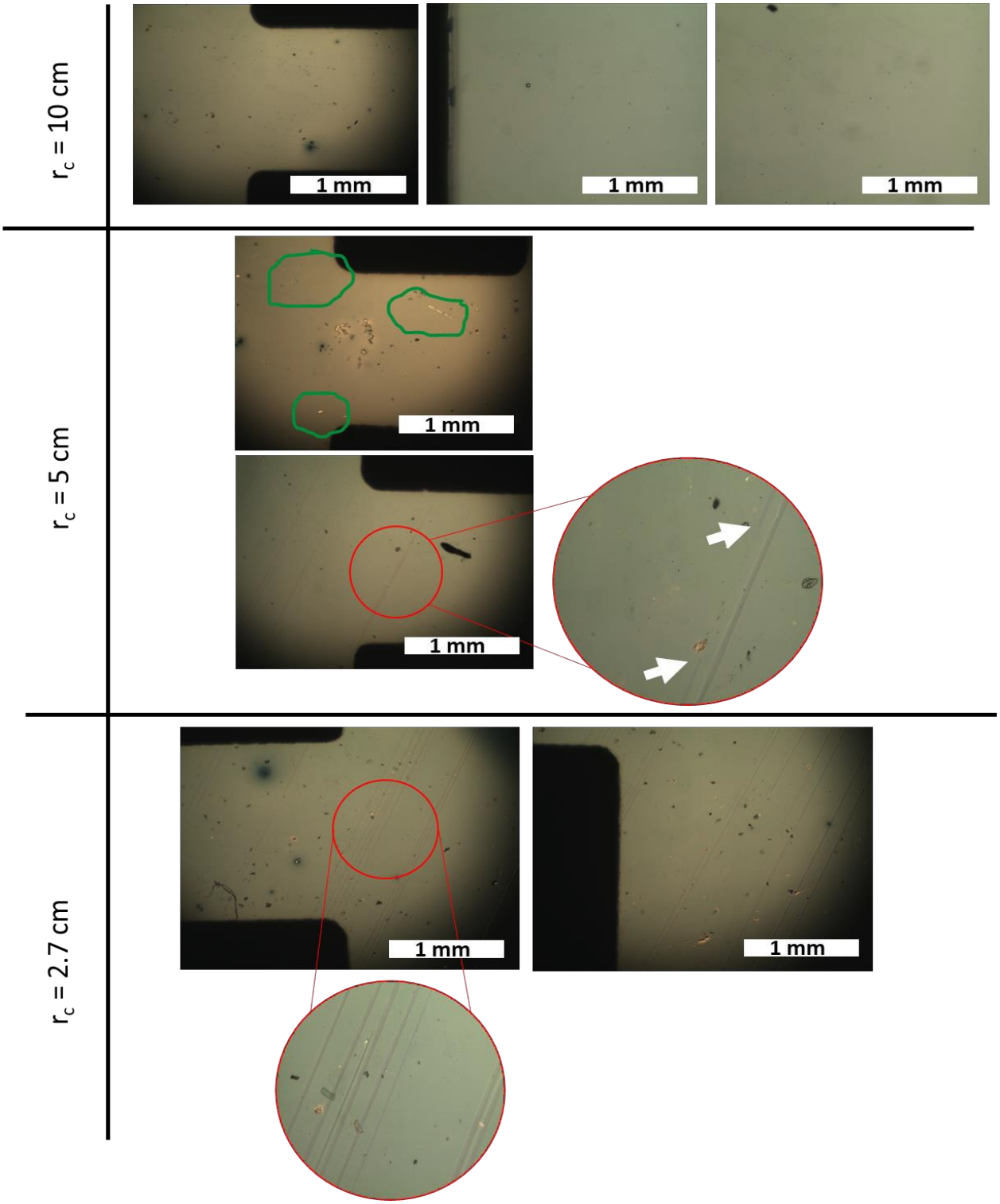

Figure 5- 13 Optical microscopic images of the active layer (ITIC:PBDP-T) after 100 bending cycles at the speed of 30 mm s^{-1} with three different bending radiuses of 10 cm, 5 cm and 2.7 cm. The square images were taken with 2.5x magnification, the magnified images in the circles were taken with 100x magnification. The green marks highlight the small scratches while the white arrow highlights the initiation of the new striation marks.

Although no visual damage to the active layer was observed after the in-situ experiments, it was important to examine the active layer after 100 bending cycles, to further understand the effect of bending on the active layer and on the overall performance of the device (See Figure 4-8). From Figure 5-13, it was clear that the bending radius had a clear effect on the active layer quality. At 10 cm bending radius, the active layer seems intact, and no damages are observed. At 5 cm bending radius, small scratches are observed (marked in green) which is believed to be due to handling the sample as they are not seen in any other samples. In addition to that, and minor striation are observed. The white arrows show what could be a start of these striations. At 2.7 cm bending radius, the striation appears to increase and are segregated. It is believed, that beyond 100 bending cycles or at a lower bending radius, these striations could lead a rupture and thus, damaging the active layer more severely.

Literature suggests that when blending a small molecule (SM) based acceptor such as ITIC, with polymer donor to form a BHJ, the small molecules acceptors are likely to act as anti-plasticizer that embrittles the BHJ blend [179-182]. A property that is undesired in flexible devices. At which SM-based acceptors tend to segregate within the BHJ and do not form connected ties and bridges with the polymer donor allowing for weak interaction leading to lower adhesion energy between donor/acceptor and thus, resulting in a brittle active layer. Although the mechanical properties behaviour of the BHJ blend used in this work is not reported in literature nor their behaviour during bending tests, the ITIC adhesion energy with PTB7-Th[f] is reported to be around 1.9 J m^{-2} [183]. When comparing SM-based acceptor with polymer acceptor for flexible OPV BHJ blends, it has been reported that a threshold of critical molecular weight of the polymer acceptor is required to ensure a robust mechanical behaviour, this critical molecular weight ranges between 45 and 104 kg mol^{-1} , above which significant enhancement in the adhesion energy is reported [104, 183, 184]. This is because, polymers with molecular weight higher than the critical value (45 and 104 kg mol^{-1}), introduce tie molecules and a network of entanglement chain between the polymer donor and acceptor. Thus, it would require a high strain energy to fracture the BHJ, making the active layer more ductile [183-185].

[f] Poly([2,6'-4,8-di(5-ethylhexylthienyl)benzo[1,2-b;3,3-b]dithiophene]{3-fluoro-2[(2-ethylhexyl)carbonyl]thieno[3,4-b]thiophenediyl}),

Thus, one can hypothesis, the mechanical behavior of SM-based acceptor within a BHJ could explain the striations appearing at 5 cm and 2.7 cm bending radiuses, where they could indicate a crack/rupture initiation spot. However, it is clear that the directions of the of the striation are not within the bending axis (x-axis), thus it is clear that what initiated the striation could have been a pressure point either due to temperature variation during the fabrication process or mechanical treatment (see Chapter 2) while handling the sample or wiring it. Thus, although the bending radius had a clear effect of these striations, it is important to note the point of origin of these marks.

From this work it can be concluded that the effect of 3-point bending test on the OPV fabricated in this work (features observed in Figure 4-8 in Chapter 4), are believed to be attributed to two possibilities: the weak MoOx/ITIC:PBDP-T interface resulting into delamination, which resulted in dramatic increase in R_s with increasing bending cycles and reducing bending radiuses. This became clear from the in-situ bending system once the full device was examined, and an overload of resistance occurred at 2.7 cm bending radius and a continuous increase in resistance with higher magnitude per cycle at 5 cm bending radius. In addition to the manual peeling test which clearly show a layer on top of the silver on the top part of the laminate and the fact that the active layer remained intact. The second possibility is damages to the active layer itself. Where, At 100 bending cycles, via the use optical microscope, striations were observed at 5 cm bending radius which became more prominent and segregated at 2.7 cm bending radius. In device performance parameters, it is believed that these striations could cause drop in J_{sc} values with bending cycles and lower bending radiuses. At which such morphology/feature could affect exciton separation efficiency.

The advantages of the novel in-situ bending system introduced in this work, allow for better understanding as to what happens to the device upon bending in terms of its optoelectrical properties. Although the system does not produce a definite quantitative result, such as peeling strength or adhesion energy. It does provide information related to the evolution of the interlayer and interfaces upon bending. Meaning, when relaying on 3-point bending test to quantify the degree of flexibility of a device, information such as peeling strength or adhesion energy does not provide data as to the limits of bending cycles and bending radiuses.

5.4 in-situ bending under illumination

Once a clear understanding has been developed around the effect of 3-point bending test on the OPV performance parameters, we wanted to understand the behaviour of the OPV when it is under bending, compared to when it is flat under illumination. It is worth mentioning that an attempt of recording the OPV J-V performance under compression during illumination on flexible glass substrate have been reported once in literature. However, the quality of the OPV devices did not allow for appropriate conclusion (more information can be taken from [186]).

Nonetheless, within work of this thesis, to conduct a 3-point bending experiment under illumination, it meant that the transparent side of the PET must be directly under the solar simulator, meaning that the loading pin had to be removed. Therefore, a replacement to the loading pin set up had to be found. Thus, a hydraulic robotic arm was assembled (acquired from CONSTRUCT & CREATE Ltd) to function as the loading pin, while the device was lightly held by clamps to allow for bending (see Figure 5-14). More information regarding the hydraulic robotic arm range of motion and design can be obtained from Appendix D.

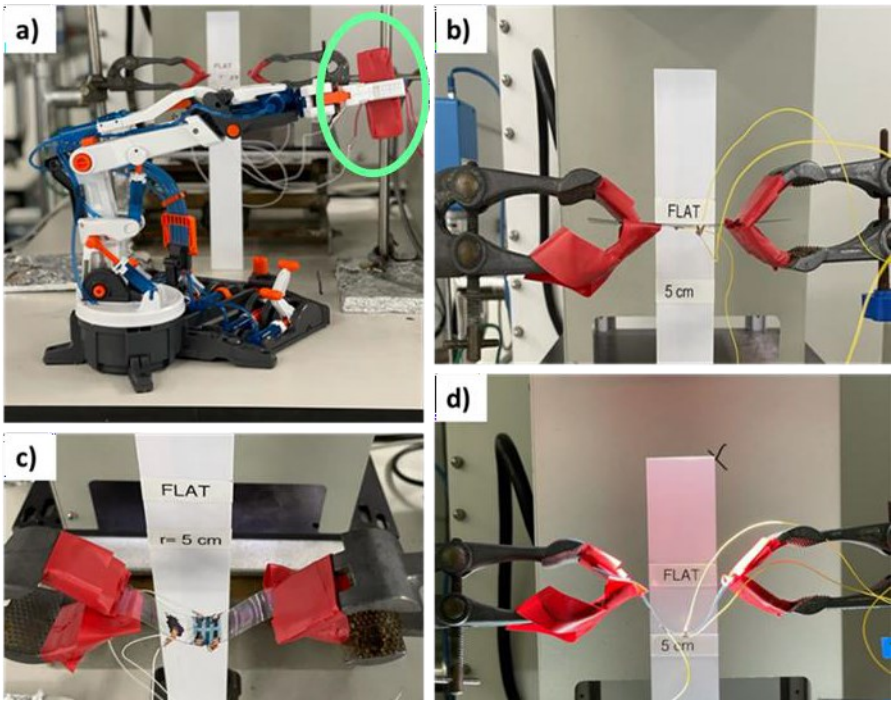

Figure 5- 14 Show the in-situ set up of 3 point bending system for flexible OPV to further understand the difference in device behaviour in both bending and flat conditions. a) shows the hydraulic robotic arm, holding a red block (marked with green) that functioned as the loading pin within a 3-point bending test. b) show the red clamps that acted as the support pins within the 3-point bending test and allowed the device to remain flat. In here the clamps were not tightened to not introduce any stress on the device or any movement. c) top view of the device under bending after removing the loading pin and slightly tightening the greps to hold the device under bending. d) device under illumination while bent.

Due to the nature of the set up, upon testing for 2.7 cm bending radius, the flexible OPV would snap-off of the red clamps that were holding the device. Thus, to ensure stability of device within the set up during measurements, the test here focused on bending radius 5 cm. The experiment followed the following steps: 1) First step was wiring the flexible OPV, using the same method described in Chapter 3. 2) The device was held by the clamps, being in flat conditions and the J-V curve was recorded under illumination (Figure 5-14b). 3) The hydraulic arm with the red block (loading pin), was brought in contact at top of the OPV device (under

the solar simulator), bending the OPV with bending radius of 5 cm, thus moved downwards a distance close to 15.3 mm which was confirmed at each bending stage with digital calliper. (Keeping in mind errors associated with measuring in a delict system) 4) The robotic arm would then be removed, and the bent device would be held in place simply by tightening the red clamps (see Figure 5-14 c and d). A J-V curve would then be recorded while the device is under bending. The stress introduced by slightly tightening the clamps does not affect the device as they it is localised to the side of the substrate. 5) The hydraulic arm would then go back in contact with the device, the clamps will be loosened, and with the help of the hydraulic robotic arm and loading pin, the device would unload and taken back to flat position. Figure 5-15 show the normalised values of the device performance parameters in flat and bent conditions. J-V curves along with normalised values of R_{sh} can be found in Appendix E.

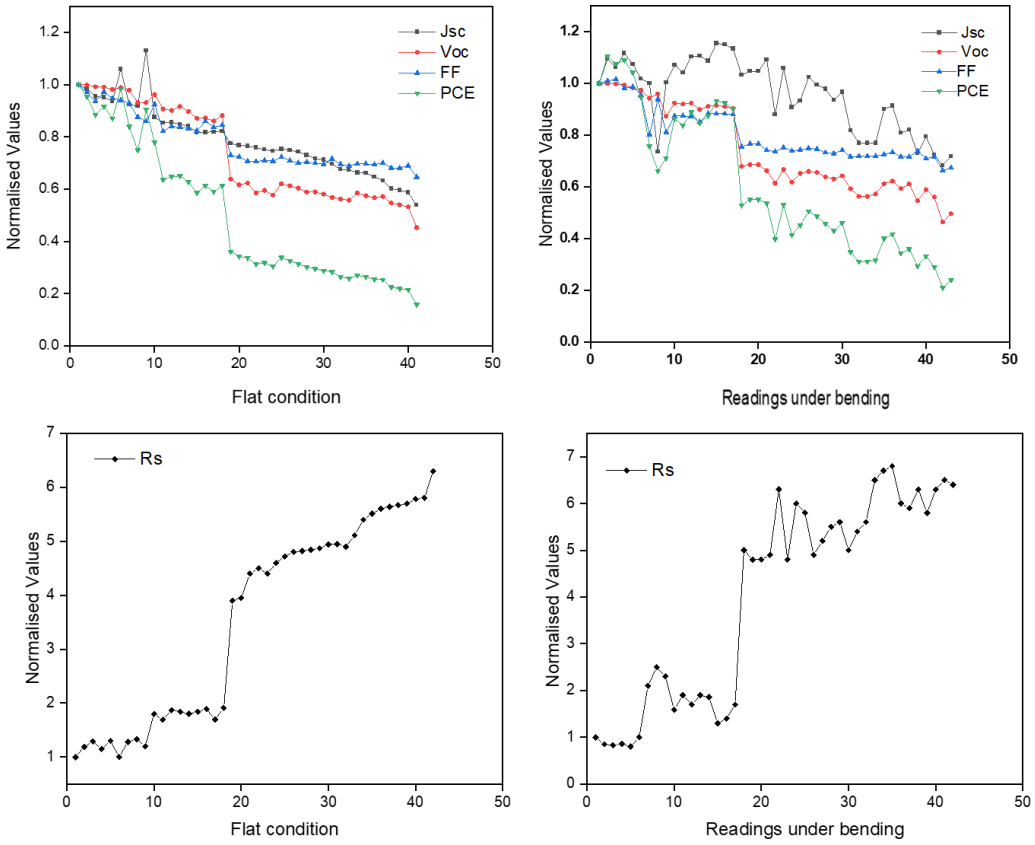

Figure 5- 15 shows the normalised values of flexible OPV performance parameters underwent in- situ bending under illumination where on the left the flexible OPV was flat. On the right the flexible OPV was at maximum bending with bending radius of 5 cm.

When comparing the results in Figure 5-15 to the results in Figure 4-8 (the OPV's performance parameters that were measured flat after 10, 50 and 100 bending cycles). With J_{sc}, the drop was 50% less sever, this could be attributed to the fact that the active layer is intact as no evidence of striation were noticed within the in-situ bending under illumination. The hypothesis in here is that the absence of the loading pin being constantly in touch with the sample during bending, could reduce the forces experienced by the sample and thus, keeping the active layer intact. Figure 5-16 show the optical microscopic images of the active layer after the institute test.

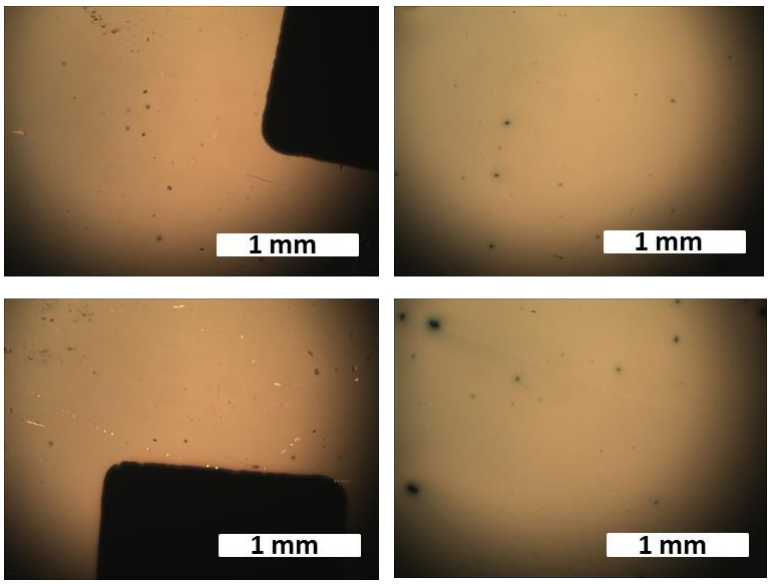

Figure 5- 16 Optical microscopic images of the active layer after the in-suit test of bending under illumination with bending radius 5 cm. The images were taken with 2.5x magnification. The small starches is believed to be due to handling the flexible solar cell.

Upon comparing the results of the in-situ while bending, which the results in Chapter 4 (Figure 4-8), it is clear that FF has similar trend, whereas V_{oc} dropped by around 20% more, this could be attributed to increase in temperature of the device, giving the number of times the solar simulator was operating during each J-V reading. Nonetheless, the drop in PCE in here is clearly associated with increase in R_s. Which can be explained by delamination process, which is now is understood to be between the active layer and MoOx layer, preventing an efficient hole extraction process which will also cause a drop in J_{sc}. From the in-situ bending system it was understood that the delamination could have a reversable effect upon bending of the

device, this explains the fluctuations noticed in R_s in Figure 5-15, and also the improvements of J_{sc} when the device is under bending. Thus, if we assume that within the set-up introduced here and bending radius of 5 cm, the delamination spot is back in back in contact when under bending, then R_s will reduce and J_{sc} will increase. However, as the performance of OPV under bending under illumination isn't investigated well in literature, further analysis is required to understand the improvement of J_{sc} under bending.

5.5 Encapsulation of flexible OPV via laminating technique.

Due to the high Young's modulus values of the materials involved in fabricating the OPVs, and the big difference in thickness between the substrate and the thin films within the OPV and with the absence of encapsulation, the neutral axis often lies within the flexible substrate instead of the midplane of the entire device. Nonetheless, according to literature, it has been demonstrated that upon introducing a sandwich encapsulating system, compressing by that the substrate and the thin films, the bending radius can be further reduced without damaging the device. At which, encapsulation would allow the movement of the natural axis towards the stiff, brittle thin films *i.e*, to the midplane [187]. The neutral axis will be within the midplane of the device if the following term is achieved [149].

$$E_s t_s^2 = E_e t_e^2$$

Where E_s and t_s are the Young's modulus and thickness of the substrate, respectively, and E_e and t_e are the Young's modulus and thickness of the encapsulation material, respectively. In this work, both the substrate and encapsulation are of the same materials, PET. Thus, E_s and E_e are the same with the value of 2.7 GPa. The thickness, however, slightly varies as the thickness of the substate is 0.21 mm and the thickness of the encapsulation (laminating sheet) is 0.15 mm, with 0.075 mm at top and bottom of the device. However, before encapsulation, It was important to ensure that the lamination technique and the bonding agent within the laminating sheets, would not hinder the light transmission to the PET/ITO substrate. Figure 5-

17 shows the transmittance spectra of the PET/ITO substrate before and after lamination *i.e*, encapsulating.

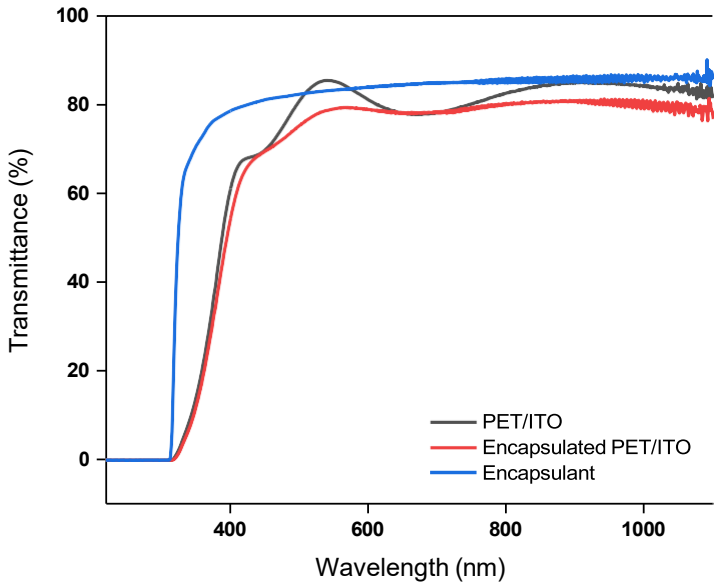

Figure 5- 17 Transmittance spectrum of PET/ITO before encapsulating (in black), the encapsulated PET/ITO (in red), and the encapsulate material (sheet) alone (in blue).

As Figure 5-17 indicate, the addition of the encapsulate did not hinder the optical transmission of the PET/ITO substrates. The overall transmission is appropriate for an OPV application. An appropriate wiring system was also important to establish to allow for proper encapsulation. The first method was utilizing silver paste to connect thin wires to the electrodes. Figure 5-18 shows the J-V curve of before and after encapsulation.

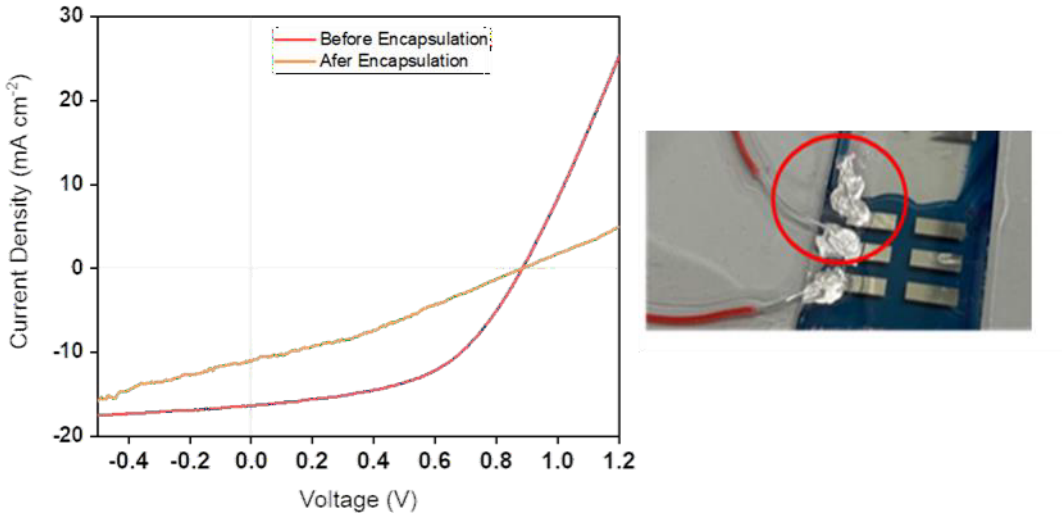

Figure 5- 18 J-V curve of a flexible OPV before encapsulation (in red) and after encapsulating (in orange).On the right, a picture of encapsulated OPV, utilising silver paste to connect the wires to the electrodes. The red circle shows the wires of one of the electrodes snaped off and issues associated with silver paste.

Table 5- 2 shows the performance parameters of flexible OPV before and after encapsulation, using silver paste to connect the wires.

	J_{sc} (A cm^{-2})	V_{oc} (V)	FF	PCE (%)	R_s (Ω)	R_{sh} (Ω)
Before encapsulation	-16.4	0.88	0.50	7.3	9.57	351.9
After encapsulation	-11	0.88	0.31	3	52.22	408.1

The J-V curves in Figure 5-18 and the performance parameters in Table 5-2 indicate that using silver paste is not suitable, as the PCE dropped from 7.3% to 3%. This drop in PCE which is associated with increase in R_s was attributed to the weak contact, as the silver paste did not attach the wire the electrodes properly and it was hard to control the area that the silver paste would stay on, and thus connecting multiple pixels together. Another issue with silver paste, silver paste would always dry thin and brittle, thus, any movement to the device would lead the wire to snap off and break as shown in Figure 5-18. Therefore, silver paste was

eliminated. Silver epoxy was also considered as it is a good candidate for applications requiring flexibility coupled with good electrical properties, however, epoxy resin requires annealing process at 50 °C for 5 minutes to dry, a process that was avoided as it could change the device interlayer's morphology and will not allow for clear comparison with device fabricated before encapsulation. Thus, the wiring process illustrated in Chapter 3, section 3.3 was adopted via the use of conductive tape, carbon paste and hot soldering. once the wires were connected, the device was encapsulated, and underwent continuous 100 bending cycles at a bending radius of 2.7 cm. Figure 5-19, illustrate the process bending and measuring the encapsulated devices. Figure 5-10, illustrates the J-V curves of three flexible OPVs before encapsulation, after encapsulation and after 100 bending cycles with bending radius of 2.7 cm.

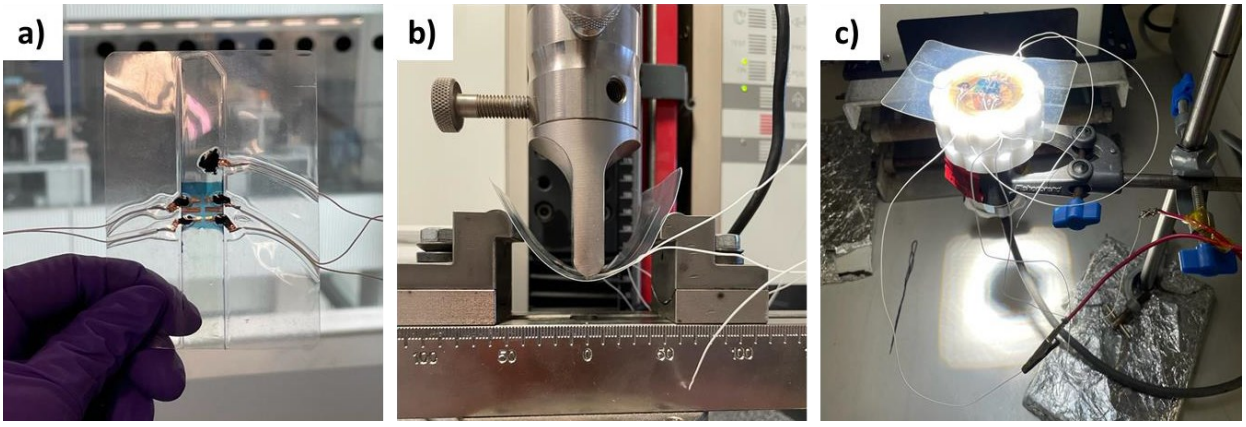

Figure 5- 19 A final encapsulated cell, b) the encapsulated cell under bending with bending radius of 2.7 cm with up to 100 bending cycles, d) the encapsulated cell under illumination after bending.

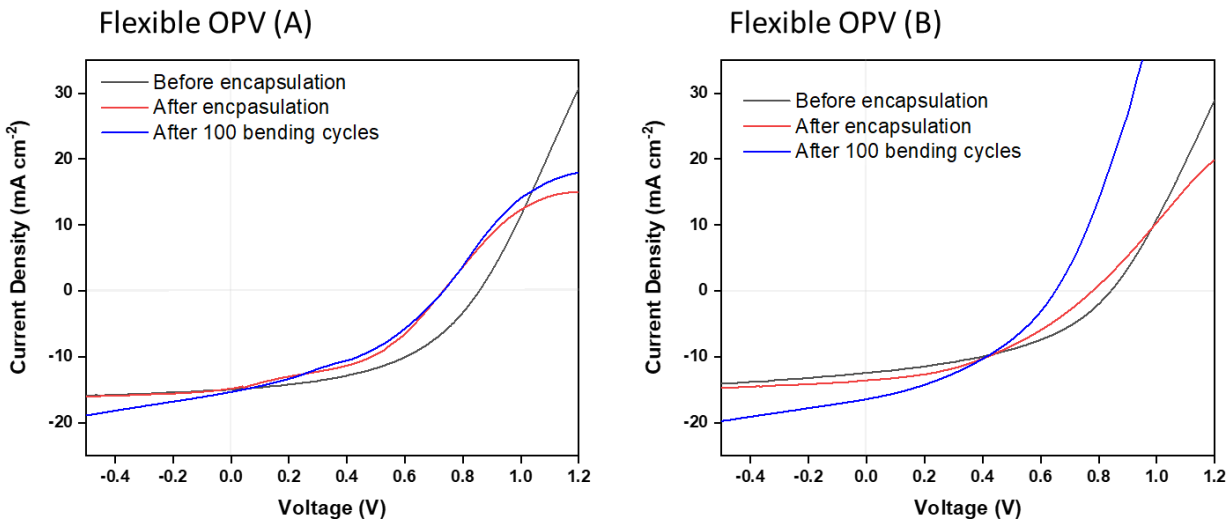

Figure 5- 20 J-V curves of two flexible OPVs before encapsulating (in black) after encapsulating (in red) and after 100 bending cycles at bending radius of 2.7 cm (in blue).

Table 5- 3 Shows the performance parameters of flexible OPVs before and after encapsulation and after 100 bending cycles of encapsulated device with 2.7 cm bending radius.

		J_{sc} (A/cm^2)	V_{oc} (V)	FF	PCE (%)	R_s (Ω)	R_{sh} (Ω)
Flexible OPV (A)	**Before encapsulation**	-14.9	0.85	0.47	6.0	15.6	317.2
	After encapsulation	-15.0	0.74	0.44	4.8	17.9	120.5
	After 100 bending cycles	-15.3	0.73	0.41	4.5	19.3	149.9
Flexible OPV (B)	**Before encapsulation**	-12.4	0.84	0.43	5.1	12.0	400.3
	After encapsulation	-13.6	0.78	0.40	4.2	19.2	208.1
	After 100 bending cycles	-15.4	0.65	0.39	4.1	22.3	133.1

As Figure 5-20 and table 5-3 show, the drop in PCE and the rise in R_s were not as severe as the case before encapsulation. So, although there is a difference of 0.06 mm in thickness between the substrate and the encapsulation sheet, the neutral axis did seem move towards the midplane of the device, and thus protecting the brittle interlayer with weak adhesion from any sever damages. It was also clear that the R_s increased after the encapsulation, which could be a result of the wiring system. A clear drop in V_{oc} and R_{sh} were noticed after encapsulation along with a slight drop in FF. Thus, it is believed that upon encapsulation a shunting path was created, which could have resulted from the heat experienced by the device during encapsulation process. Therefore, although further work is required to understand what happens to the device upon encapsulation, we assume that bending in this case had minimum impact to the device performance. In addition, it was clear that there is an increase in J_{sc} values after encapsulation and after 100 bending cycles which is more predominant in flexible OPV B. These results seem like an anomaly and further investigation is required. It is also worth mentioning that, when conducting this experiment, the device fabrication process, the encapsulation process, and J-V measurements were done at one campus (White city campus), while the mechanical bending tests were done at another campus (South Kensington campus), meaning the device had to be transported back and forward between the two campuses. Thus, although ambient stability test was not performed on an encapsulated device. Travelling between campuses (1 hour apart) without the use of vacuum sealed container could lead to some degradations.

5.6 FE analysis of the effect of encapsulation

FEA was carried out to further understand the effect of bending and visualise and obtain values of stress distribution the samples in this work underwent bending before and after encapsulation. Acknowledgements to Gorge Morgan who helped conducting these simulations. As indicated in Chapter 3, that in this simulation only the substrate and the encapsulate were taking into consideration. This was done because the simulation programme used was not able to sustain simulating bending for thin films within nm range of thickness. Figure 5-21 show the results of the simulation from a front and top view. In the unencapsulated scenario, as the bending radius reduces, the distribution of high Von Mises stress across the upper surface increase as well. This was expected as higher forces were required to bending the device further. The forces extracted from the simulation required to bend the unencapsulated substrate were 0.134 N, 0.260 N and 0.425 N for bending radius of 10 cm, 5 cm, and 2.7 cm, respectively (See chapter 3, Section 3.4). It is also clear that once the substrate was encapsulated, a higher stress distribution was noticed at bending radius of 5 cm. This was expected as increasing the thickness will require higher force of bending. The forces required to bend the encapsulated substrates are, 2.016 N, 1.234 N, and 0.637 N for bending radius of 2.7 cm, 5 cm, and 10 cm, respectively. Nonetheless, the stress distribution on the top surface of the device was always bound to be higher, as it is direct contact with the loading pin. However, the main interest in here is the distribution of the stress vertically across z-axis, to further understand the stress that the device is experiencing. This is because the OPV would be fabricated on the lower edge of the substrate.

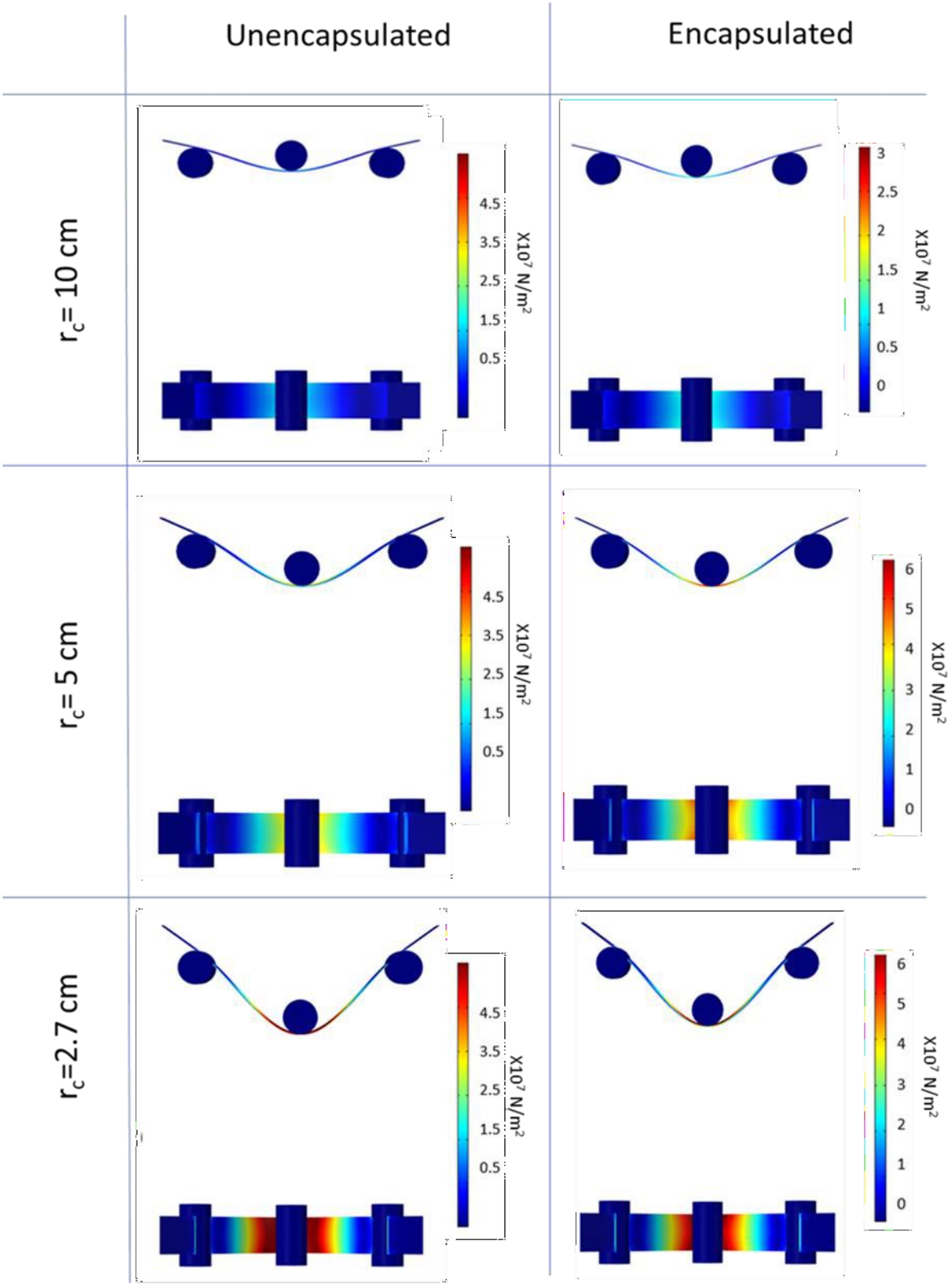

Figure 5- 21 The simulated results of unencapsulated substate under bending with three different bending radiuses of 10 cm, 5 cm and 2.7 cm with loading force of 0.134 N, 0.260 N and 0.425 N, respectively. On the right are the simulated results of an encapsulated substate under bending with three different bending radiuses of 10 cm, 5 cm and 2.7 cm with loading force of 2.016 N, 1.432 N, and 0.63 N respectively. The colour gradient refers to the Von Mises stress distribution.

Figure 5-21 shows the simulated stress distribution z-axes of the substrate before and after encapsulation. This was of an interest because at the lower edge of the substrate, is where the OPV will be fabricated. Thus, it was important to know the tensile stress the device would be experienced when not encapsulated. Starting with 10 cm bending radius in, in the unencapsulated scenario, the stress distribution across the substrate, is around $0.5x10^7$ N m^{-2} across the entire sample thickness. Meaning the results of device performance obtained in this work related to 10 cm bending radius were not affected by such value of tensile stress. However, once the encapsulate was add, although the stress distribution increased throughout the thickness of the substrate of around $1.5x10^7$ N m^{-2} , which is expected due to the increase of thickness. The neutral axis (blue line) can be seen passing through what seems like the midplane. The blue line indicates an area with the stress at that plane is 0, i.e; neutral axis. At 5 cm bending radius, in the case of un-encapsulation, the stress distribution though z-axis of the substrate and more specifically at the lower edge of the substrate, is around $2.5x10^7$ N m^{-2}. However, upon encapsulation, a clear blue line (neutral axis) passes by what we are expecting the device will be pushed at after encapsulation. At 2.7 cm bending radius, the substrate experiences stress of around $3.5x10^7$ N m^{-2} without encapsulation In the case of encapsulation, although the neutral axis (blue line) is not very clear here when looking at Figure 5-22, it shows a very clear stress distribution under bending, where below the neutral axis, at the very end, the sample experiences maximum tensile stress, and above the neutral axis, where the loading pin is in direct contact, the sample experience maximum compression stress. Thus, the gradient change of stress distribution between the two ends, is where the neutral axis is located. This proves the theory we speculated at Section 5.5 of this work. Where encapsulated OPV performance parameters were compared to before encapsulation and before 100 bending cycles at 2.7 cm bending radius, at which, the degradation of the device performance after bending was actually a continues effect of the shutting path created by the encapsulation technique used in this work *i.e,* degradation due to lamination and not due to mechanical deformation.

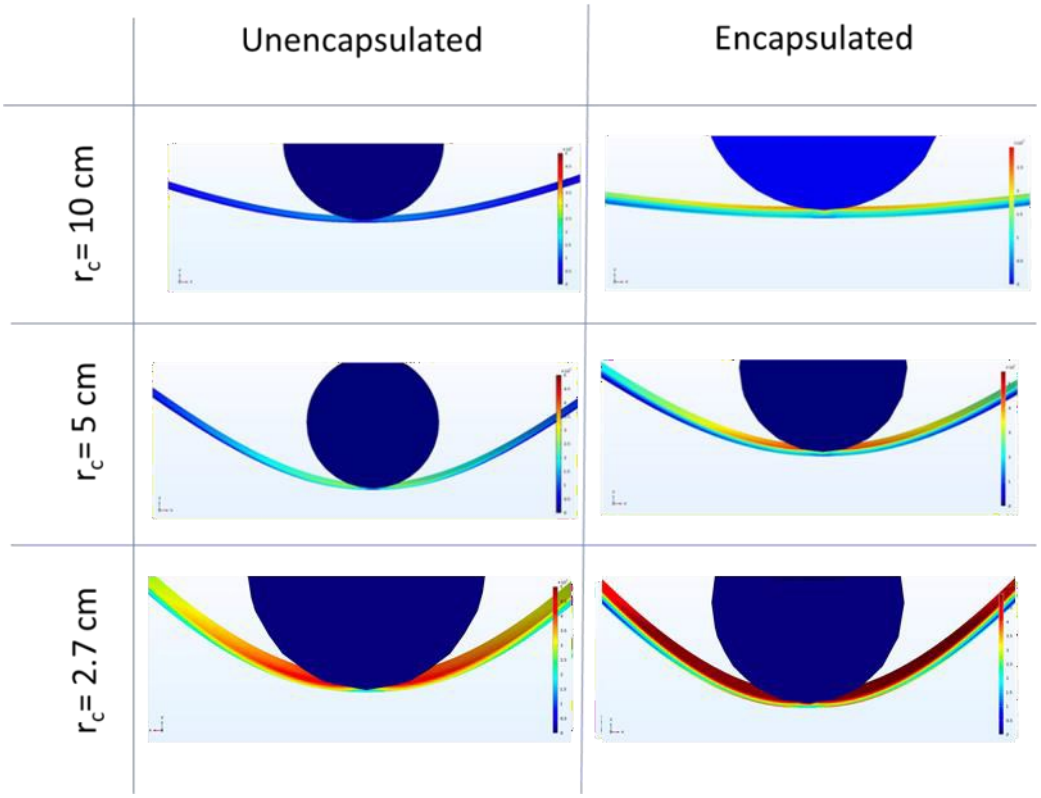

Figure 5- 22 A zoomed view of the simulated results to observe the change in stress distribution along z-direction, of unencapsulated substate under bending with three different bending radiuses of 10 cm, 5 cm and 2.7 cm with loading force of 0.134 N, 0.260 N and 0.425 N, respectively. On the right are the simulated results of an encapsulated substate under bending with three different bending radiuses of 10 cm, 5 cm and 2.7 cm with loading force of 0.63N, 1.234 N, and 2.016 N respectively. The colour gradient refers to the Von Mises stress distribution

5.5 Conclusion

In this chapter, answers as to the causes of flexible OPV mechanical degradation due to 3 point bending test under three bending radiuses of 2.7 cm, 5 cm and 10 cm discussed in the previous chapter was obtained. The neutral axis position was calculated which was at around 0.11 mm from the surface of the PET/ITO substrate. The tensile flexural stain that the ITO experience upon bending was also calculated to be around $3.89x10^{-3}$ %, $2.11x10^{-3}$ % and $1.10x10^{-3}$ % for bending radius of 2.7 cm, 5 cm and 10 cm, respectively. ITO layer's sheet resistivity before and after 100 bending cycles at 3 different bending radiuses were measures and remined constant, indicating that the ITO layer did not undergo any mechanical degradation. A novel method of monitoring the electrical resistance of the device while bending was used, to investigate the effect of bending on the interfaces and the individual layers. The work conducted in this thesis, proves the reliability of the new in-situ bending introduced here. Where when references indicated week peeling strength, a clear trend of increasing resistance while bending was notices. Additionally, the in-situ bending system was able to detect delamination by presenting a resistance overload. Within the OPV devices fabricated in this work with the structure of (PET/ITO/ITIC:PBDP-T/MoOx/Ag), two main weak links leading to the mechanical degradation were concluded. A weak interface between MoOx and the active layer. This was in the form of continuous increase in resistance during bending at 5 cm bending radius, and a resistance overload at 2.7 cm bending radius. This was also confirmed by comparing the performance of MoOx and ZnO along first under bending, then followed by the addition of the active layer along with referring to a peeling strength values published in literature. Additionally, this was proved via the manual peeling test that was preformed, where the silver layer was completely removed with some additional layer on top. Given the active layer was intact, and the lighter colour on top of the silver indicates that its MoOx layer. Thus, proving the weak interface is between MoO and the active layer. The effected link was found to be the active layer, as after 100 bending cycles, striation started to appear at 5 cm bending radius, and were more obvious at 2.7 bending radius. These striations could be the results of having SM-based acceptors and the polymer donor, thus, creating weak spots due to unconnected molecules, that translated into stretch marks upon bending, although the striations seem to be an effect of bending radius, it was clear that they were not within the same direction as the bnding axis, thus it is believed that a pressure point either due to fabrication or created during mechanical testing was the starting point of these

striations . An in house, system was created to understand the behaviour of an OPV under bending, while under illumination with the focus of bending radius of 5 cm due to limitation of the system. An interesting improvement of J_{sc} was observed when the device was under bending conditions, this could be associated with changing the incident light angle and thus enhancing light intensity, however, further analysis is required to confirm the theory. Finally, the flexible OPVs were encapsulated via lamination techniques, in an attempt to move the neutral axis towards the device layers. Although the performance parameters where not degraded with the same severity as an un-encapsulated device. It is believed that the degradation which is governed by reduction in V_{oc}, FF and R_{sh}, is resulted from creating a shunting path within the device, while encapsulation. The FE analysis does prove that for the substrate, and encapsulating materials and thickness used in this work, and at 2.7 cm bending radius, the neutral axis is positioned in midplane. Thus, further analysis to the effect of encapsulation might be required.

Chapter 6

Conclusion and future outlook

The overall goal of this thesis was to be able to answer the simple question as to how the performance parameters of a flexible OPV changes as it experiences flexural bending. Answering this question first started with examining the optical properties of the PET/ITO substrates and ensuring its compatibility with well documented glass/ITO substrates. An inverted OPV with structure of (PET/ITO/ZnO/ITIC:PBDP-T/MoOx/Ag) was chosen for this study. As the device is fabricated, evaluated and mechanically tested under ambient conditions instead of inside the glovebox, the ambient stability of the device was tested. It showed that the device is stable within the first 20 hours of fabricating the device. Thus, allowing a window to mechanically test an unencapsulated device under ambient condition without having an effect of environmental ambient degradation. 3-point bending machine was utilised to test the mechanical durability of the device by preforming flexural bending test. Three different bending radiuses of 2.7 cm, 5 cm and 10 cm, and the devices were tested under illumination after 10, 50 and 100 bending cycles. From there, it was noted that the mechanical degradation resulted in dramatic drop in J_{sc}, PCE, along with dramatic increase in R_s. The initial hypothesis, was a damage to one or more interfaces within the device layers, leading to poor collection of the generated charges. Thus leading to a drop in J_{sc} which linked with a drop in R_s. The investigation started with calculating the position of the neutral axis, it was found to be at 0.11 mm from the surface of the PET/ITO substrate. That meant that the ITO layer was experiencing tensile strain which was calculated to be around the value of 3.89×10^{-3} %, 2.11×10^{-3} % and 1.10×10^{-3} % for bending radius of 2.7 cm, 5 cm and 10 cm, respectively. Nonetheless, these tensile strains did not cause any mechanical deformation to the ITO layer as sheet resistance remined intact. A novel method of monitoring the electrical resistance of the device while bending was used, to investigate the effect of bending on the interfaces and the individual layers. The work conducted in this thesis, proves the reliability of the new in- situ bending introduced here. Where when literature references indicated week peeling strength clear trend of increasing resistance while bending was noticed.

Additionally, the in-situ bending system was able to detect delamination by presenting a resistance overload. Where, sandwich devices of PET/ITO/ZnO/Ag and PET/ITO/MoOx/Ag were tested. The reliability of the system introduced was proved by comparing a ZnO sandwich device before and after enhancing its peeling strength with ITO. In which when literature reported a low peeling strength the system introduced confirmed a resistance overload i.e, delamination at 5 cm bending radius. Although the with MoOx might require further analysis to fully understand the evolution of the resistance beyond the tested cycles. None of the interlayers showed any weak interfaces with their respective electrodes at least 5 cm bending radius. Thus, the test was carries on a full device. by relaying on peeling strength from literature, a weak interface between MoOx and the active layer was detected. This was in the form of continuous increase in resistance during bending at 5 cm bending radius, and a resistance overload at 2.7 cm bending radius. Additionally, to further confirm this, a manual peeling test was preformed to an incapsulated sample, upon removal of the top layer of the laminate, the silver electrode was completely removed with some additional layer on top wich was lighter in colour, although EDX was not performed, it is expected to be the MoO layer. for future reference it is recommended to utilize EDX to further confirm.

The second mechanical degradation was witnessed in the active layer, as after 100 bending cycles, striation started to appear at 5 cm bending radius, and were more obvious at 2.7 bending radius. These striations could be the results of having SM-based acceptors and the polymer donor, thus, creating weak spots, which translated into striation upon bending. Thus, explaining overall mechanical deformation the device experienced upon bending for 100 bending cycles at 2.7 cm and 5 cm bending radiuses. At which, the delamination would have caused the R_s values to increase, and the damages notices in the active layer could lead to reduction in J_{sc} due to possible charge recombination processes. An in house, novel system was utilised in this study to understand the behaviour of an OPV under bending, while under illumination with the focus of bending radius of 5 cm due to limitation of the device. An interesting improvement of J_{sc} was observed when the device was under bending conditions, this could be associated with changing the incident light angle however, further analysis is required to confirm the theory. Additionally, when comparing the results of the in-situ bending under illumination and the as to when the device J-V curves are measured after a given number of cycles in a flat position, V_{oc} seems to drop by 20% more in the in-situ experiment, this could be due to increase in temperature of the device due to the long period

the device was tested under illumination. Additionally, by combining the two in-situ bending tests, it was noticed that delamination has a reversable effect, meaning that upon bending the device and flattening it, the delamination area changes and thus fluctuations to the R_s is noticed.

Finally, the OPVs were encapsulated via lamination techniques, in an attempt to move the neutral axis towards the device layer and thus, protecting any weak interfaces. Although the performance parameters where not degraded with the same severity as an un-encapsulated device. It is believed that the degradation, which is governed by reduction in V_{oc}, FF and R_{sh}, is resulted from creating a shunting path within the device. This could be the results of heat experienced by the device during encapsulation. The FE analysis does prove that for the substrate, and encapsulating materials and thickness used in this work, and at 2.7 cm bending radius, the neutral axis is position midplane. Thus, further analysis to the effect of encapsulation might be required.

In here, we state recommendations and future workout to the work discussed in this thesis. Within the novel in-situ bending system introduced in this work, it is hard to differentiate weather the changes in resistance is due to which specific weak interface within the device. Thus, it is recommended in the future to introduce one individual layer at a time. This would help with detecting the week interface one step at a time. For example, user should start with PET/ITO/ZnO/Ag sandwich device, as done in this work, where we understand now that upon 5 minutes of UV-ozone, the interface between ZnO and ITO becomes more stable. Then follow that adding the active layer, then follow that by adding the MoOx layer. Thus, along with the information reported in this thesis, it would be easier to detect the weak interfaces, by comparing the magnitude and trends of resistance change while bending. However in doing so it is important to note the change of strain applied to the last layer upon bending, ass the maximum strain/stress will always be applied to the most top and bottom layer of the structure.

As mentioned above, this new proposed method dose not replace any quantitative method such as peeling strength test and adhesion energy via 4-point bending tests, however, the concept here is to determine how do these values translate into bending, giving the user a limits to bending radius and bending cycles an interface or a material can withstand before an overload of resistance is recorded which is believed to be a feature associated with delamination. To further support the reliability of the new system introduced in this work, a

peeling strength, or an adhesion measurement for the specific OPV structure fabricated in this work is suggested. Another technique that can be done on the absence of a peeling strength, is to utilize AFM technique in a contact mode to scratch the electrode and MoO layer, and record the forced required for that.

Moreover, when using the in-situ bending system, for a given bending radius, it is suggested to not stop the bending cycles until no further changes are recorded to resistance or until an overload occurs this would help with confirming the effect of 2.7 cm bending radius on MoOx sandwich device. A proposed method to further confirm a delamination between MoOx and the active layer, is to remove the Ag/MoOx layer using a magic scotch tape (as it does not leave any residuals nor dose it damage the flexible substrate upon removing it) unlike the the manual peeling test preformed in this work using lamination. After that, re-evaporate MoOx and Ag layer again. If the effects of bending were found reversible after evaporating the new layers, this could be evidence of delamination. Additionally, as for the effect of increasing the temperature during bending under illumination, temperature probing can be utilised to further confirm the reduction in V_{oc} in the in-situ bending analysis. As for the features observed in the active layer after 100 bending cycles at bending radiuses of 5 cm and 2.7 cm, a mapping Raman Spectroscopy would help seeing changes in concentration of one of the components (donor/acceptor) or changes within the BHJ structure at specifically the striation spots.

One of the main challenges faced in this work, is the inability to access SEM facilities and lack of expertise with SEM/TEM. It was attempted to conduct an in-situ bending within SEM. Where within the flexible substrate used in this work illustrated in Figure 3-1 in Chapter 3, the side PET (area of PET around the pre-patterned ITO) was removed, and the devices were fabricated only on top of the ITO layer. The devices then underwent 100 bending cycles for 10 cm, 5 cm and 2.7 cm bending radius. After that, the devices were wrapped around the SEM holders. As the side PET section was removed, theoretically, one would be able to look directly into the cross section and thus being able to look at the damages/delamination caused by the 3-point bending test (See Appendix F). However, no clear images were able to be extracted. Thus, it is proposed to repeat this experiment with more experienced SEM expert.

References

1. Li, N., et al., *Towards commercialization: the operational stability of perovskite solar cells.* Chemical Society Reviews, 2020. **49**(22): p. 8235-8286.
2. Goverment, H., *The Carbon Plan: Delivering our low carbon future*, D.o.E.a.C. Change, Editor. 2011: 3 Whitehall Place p. 218.
3. Hart, M., *Hubris: The Troubling Science, Economics, and Politics of Climate Change* . Vol. 1. 2015, Canada Compleat Desktops Publishing, a division of Compleat Desktops R&D Inc.
4. Muhammad Luqman, S.R.A., Samiullah Khan, Usman Ahmad, Ahmad Raza, Farkhanda Akmal, *Estimation of Solar Energy Potential from Rooftop of Punjab Government Servants Cooperative Housing Society Lahore Using GIS.* Smart Grid and Renewable Energy, 2015. **6**(5).
5. Ali Assi, M.J., Maitha Al-Shamisi, *Prediction of Global Solar Radiation in Abu Dhabi.* Hindawi, 2012. **2012**.
6. Burnett, D., E. Barbour, and G.P. Harrison, *The UK solar energy resource and the impact of climate change.* Renewable Energy, 2014. **71**: p. 333-343.
7. IEA, *Renewables 2020*. 2020: Paris.
8. Chapin, D.M., C.S. Fuller, and G.L. Pearson, *A New Silicon p ‐ n Junction Photocell for Converting Solar Radiation into Electrical Power.* Journal of Applied Physics, 1954. **25**(5): p. 676-677.
9. Chen, Y., et al., *From Laboratory to Production: Learning Models of Efficiency and Manufacturing Cost of Industrial Crystalline Silicon and Thin-Film Photovoltaic Technologies.* IEEE Journal of Photovoltaics, 2018. **8**(6): p. 1531-1538.
10. Richter, A., M. Hermle, and S.W. Glunz, *Reassessment of the Limiting Efficiency for Crystalline Silicon Solar Cells.* IEEE Journal of Photovoltaics, 2013. **3**(4): p. 1184-1191.
11. Green, M.A., et al., *Solar cell efficiency tables (Version 55).* Progress in Photovoltaics: Research and Applications, 2020. **28**(1): p. 3-15.
12. Wilson, G.M., et al., *The 2020 photovoltaic technologies roadmap.* Journal of Physics D: Applied Physics, 2020. **53**(49): p. 493001.
13. Castillo-Aguilella, J.E. and P.S. Hauser, *Multi-Variable Bifacial Photovoltaic Module Test Results and Best-Fit Annual Bifacial Energy Yield Model.* IEEE Access, 2016. **4**: p. 498-506.
14. Huang, W., et al., *Efficient and Mechanically Robust Ultraflexible Organic Solar Cells Based on Mixed Acceptors.* Joule, 2020. **4**(1): p. 128-141.
15. Li, Y., et al., *High-efficiency robust perovskite solar cells on ultrathin flexible substrates.* Nature Communications, 2016. **7**(1): p. 10214.
16. Park, J., et al., *Flexible single-strand fiber-based woven-structured triboelectric nanogenerator for self-powered electronics.* APL Materials, 2018. **6**(10): p. 101106.
17. Zhang, K., et al., *High-Performance Polymer Tandem Solar Cells Employing a New n-Type Conjugated Polymer as an Interconnecting Layer.* Adv Mater, 2016. **28**(24): p. 4817-23.
18. Abate, A., et al., *Perovskite Solar Cells: From the Laboratory to the Assembly Line.* Chemistry – A European Journal, 2018. **24**(13): p. 3083-3100.
19. Bonaccorso, F., et al., *2D materials. Graphene, related two-dimensional crystals, and hybrid systems for energy conversion and storage.* Science (New York, N.Y.), 2015. **347**: p. 1246501.
20. Cheng, P. and X. Zhan, *Stability of organic solar cells: challenges and strategies.* Chemical Society Reviews, 2016. **45**(9): p. 2544-2582.
21. Verlinden, P.J., et al., *Sliver® solar cells: A new thin-crystalline silicon photovoltaic technology.* Solar Energy Materials and Solar Cells, 2006. **90**(18): p. 3422-3430.
22. Kayes, B.M., et al. *27.6% Conversion efficiency, a new record for single-junction solar cells under 1 sun illumination*. in *2011 37th IEEE Photovoltaic Specialists Conference*. 2011.

23. Reinhard, P., et al. *High efficiency flexible Cu(In,Ga)Se2 solar cells*. in *Proceedings of the 20th International Workshop on Active-Matrix Flatpanel Displays and Devices: TFT Technologies and FPD Materials, AM-FPD 2013*. 2013.
24. Fu, X., et al., *Flexible solar cells based on carbon nanomaterials.* Carbon, 2018. **139**: p. 1063-1073.
25. Bässler, A.K.H., *The Electronic Structure of Organic Semiconductors*, in *Electronic Processes in Organic Semiconductors*. 2015. p. 1-86.
26. Ding, J.M., et al., *Patternable polymer bulk heterojunction photovoltaic cells on plastic by rotogravure printing.* Solar Energy Materials and Solar Cells, 2009. **93**(4): p. 459-464.
27. Weiran, C., et al., *Transparent electrodes for organic optoelectronic devices: a review.* Journal of Photonics for Energy, 2014. **4**(1): p. 1-28.
28. Salvatierra, R.V., et al., *ITO-Free and Flexible Organic Photovoltaic Device Based on High Transparent and Conductive Polyaniline/Carbon Nanotube Thin Films.* Advanced Functional Materials, 2013. **23**(12): p. 1490-1499.
29. Klauk, H., *Charge Transport Theories in Organic Semiconductors*, in *Organic Electronics II*. p. 67-104.
30. Singleton, J., *Band Theory and Electronic Properties of Solids*. Oxford Master Series in Physics (Book 2). Vol. 1. 2001, UK: Oxford University Press. 240.
31. Mark Geohegan, G.H., *Polymer Electronics*. 2013, United Kingdom: OXFORD university press.
32. Greeves, N. *ChemTube3D*. 2008 30.1.2021]; Available from: www.chemtube3d.com.
33. Fleming, I., *Molecular Orbital Theory*, in *Molecular Orbitals and Organic Chemical Reactions*. 2010. p. 1-67.
34. Haas, K. *Molecular Orbitals*. 2020 2020/09/27 [cited 2020 28th January]; Available from: https://chem.libretexts.org/@go/page/151386.
35. Ashenhurst, J. *Bonding And Antibonding Pi Orbitals*. Master Organic Cemistry 2020 February 9th, 2020 [cited 2021 02-02]; Available from: https://www.masterorganicchemistry.com/2017/02/14/molecular-orbital-pi-bond/#comment-597133.
36. Reusch, W. *Aromaticity - Benzene and Other Aromatic Compounds*. Virtual Textbook of Organic Chemistry 2013 [cited 2021 02-02]; Available from: https://www2.chemistry.msu.edu/faculty/reusch/VirtTxtJml/intro1.htm#contnt.
37. Alan J. Heeger, A.G.M., and Hideki Shirakawa, *Macromolecules.* Macromolecules, 2002. **35**(4): p. 1137-1139.
38. Cavendish Laboratory, C. *Organic Semiconductors*. Optoelectronics [cited 2021 02-01].
39. Kahn, A., *Fermi level, work function and vacuum level.* Materials Horizons, 2016. **3**(1): p. 7-10.
40. Nelson, J., *Polymer:fullerene bulk heterojunction solar cells.* Materials Today, 2011. **14**(10): p. 462-470.
41. Emmott, C.J.M., et al., *Organic photovoltaic greenhouses: a unique application for semi-transparent PV?* Energy & Environmental Science, 2015. **8**(4): p. 1317-1328.
42. Arbouch, I., Y. Karzazi, and B. Hammouti, *Organic photovoltaic cells: Operating principles, recent developments and current challenges – review.* Physical and Chemical News, 2014. **72**: p. 73-84.
43. Augustin McEvoy, L.C., Tom Markvart, *Solar Cells: Materials, Manufacture and Operation*. 2012: Academic Press. 547.
44. Cahen, D. and A. Kahn, *Cahen, D. & Kahn, A. Electron energetics at surfaces and interfaces: Concepts and experiments. Adv. Mater. 15, 271-277.* Advanced Materials, 2003. **15**: p. 271-277.
45. Ishii, H., et al., *Energy Level Alignment and Interfacial Electronic Structures at Organic/Metal and Organic/Organic Interfaces.* Advanced Materials, 1999. **11**(8): p. 605-625.
46. Plummer, E.W., et al., *Photoelectron spectra of adsorbed species on tungsten.* Progress in Surface Science, 1976. **7**(3): p. 149-182.

47. Janssen, R.A.J. and J. Nelson, *Factors Limiting Device Efficiency in Organic Photovoltaics.* Advanced Materials, 2013. **25**(13): p. 1847-1858.
48. Brabec, C.J., Dyakonov, V., Parisi, J., Sariciftci, N.S. (Eds.), *Organic Photovoltaics: Concepts and Realization*. 1 ed. 2003: Springer-Verlag Berlin Heidelberg. 300.
49. Himmelberger, S. and A. Salleo, *Engineering semiconducting polymers for efficient charge transport.* MRS Communications, 2015. **5**(3): p. 383-395.
50. Noriega, R., *Efficient Charge Transport in Disordered Conjugated Polymer Microstructures.* Macromolecular Rapid Communications, 2018. **39**(14): p. 1800096.
51. Hou, J., et al., *Organic solar cells based on non-fullerene acceptors.* Nat Mater, 2018. **17**(2): p. 119-128.
52. Scharber, M.C., et al., *Design Rules for Donors in Bulk-Heterojunction Solar Cells—Towards 10 % Energy-Conversion Efficiency.* Advanced Materials, 2006. **18**(6): p. 789-794.
53. Zhao, W., et al., *Fullerene-Free Polymer Solar Cells with over 11% Efficiency and Excellent Thermal Stability.* Advanced Materials, 2016. **28**(23): p. 4734-4739.
54. Shrotriya, V., et al., *Transition metal oxides as the buffer layer for polymer photovoltaic cells.* Applied Physics Letters, 2006. **88**.
55. Gaspar, H., et al., *Recent Developments in the Optimization of the Bulk Heterojunction Morphology of Polymer: Fullerene Solar Cells.* Materials (Basel, Switzerland), 2018. **11**(12): p. 2560.
56. Hutten, P.G.H.D.P.F.v., *Semiconducting Polymers: Chemistry, Physics and Engineering*. 1990: 1999 Wiley‐VCH Verlag GmbH.
57. Yu, G., et al., *Polymer photovoltaic cells: enhanced efficiencies via a network of internal donor-acceptor heterojunctions.* Science, 1995. **270**: p. 1789+.
58. Castaner, A.M.T.M.L.C.T.M.L., *Practical Handbook of Photovoltaics: Fundamentals and Applications*. 2003: Elsevier Science. 998.
59. Shahin, S., P. Gangopadhyay, and R. Norwood, *Ultrathin organic bulk heterojunction solar cells: Plasmon enhanced performance using Au nanoparticles.* Applied Physics Letters, 2012. **101**: p. 053109.
60. Yang, Y. and G. Li, *Fundamentals, Materials, Devices and Fabrication*, in *Progress in High-Efficient Solution Process Organic Photovoltaic Devices*. 2015, Springer-Verlag Berlin Heidelberg. p. 417.
61. Gilot, J., M.M. Wienk, and R.A.J. Janssen, *Double and triple junction polymer solar cells processed from solution.* Applied Physics Letters, 2007. **90**(14): p. 143512.
62. Halls, J.J.M., et al., *Efficient photodiodes from interpenetrating polymer networks.* Nature, 1995. **376**(6540): p. 498-500.
63. Brabec, C., et al., *Origin of the Open Circuit Voltage of Plastic Solar Cells.* Advanced Functional Materials, 2001. **11**: p. 374-380.
64. Brabec, C.J., et al., *Origin of the Open Circuit Voltage of Plastic Solar Cells.* Advanced Functional Materials, 2001. **11**(5): p. 374-380.
65. Blakesley, J.C. and N.C. Greenham, *Charge transfer at polymer-electrode interfaces: The effect of energetic disorder and thermal injection on band bending and open-circuit voltage.* Journal of Applied Physics, 2009. **106**(3): p. 034507.
66. Scharber, M., et al., *Design Rules for Donors in Bulk‐Heterojunction Solar Cells—Towards 10 % Energy‐Conversion Efficiency.* Advanced Materials, 2006. **18**: p. 789-794.
67. Servaites, J.D., M.A. Ratner, and T.J. Marks, *Organic solar cells: A new look at traditional models.* Energy & Environmental Science, 2011. **4**(11): p. 4410-4422.
68. Hsieh, Y.-T., et al., *Mechanically robust, stretchable organic solar cells via buckle-on-elastomer strategy.* Organic Electronics, 2018. **53**: p. 339-345.
69. Servaites, J., M. Ratner, and T. Marks, *Organic solar cells: A new look at traditional models.* Energy Environ. Sci., 2011. **4**: p. 4410-4422.

70. Sharma, S., et al., *Alternative transparent conducting electrode materials for flexible optoelectronic devices.* Opto-Electronics Review, 2018. **26**: p. 223-235.
71. Abdulrazzaq, O.A., et al., *Organic Solar Cells: A Review of Materials, Limitations, and Possibilities for Improvement.* Particulate Science and Technology, 2013. **31**(5): p. 427-442.
72. Cao, W., et al., *Transparent electrodes for organic optoelectronic devices: a review.* Journal of Photonics for Energy, 2014. **4**(1): p. 040990.
73. Kang, S., et al., *Capillary Printing of Highly Aligned Silver Nanowire Transparent Electrodes for High-Performance Optoelectronic Devices.* Nano Lett, 2015. **15**(12): p. 7933-42.
74. Yin, X., et al., *Highly Efficient Flexible Perovskite Solar Cells Using Solution-Derived NiOx Hole Contacts.* ACS Nano, 2016. **10**(3): p. 3630-3636.
75. Zhu, R., Z. Zhang, and Y. Li, *Advanced materials for flexible solar cell applications.* 2019. **8**(1): p. 452.
76. Hashemi, S.A., S. Ramakrishna, and A.G. Aberle, *Recent progress in flexible–wearable solar cells for self-powered electronic devices.* Energy & Environmental Science, 2020. **13**(3): p. 685-743.
77. Bhosle, S., R. Tewari, and C. Friedrich, *Dependence of Nanotextured Titanium Orthopedic Surfaces on Electrolyte Condition.* Journal of Surface Engineered Materials and Advanced Technology, 2016. **06**: p. 164-175.
78. Wang, W., et al., *Transparent, Double-Sided, ITO-Free, Flexible Dye-Sensitized Solar Cells Based on Metal Wire/ZnO Nanowire Arrays.* Advanced Functional Materials, 2012. **22**(13): p. 2775-2782.
79. Pandey, M., et al., *Dependence of ITO-Coated Flexible Substrates in the Performance and Bending Durability of Perovskite Solar Cells.* Advanced Engineering Materials, 2019. **21**(8): p. 1900288.
80. Root, S.E., et al., *Mechanical Properties of Organic Semiconductors for Stretchable, Highly Flexible, and Mechanically Robust Electronics.* Chemical Reviews, 2017. **117**(9): p. 6467-6499.
81. Tahk, D., H.H. Lee, and D.-Y. Khang, *Elastic Moduli of Organic Electronic Materials by the Buckling Method.* Macromolecules, 2009. **42**(18): p. 7079-7083.
82. Printz, A.D., et al., *Yield Point of Semiconducting Polymer Films on Stretchable Substrates Determined by Onset of Buckling.* ACS Applied Materials & Interfaces, 2015. **7**(41): p. 23257-23264.
83. Awartani, O., et al., *Correlating Stiffness, Ductility, and Morphology of Polymer:Fullerene Films for Solar Cell Applications.* Advanced Energy Materials, 2013. **3**(3): p. 399-406.
84. Han, J.H. and K.C. Choi, *P-104: A Transparent, Flexible, Patternable Electrode Using a Multilayer Film Structure.* SID Symposium Digest of Technical Papers, 2016. **47**(1): p. 1519-1522.
85. Guo, X., et al., *Highly Conductive Transparent Organic Electrodes with Multilayer Structures for Rigid and Flexible Optoelectronics.* Scientific reports, 2015. **5**: p. 10569.
86. Fukuda, K., K. Yu, and T. Someya, *The Future of Flexible Organic Solar Cells.* Advanced Energy Materials, 2020. **10**(25): p. 2000765.
87. ToolBox, E. [cited 2021 25th January]; Available from: https://www.engineeringtoolbox.com/young-modulus-d_417.html.
88. Hengst, C., et al., *Mechanical Properties of ZTO, ITO, and a-Si:H Multilayer Films for Flexible Thin Film Solar Cells.* Materials (Basel, Switzerland), 2017. **10**(3): p. 245.
89. Jiang, J.-W., J.-S. Wang, and B. Li, *Young's modulus of graphene: A molecular dynamics study.* Physical Review B, 2009. **80**(11): p. 113405.
90. Qu, J., et al., *Stiffness, strength and adhesion characterization of electrochemically deposited conjugated polymer films.* Acta biomaterialia, 2016. **31**: p. 114-121.
91. Jain, A., et al., *Commentary: The Materials Project: A materials genome approach to accelerating materials innovation.* APL Materials, 2013. **1**(1): p. 011002.

92. Yoshimura, H.N., et al., *Mechanical Properties and Microstructure of Zinc Oxide Varistor Ceramics.* Materials Science Forum, 2006. **530-531**: p. 408-413.
93. O'Connor, B., et al., *Correlations between Mechanical and Electrical Properties of Polythiophenes.* ACS Nano, 2010. **4**(12): p. 7538-7544.
94. SEMICORE. *Sputtering Yield Rates*. 2020 [cited 2020 9th June]; Available from: http://www.semicore.com/reference/sputtering-yields-reference.
95. Munshi, J., et al., *Elasto-morphology of P3HT:PCBM bulk heterojunction organic solar cells.* Soft Matter, 2020. **16**(29): p. 6743-6751.
96. Müller, C., et al., *Tough, Semiconducting Polyethylene ‐ poly(3 ‐ hexylthiophene) Diblock Copolymers.* Advanced Functional Materials, 2007. **17**: p. 2674-2679.
97. Stafford, C.M., et al., *Elastic Moduli of Ultrathin Amorphous Polymer Films.* Macromolecules, 2006. **39**(15): p. 5095-5099.
98. Koltzenburg, S., Maskos, Michael, Nuyken, Oskar, *Polymer Chemistry*. 1 ed. 2017: Springer-Verlag Berlin Heidelberg. 584.
99. Wang, X., et al., *The Lennard-Jones potential: when (not) to use it*. 2019.
100. O'Connor, T.F., et al., *Wearable organic solar cells with high cyclic bending stability: Materials selection criteria.* Solar Energy Materials and Solar Cells, 2016. **144**: p. 438-444.
101. Awartani, O., M.W. Kudenov, and B.T. O'Connor, *Organic photovoltaic cells with controlled polarization sensitivity.* Applied Physics Letters, 2014. **104**(9): p. 093306.
102. Yu, Z., et al., *Highly Flexible Silver Nanowire Electrodes for Shape-Memory Polymer Light-Emitting Diodes.* Advanced Materials, 2011. **23**(5): p. 664-668.
103. O'Connor, T.F., et al., *Stretching and conformal bonding of organic solar cells to hemispherical surfaces.* Energy & Environmental Science, 2014. **7**(1): p. 370-378.
104. Rodriquez, D., et al., *Mechanical Properties of Solution-Processed Small-Molecule Semiconductor Films.* ACS Applied Materials & Interfaces, 2016. **8**(18): p. 11649-11657.
105. Yasuda, T., L. Han, and T. Tsutsui, *Fabrication of Stretch-Oriented Regioregular Poly(3-Hexylthiophene) film and Its Application to Organic Field-Effect Transistors.* Journal of Photopolymer Science and Technology, 2009. **22**(6): p. 713-717.
106. Lipomi, D.J., et al., *Toward mechanically robust and intrinsically stretchable organic solar cells: Evolution of photovoltaic properties with tensile strain.* Solar Energy Materials and Solar Cells, 2012. **107**: p. 355-365.
107. Lipomi, D.J., et al., *Stretchable Organic Solar Cells.* Advanced Materials, 2011. **23**(15): p. 1771-1775.
108. Abdelhadi, O., L. Ladani, and J. Razmi, *Fracture toughness of bonds using interfacial stresses in four-point bending test.* Mechanics of Materials - MECH MATER, 2011. **43**: p. 885-900.
109. Brand, V., C. Bruner, and R. Dauskardt, *Cohesion and device reliability in organic bulk heterojunction photovoltaic cells.* Solar Energy Materials and Solar Cells, 2012. **99**: p. 182–189.
110. Dupont, S.R., et al., *Interlayer adhesion in roll-to-roll processed flexible inverted polymer solar cells.* Solar Energy Materials and Solar Cells, 2012. **97**: p. 171-175.
111. Savagatrup, S., et al., *Mechanical degradation and stability of organic solar cells: molecular and microstructural determinants.* Energy & Environmental Science, 2015. **8**(1): p. 55-80.
112. Wagner, S. and S. Bauer, *Materials for stretchable electronics.* MRS Bulletin, 2012. **37**(3): p. 207-213.
113. Sekitani, T. and T. Someya, *Stretchable, large-area organic electronics.* Adv Mater, 2010. **22**(20): p. 2228-46.
114. Padhye, N., et al., *Enhancing the performance of the T-peel test for thin and flexible adhered laminates.* Rev Sci Instrum, 2016. **87**(8): p. 085111.
115. Juillard, S., *Optimization of the interfaces of encapsulated OPV*

devices, in *Chemical engineering.* 2018, Université Grenoble Alpes. p. 226.
116. Heinzmann, C., C. Weder, and L.M. de Espinosa, *Supramolecular polymer adhesives: advanced materials inspired by nature.* Chemical Society Reviews, 2016. **45**(2): p. 342-358.

117. Gupta, S.K., et al., *Degradation of organic photovoltaic devices: a review.* Nanomaterials and Energy, 2013. **2**(1): p. 42-58.
118. Sawyer, E.J., et al., *Large increase in stretchability of organic electronic materials by encapsulation.* Extreme Mechanics Letters, 2016. **8**: p. 78-87.
119. Lare, Y., et al., *Influence of the exciton blocking layer on the stability of layered organic solar cells.* Journal of Physics and Chemistry of Solids, 2011. **72**(2): p. 97-103.
120. Harris, K., A. Elias, and H.-j. Chung, *Flexible electronics under strain: a review of mechanical characterization and durability enhancement strategies.* Journal of Materials Science, 2015. **51**.
121. Ren, -.H., et al., - *Three-point and four-point mechanical bending test modeling and application in solar cells.* - Acta Physica Sinica, 2019. **- 68**(- 20): p. - 208801-1.
122. Gherardi Hein, P.R. and L. Brancheriau, *Comparison between three-point and four-point flexural tests to determine wood strength of Eucalyptus specimens.* Maderas: Ciencia y Tecnología, 2018. **20**.
123. Raheem, Z., *Standard Test Methods for Flexural Properties of Unreinforced and Reinforced Plastics and Electrical Insulating Materials 1*. 2019.
124. Chen, H., et al., *Interfacial Failure in Flexible Electronic Devices.* IEEE Electron Device Letters, 2014. **35**(1): p. 132-134.
125. Leterrier, Y., et al., *Biaxial fragmentation of thin silicon oxide coatings on poly(ethylene terephthalate).* Journal of Materials Science, 2001. **36**(9): p. 2213-2225.
126. Tait, J.G., et al., *Spray coated high-conductivity PEDOT:PSS transparent electrodes for stretchable and mechanically-robust organic solar cells.* Solar Energy Materials and Solar Cells, 2013. **110**: p. 98-106.
127. Gomez, L., et al., *Continuous, Highly Flexible, and Transparent Graphene Films by Chemical Vapor Deposition for Organic Photovoltaics.* ACS nano, 2010. **4**: p. 2865-73.
128. Yoon, J., et al., *Ultrathin silicon solar microcells for semitransparent, mechanically flexible and microconcentrator module designs.* Nature materials, 2008. **7**: p. 907-15.
129. Khanna, V.K., *Flexible Electronics*. 2019, UK: IOP Publishing.
130. Logothetidis, S., *Handbook of Flexible Organic Electronics: Materials, Manufacturing and Applications*. 2014: Woodhead Publishing.
131. Lewis, J., *Material challenge for flexible organic devices.* Materials Today, 2006. **9**(4): p. 38-45.
132. Suo, Z., *Mechanics of stretchable electronics and soft machines.* MRS Bulletin, 2012. **37**.
133. Johlin, E., et al., *Structural origins of intrinsic stress in amorphous silicon thin films.* Physical Review B, 2012. **85**(7): p. 075202.
134. Dias, T., *Electronic textiles : smart fabrics and wearable technology.* 2015.
135. Miccoli, I., et al., *The 100th anniversary of the four-point probe technique: The role of probe geometries in isotropic and anisotropic systems.* Journal of Physics Condensed Matter, 2015. **27**.
136. Eaton, P. and P. West, *Atomic Force Microscopy*. 2010.
137. Albrecht, T.R., et al., *Microfabrication of cantilever styli for the atomic force microscope.* journal of vacuum science and technology, 1990. **8**(4): p. 3386-3396.
138. Han, Y., et al., *Efficiency above 12% for 1 cm(2) Flexible Organic Solar Cells with Ag/Cu Grid Transparent Conducting Electrode.* Advanced science (Weinheim, Baden-Wurttemberg, Germany), 2019. **6**(22): p. 1901490-1901490.
139. Zhang, Y., et al., *Thermally Stable All-Polymer Solar Cells with High Tolerance on Blend Ratios.* Advanced Energy Materials, 2018. **8**(18): p. 1800029.
140. Lilliedal, M.R., et al., *The effect of post-processing treatments on inflection points in current–voltage curves of roll-to-roll processed polymer photovoltaics.* Solar Energy Materials and Solar Cells, 2010. **94**(12): p. 2018-2031.

141. Cheun, H., et al., *Electrical and Optical Properties of ZnO Processed by Atomic Layer Deposition in Inverted Polymer Solar Cells.* The Journal of Physical Chemistry C, 2010. **114**(48): p. 20713-20718.
142. Wang, Y., et al., *Stability of Nonfullerene Organic Solar Cells: from Built-in Potential and Interfacial Passivation Perspectives.* Advanced Energy Materials, 2019. **9**(19): p. 1900157.
143. Hu, L., et al., *Chemical reaction between an ITIC electron acceptor and an amine-containing interfacial layer in non-fullerene solar cells.* Journal of Materials Chemistry A, 2018. **6**(5): p. 2273-2278.
144. Wang, Y., et al., *Origin of Efficient Inverted Nonfullerene Organic Solar Cells: Enhancement of Charge Extraction and Suppression of Bimolecular Recombination Enabled by Augmented Internal Electric Field.* The Journal of Physical Chemistry Letters, 2017. **8**(21): p. 5264-5271.
145. Park, G.-S. and J.-K. Kwon, *Degradation of ITO/PET films in humid and contaminative environments studied by TEM.* Journal of Materials Science: Materials in Electronics, 2001. **12**(9): p. 497-503.
146. Liu, C., et al., *Flexible organic solar cells: Materials, large-area fabrication techniques and potential applications.* Nano Energy, 2021. **89**: p. 106399.
147. Lim, C.-Y., et al., *Mechanical and Electrical Stability Indium-Tin-Oxide Coated Polymer Substrates under Continuous Bending Stress Condition.* Journal of International Council on Electrical Engineering, 2012. **2**(3): p. 237-241.
148. Kirubanandham, A. and S. Basu, *On Characterization of Mechanical Deformation in Flexible Electronic Structures*. 2012.
149. Mao, L., et al., *Mechanical Analyses and Structural Design Requirements for Flexible Energy Storage Devices.* Advanced Energy Materials, 2017. **7**(23): p. 1700535.
150. Lim, K., et al., *Flexible PEDOT: PSS/ITO hybrid transparent conducting electrode for organic photovoltaics.* Solar Energy Materials and Solar Cells, 2013. **115**: p. 71-78.
151. Sekitani, T., et al., *Stretchable active-matrix organic light-emitting diode display using printable elastic conductors.* Nature Materials, 2009. **8**(6): p. 494-499.
152. Kim, E.-H., et al., *Nucleation and growth of crystalline Indium Tin Oxide (ITO) coatings on polyethylene terephthalate (PET).* Surface and Coatings Technology, 2010. **205**(1): p. 1-8.
153. Kim, Y.S., et al., *Mechanical reliability of transparent conducting IZTO film electrodes for flexible panel displays.* Applied Surface Science, 2011. **257**(18): p. 8134-8138.
154. Abdallah, A.A., et al., *Buckle initiation and delamination of patterned ITO layers on a polymer substrate.* Surface and Coatings Technology, 2011. **205**(8): p. 3103-3111.
155. Boehme, M. and C. Charton, *Properties of ITO on PET film in dependence on the coating conditions and thermal processing.* Surface and Coatings Technology, 2005. **200**(1): p. 932-935.
156. Can, M., et al., *Electrical properties of SAM-modified ITO surface using aromatic small molecules with double bond carboxylic acid groups for OLED applications.* Applied Surface Science, 2014. **314**: p. 1082-1086.
157. Han, D., et al., *Cathodic multilayer transparent electrodes for ITO-free inverted organic solar cells.* Organic Electronics, 2013. **14**(6): p. 1477-1482.
158. Kim, D.-H., et al., *Thickness dependence of electrical properties of ITO film deposited on a plastic substrate by RF magnetron sputtering.* Applied Surface Science, 2006. **253**(2): p. 409-411.
159. Dauskardt, R.H., et al., *Adhesion and debonding of multi-layer thin film structures.* Engineering Fracture Mechanics, 1998. **61**(1): p. 141-162.
160. Bruner, C., et al., *Molecular Intercalation and Cohesion of Organic Bulk Heterojunction Photovoltaic Devices.* Advanced Functional Materials, 2013. **23**(22): p. 2863-2871.
161. Kim, J.-H., et al., *Understanding mechanical behavior and reliability of organic electronic materials.* Mrs Bulletin, 2017. **42**: p. 115-123.

162. Juillard, S., et al., *Mechanical Reliability of Flexible Encapsulated Organic Solar Cells: Characterization and Improvement.* ACS Applied Materials & Interfaces, 2018. **10**(35): p. 29805-29813.
163. Vilkman, M., et al., *Gravur… Printed ZnO in Fully RolŒ t• Roll Printed Inverted Organic Solar Cells: Optimization of Adhesion and Performance.* Energy technology, 2015. **3**: p. 407-413.
164. Kim, J.-H., et al., *Effect of Ultraviolet-Ozone Treatment on the Properties and Antibacterial Activity of Zinc Oxide Sol-Gel Film.* Materials (Basel, Switzerland), 2019. **12**(15): p. 2422.
165. Hook, D.A., et al., *Evaluation of Oxygen Plasma and UV Ozone Methods for Cleaning of Occluded Areas in MEMS Devices.* Journal of Microelectromechanical Systems, 2010. **19**: p. 1292-1298.
166. Kang, D.J., et al., *Enhancing Mechanical Properties of Highly Efficient Polymer Solar Cells Using Size-Tuned Polymer Nanoparticles.* ACS Applied Materials & Interfaces, 2015. **7**(4): p. 2668-2676.
167. Sierros, K.A., et al., *Mechanical properties of ZnO thin films deposited on polyester substrates used in flexible device applications.* Thin Solid Films, 2010. **519**(1): p. 325-330.
168. Stalder, A.F., et al., *A snake-based approach to accurate determination of both contact points and contact angles.* Colloids and Surfaces A: Physicochemical and Engineering Aspects, 2006. **286**(1): p. 92-103.
169. Chen, J. and S.J. Bull, *Approaches to investigate delamination and interfacial toughness in coated systems: an overview.* Journal of Physics D: Applied Physics, 2010. **44**(3): p. 034001.
170. Chen, L., et al., *A new approach to determine wedge-indented interfacial toughness in soft-film hard-substrate systems with application to low-k films on Si substrate.* Journal of Materials Research, 2012. **27**(22): p. 2872-2883.
171. Yeap, K.B., et al., *Determining interfacial properties of submicron low-k films on Si substrate by using wedge indentation technique.* Journal of Applied Physics, 2007. **101**(12): p. 123531.
172. Yu, S., et al., *All-Solution-Processed Molybdenum Oxide-Encapsulated Silver Nanowire Flexible Transparent Conductors with Improved Conductivity and Adhesion.* ACS Applied Materials & Interfaces, 2021. **13**(12): p. 14470-14478.
173. Dupont, S.R., et al., *Adhesion properties of inverted polymer solarcells: Processing and film structure parameters.* Organic Electronics, 2013. **14**(5): p. 1262-1270.
174. Wang, C.-T., et al., *Improvement of optical and electric characteristics of MoO3/Ag film/MoO3 flexible transparent electrode with metallic grid.* Journal of Applied Physics, 2016. **120**(19): p. 195305.
175. Greenbank, W., et al., *Improved mechanical adhesion and electronic stability of organic solar cells with thermal ageing: the role of diffusion at the hole extraction interface.* Journal of Materials Chemistry A, 2017. **5**(6): p. 2911-2919.
176. Greenbank, W.A., et al., *Interfacial thermal degradation in inverted organic solar cells.* Applied Physics Letters, 2015. **107**: p. 263301.
177. Han, G.S., et al., *Multi-functional transparent electrode for reliable flexible perovskite solar cells.* Journal of Power Sources, 2019. **435**: p. 226768.
178. Wang, Y., et al., *Solution-Processed MoO3:PEDOT:PSS Hybrid Hole Transporting Layer for Inverted Polymer Solar Cells.* ACS Applied Materials & Interfaces, 2015. **7**(13): p. 7170-7179.
179. Balar, N., et al., *Role of Polymer Segregation on the Mechanical Behavior of All-Polymer Solar Cell Active Layers.* ACS Applied Materials & Interfaces, 2017. **9**(50): p. 43886-43892.
180. Onorato, J., V. Pakhnyuk, and C.K. Luscombe, *Structure and design of polymers for durable, stretchable organic electronics.* Polymer Journal, 2017. **49**(1): p. 41-60.
181. Roth, B., et al., *Mechanical Properties of a Library of Low-Band-Gap Polymers.* Chemistry of Materials, 2016. **28**(7): p. 2363-2373.
182. Hajduk, B., et al., *P3HT:PCBM blend films phase diagram on the base of variable-temperature spectroscopic ellipsometry.* Beilstein journal of nanotechnology, 2018. **9**: p. 1108-1115.

183. Choi, J., et al., *Influence of Acceptor Type and Polymer Molecular Weight on the Mechanical Properties of Polymer Solar Cells.* Chemistry of Materials, 2019. **31**(21): p. 9057-9069.
184. Choi, J., et al., *Importance of Critical Molecular Weight of Semicrystalline n-Type Polymers for Mechanically Robust, Efficient Electroactive Thin Films.* Chemistry of Materials, 2019. **31**(9): p. 3163-3173.
185. Koch, F.P.V., et al., *The impact of molecular weight on microstructure and charge transport in semicrystalline polymer semiconductors–poly(3-hexylthiophene), a model study.* Progress in Polymer Science, 2013. **38**(12): p. 1978-1989.
186. Swathi, S.K., P.C. Ramamurthy, and S.M. Garner. *In-situ flexural OPV measurements on flexible glass substrate*. in *2015 IEEE 42nd Photovoltaic Specialist Conference (PVSC)*. 2015.
187. Suo, Z., et al., *Mechanics of rollable and foldable film-on-foil electronics.* Applied Physics Letters, 1999. **74**(8): p. 1177-1179.

Appendix A

PhD Achievements

- Publications:

Du, T., Ratnasingham, S. R., Kosasih, F. U., Macdonald, T. J., Mohan, L., Augurio, A., **Ahli, H.**, Lin, C.-T., Xu, S., Xu, W., Binions, R., Ducati, C., Durrant, J. R., Briscoe, J., McLachlan, M. A., Aerosol Assisted Solvent Treatment: A Universal Method for Performance and Stability Enhancements in Perovskite Solar Cells. Adv. Energy Mater. 2021, 11, 2101420. https://doi.org/10.1002/aenm.202101420

- Poster and oral presentations:

2020: Innovations in Large-Area Electronics Conferences, UK.

2019: Imperial College Materials Symposium, UK.

2018: Imperial College Plastic Electronics Centre of Doctoral Training (PE-CDT) symposium

Appendix B

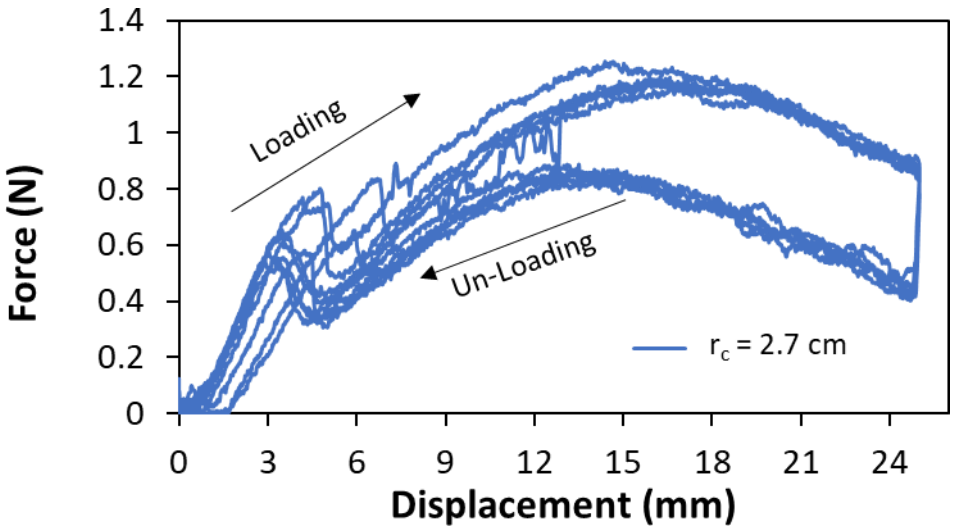

Figure B 1 shows the Force/displacement curve extracted from after 3 point bending test to an encapsulated OPV at bending radius of 2.7 cm. Clearly indicating an elastic strain behaviour and thus explaining why the OPV did not experience any permanent deformation on it's shape. Although the signals are less noisy compared to a un-encapsulated devices, a lot of fluctuations are noticed thus FEA was used to confirm the forces required for the bending and also stress distribution values.

Appendix C

Section 5.3 Chapter 5

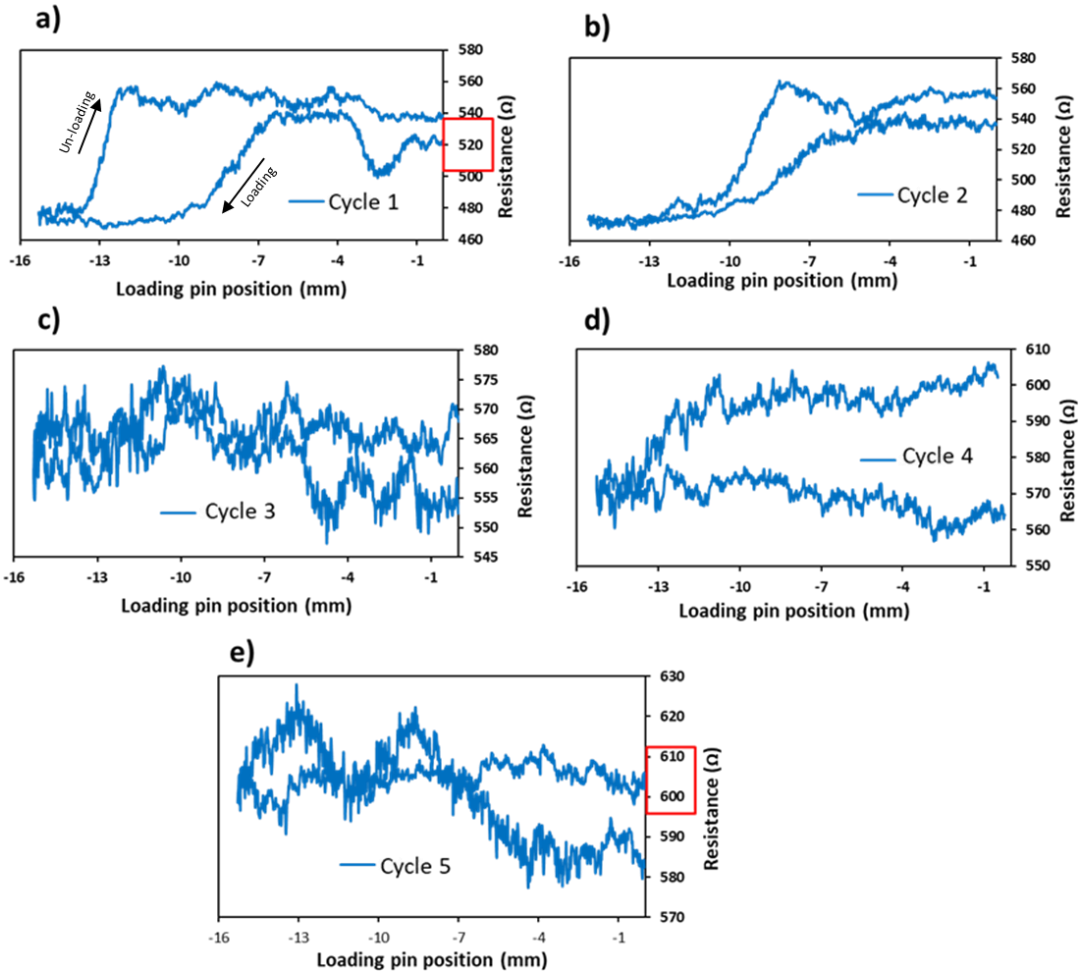

Figure C- 1 shows the in the resistance of the sandwich device (ITO/ZnO/Ag) during bending with bending radius 5 cm. The negative signs in the loading pin position indicated the downward movement. When the loading pin is at 0 mm, the sample is flat. In here, the 5 cycles have individually plotted, to show the reversibility of the changes in ZnO sandwich device. a) first cycle b)second cycle c)third cycle d) forth cycle e)fifth cycle.

As indicated in Figure B-1, the reversibility becomes clearer once each cycle is plotted individually. Thus, the overall change in resistance at 5 cm bending raidus for the sandwich device with ZnO layer is around 85 Ω.

Appendix D

Hydraulic robotic arm – for in-situ bending under illumination

Brand	CONSTRUCT & CREATE
Item weight	500 g
Item model number	52186
Range of motion	6 axis of movement Made from 229 plastic pieces Lifting capacity – 50 g Vertical reach – 42 cm Horizontal reach – 32 cm Elbow range – 44° Base rotation – 270° Shoulder motion – 45° Wrist rotation – 180° Wrist mobility – 98°

Appendix E

Section 5.4 chapter 5

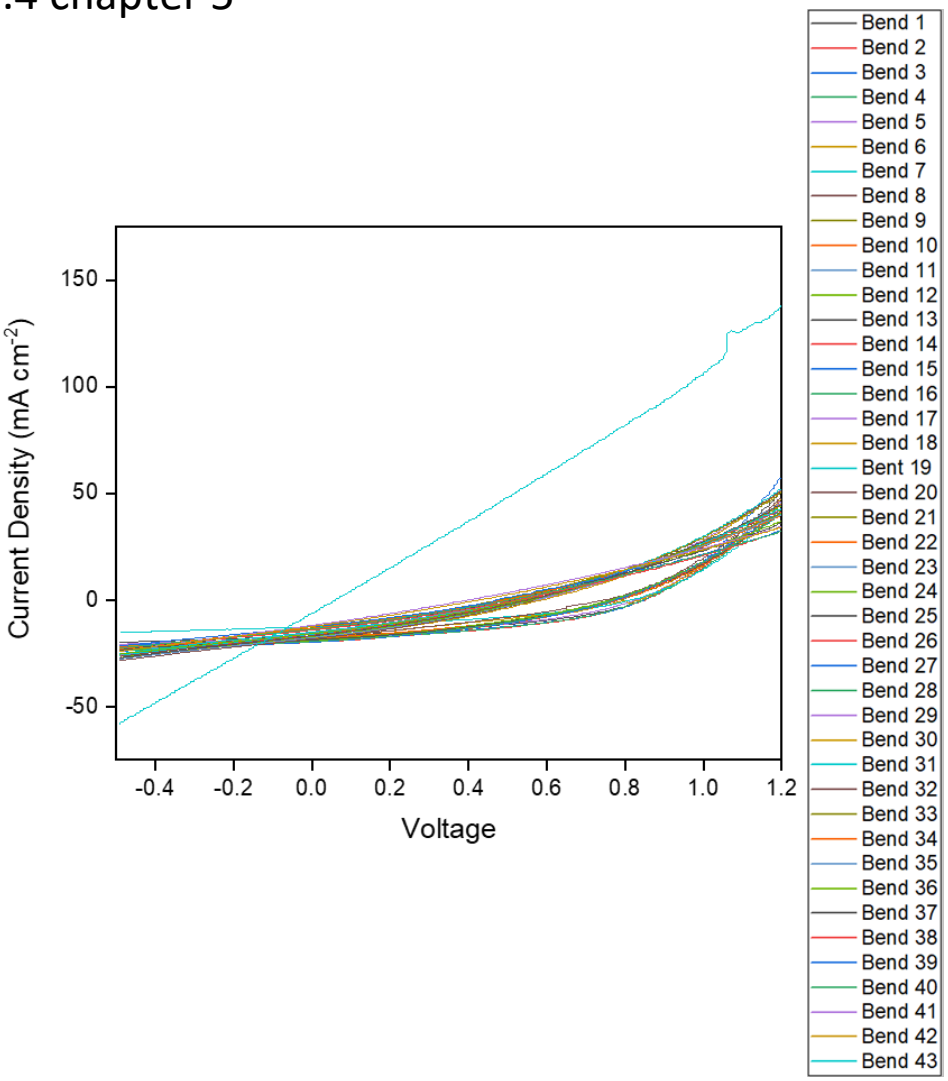

Figure E-1 J-V curves of flexible OPV under bending with bending radius of 5 cm.

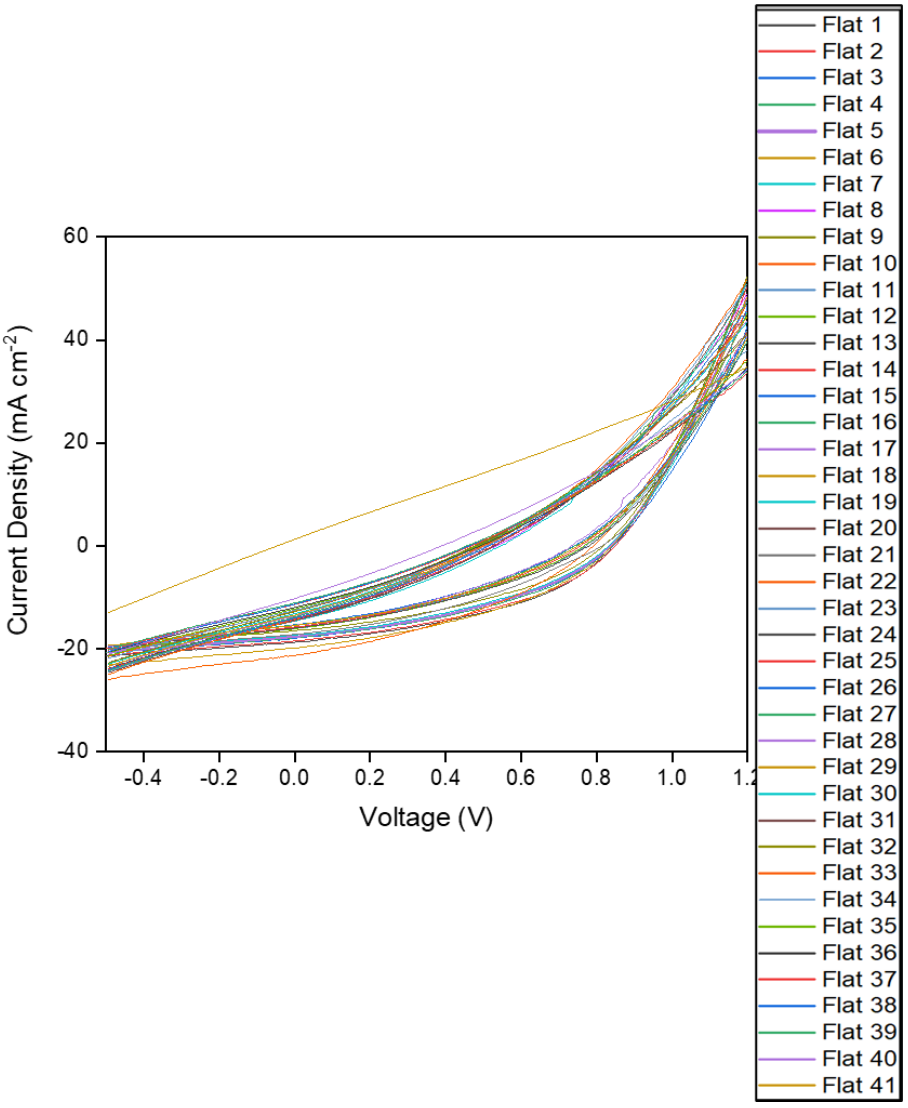

Figure E-2 J-V curves of flexible OPV under flat conditions.

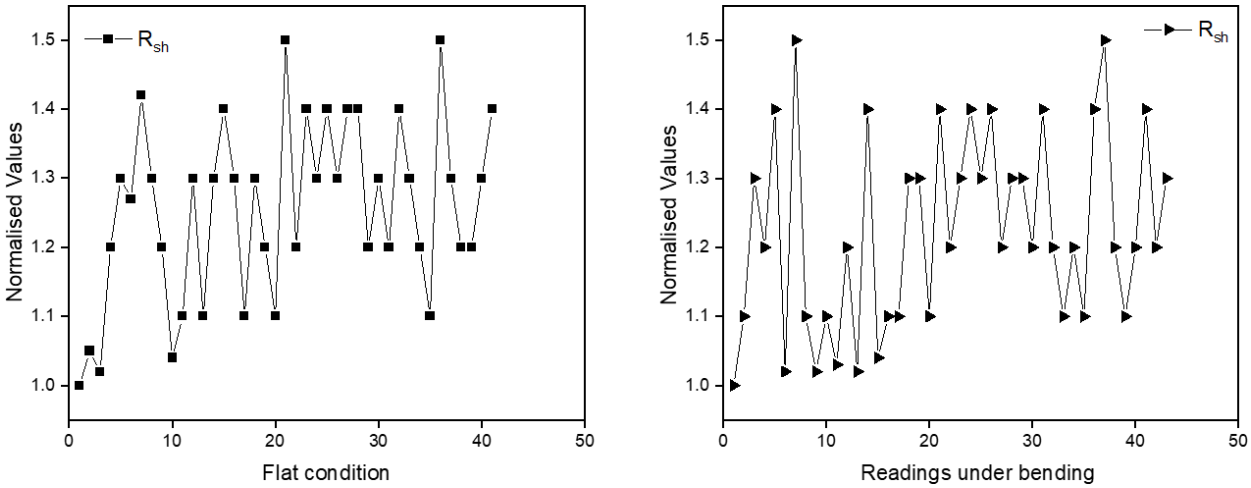

Figure E- 3 R_{sh} normalised values of OPV a flat condition (on the left side), and under bending conditions with bending radius of 5 cm under illumination (on right side)

Appendix F

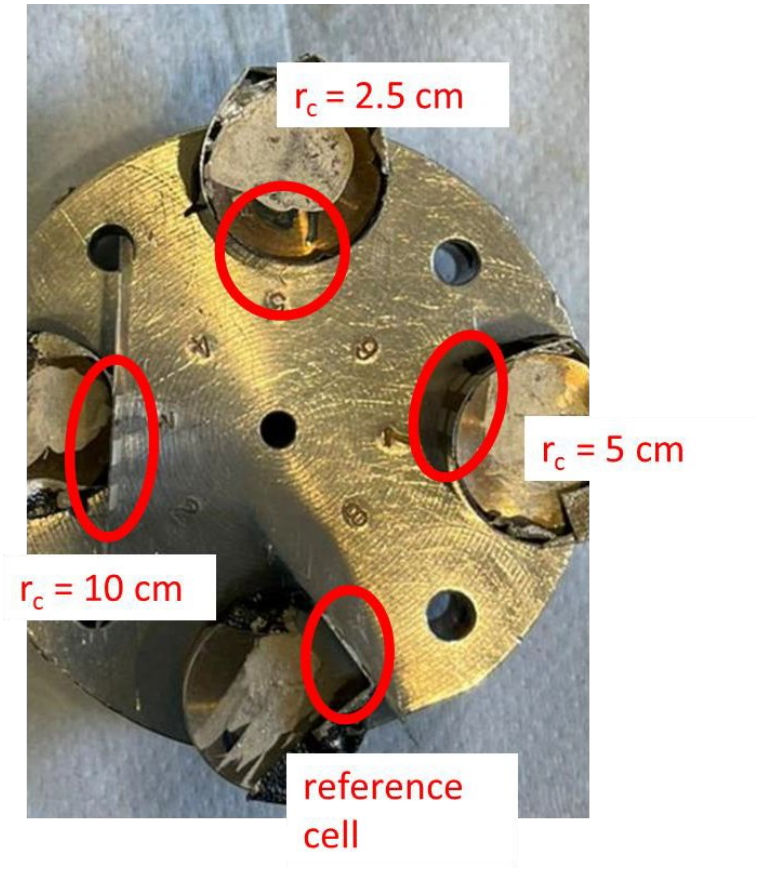

Figure E- 1 Illustrates an in-situ SEM method of visualizing the effect of bending radius and bending cycles through the cross section without used FIB. Edge of PET was removed before fabricating the device, then underwent 100 bending cycles for their respective being radiuses. The samples were then wrapped around an SEM holder vertically to look at an exposed cross sec

Appendix G
Permissions to republish third party copyrighted works

Figure Number	Permission details
Figure 2-1	*Attribution-NonCommercial-ShareAlike 2.0 UK: England & Wales (CC BY-NC-SA 2.0 UK)* © 2008-2022 The University of Liverpool
Figure 2-2	*Attribution-NonCommercial-ShareAlike 4.0 International (CC BY-NC-SA 4.0)* *"Molecular Orbitals" by Kathryn Haas, LibreTexts is licensed under CC BY-NC-SA .*
Figure 2-7	*License no. 4997701084313* *Noriega, R., Efficient Charge Transport in Disordered Conjugated Polymer Microstructures. Macromolecular Rapid Communications, 2018.* ***39****(14): p. 1800096.* © 2018 WILEY-VCH Verlag GmbH & Co. KGaA, Weinheim
Figure 2-9	*License no. 1191008* Servaites, J.D., M.A. Ratner, and T.J. Marks, *Organic solar cells: A new look at traditional models.* Energy & Environmental Science, 2011. 4(11): p. 4410-4422. © The Royal Society of Chemistry 2011
Figure 2-10	Printz, A.D., et al., *Yield Point of Semiconducting Polymer Films on Stretchable Substrates Determined by Onset of Buckling.* ACS Applied Materials & Interfaces, 2015. **7**(41): p. 23257-23264. Copyright © 2015, American Chemical Society

Figure 2-11	*License no. 1191009* Savagatrup, S., et al., *Mechanical degradation and stability of organic solar cells: molecular and microstructural determinants.* Energy & Environmental Science, 2015. 8(1): p. 55-80. © The Royal Society of Chemistry 2015